

MICROWAVE REMOTE SENSING OF SAHARAN ERGS AND
AMAZON VEGETATION

by

Haroon Stephen

A dissertation submitted to the faculty of

Brigham Young University

in partial fulfillment of the requirements for the degree of

Doctor of Philosophy

Department of Electrical and Computer Engineering

Brigham Young University

August 2006

Copyright © 2006 Haroon Stephen

All Rights Reserved

BRIGHAM YOUNG UNIVERSITY

GRADUATE COMMITTEE APPROVAL

of a dissertation submitted by

Haroon Stephen

This dissertation has been read by each member of the following graduate committee and by majority vote has been found to be satisfactory.

Date

David G. Long, Chair

Date

Michael A. Jensen

Date

Karl F. Warnick

Date

Richard H. Selfridge

Date

A. Lee Swindlehurst

BRIGHAM YOUNG UNIVERSITY

As chair of the candidate's graduate committee, I have read the dissertation of Haroon Stephen in its final form and have found that (1) its format, citations, and bibliographical style are consistent and acceptable and fulfill university and department style requirements; (2) its illustrative materials including figures, tables, and charts are in place; and (3) the final manuscript is satisfactory to the graduate committee and is ready for submission to the university library.

Date

David G. Long
Chair, Graduate Committee

Accepted for the Department

Michael A. Jensen
Graduate Coordinator

Accepted for the College

Alan R. Parkinson
Dean, Ira A. Fulton College of
Engineering and Technology

ABSTRACT

MICROWAVE REMOTE SENSING OF SAHARAN ERGS AND AMAZON VEGETATION

Haroon Stephen

Electrical and Computer Engineering

Doctor of Philosophy

This dissertation focuses on relating spaceborne microwave data to the geophysical characteristics of the Sahara desert and the Amazon vegetation. Radar and radiometric responses of the Saharan ergs are related to geophysical properties of sand formations and near surface winds. The spatial and temporal variability of the Amazon vegetation is studied using multi-frequency and multi-polarization data.

The Sahara desert includes large expanses of sand dunes called ergs that are constantly reshaped by prevailing winds. Radar backscatter (σ°) measurements observed at various incidence (θ) and azimuth (ϕ) angles from the NASA Scatterometer (NSCAT), the ERS scatterometer (ESCAT), the SeaWinds scatterometer aboard QuikScat (QSCAT), and the Precipitation Radar (TRMM-PR) aboard the Tropical Rain Monitoring Mission (TRMM) are used to model the σ° response from sand dunes. Backscatter θ and ϕ variation depends upon the slopes and orientations of the dune slopes. Sand dunes are modeled as a composite of tilted rough facets, which are characterized by a probability distribution of tilt. The small ripples are modeled as cosinusoidal surface waves that contribute to the return signal at Bragg angles.

The σ° response is high at look angles equal to the mean tilts of the rough facets and is lower elsewhere. The modeled σ° response is similar to NSCAT and ESCAT observations. σ° also varies spatially and reflects the spatial inhomogeneity of the sand surface. A model incorporating the σ° ϕ -modulation and spatial inhomogeneity is proposed. The maxima of the ϕ -modulation at $\theta = 33^\circ$ reflect the orientation of the slip-sides on the sand surface. These slip-side orientations are consistent with the European Centre for Medium-Range Weather Forecasts wind directions spatially and temporally.

Radiometric emissions from the ergs have strong dependence on the surface geometry. The radiometric temperature (T_b) of ergs is modeled as the weighted sum of the T_b from all the composite tilted rough facets. The dual polarization T_b measurements at 19 GHz and 37 GHz from the Special Sensor Microwave Imager (SSM/I) aboard the Defense Meteorological Satellite Program and the Tropical Rainfall Measuring Mission Microwave Imager are used to analyze the radiometric response of erg surfaces and compared to the model results. It is found that longitudinal and transverse dune fields are differentiable based on their polarization difference (ΔT_b) ϕ -modulation, which reflects type and orientation of dune facets. ΔT_b measurements at 19 GHz and 37 GHz provide consistent results.

In the Amazon, σ° measurements from Seasat A scatterometer (SASS), ESCAT, NSCAT, QSCAT and TRMM-PR; and T_b measurements from SSM/I are used to study the multi-spectral microwave response of vegetation. σ° versus θ signatures of data combined from scatterometers and the precipitation radar depend upon vegetation density. The multi-frequency signatures of σ° and T_b provide unique responses for different vegetation densities. σ° and T_b spatial inhomogeneity is related to spatial geophysical characteristics. Temporal variability of the Amazon basin is studied using C-band ERS data and a Ku-band time series formed by SASS, NSCAT and QSCAT data. Although the central Amazon forest represents an area of very stable radar backscatter measurements, portions of the southern region exhibit backscatter changes over the past two decades.

ACKNOWLEDGMENTS

I express my profound gratitude to Dr. David Long for giving me opportunity to conduct this research. His continuous guidance and encouragement have been an ever increasing inspiration for me and have motivated me to progress and advance.

I am thankful to Microwave Earth Remote Sensing Lab., for the financial support it granted me to complete my higher studies. I extend my warmest appreciations to my department and university for providing a morally clean and friendly educational environment.

I am deeply grateful for the love of my parents that continuously strengthens me to face challenges with dignity.

Contents

Abstract	v
List of Tables	xiii
List of Figures	xv
1 Introduction	1
1.1 Description of the Problem	2
1.2 Research Contributions	5
1.3 Dissertation Outline	7
2 Background	9
2.1 Sand and Wind	9
2.2 Rain Forest	11
2.3 Active Microwave Remote Sensing	12
2.3.1 Spaceborne Active Microwave Sensors	12
2.3.2 Active Microwave Remote Sensing of Sand	15
2.3.3 Active Microwave Remote Sensing of Forest	17
2.4 Passive Microwave Remote Sensing	18
2.4.1 Spaceborne Passive Microwave Sensors	19
2.4.2 Passive Microwave Remote Sensing of Sand	19
2.4.3 Passive Microwave Remote Sensing of Forest	22
2.5 ECMWF Winds	23
3 Microwave Backscatter Modeling of Erg Surfaces – Static	25
3.1 Surface Backscatter Model	25

3.1.1	Rough Facet Model	27
3.1.2	Cosinusoidal Ripple Model	30
3.2	Rough Facet Model Simulation	32
3.2.1	Longitudinal Dune	33
3.2.2	Transverse Dune	36
3.3	Summary	40
4	Microwave Backscatter Modeling of Erg Surfaces – Dynamic	43
4.1	Observation geometry induced σ° modulation	43
4.1.1	σ° Azimuth Angle Modulation	46
4.1.2	σ° Centroid Displacement Variability	49
4.2	σ° Full Observation Model Results	51
4.2.1	Incidence Angle Dependence of Model Parameters	54
4.2.2	Spatial Behavior of Model Parameters	60
4.2.3	Temporal Behavior of Model Parameters	65
4.3	Summary	65
5	Modeling Microwave Emissions of Erg Surfaces	67
5.1	Radiometric Emission from Sand	68
5.1.1	Radiometric Emission Model	68
5.1.2	Facet Model	72
5.1.3	ΔT_b Response over Model Dunes	73
5.2	Spaceborne T_b Observations	78
5.3	Summary	86
6	Microwave Study of Amazon Vegetation	89
6.1	σ° Incidence Angle Dependence of Vegetation	89
6.2	Multi-Spectral σ° and T_b Signatures	94
6.3	Spatial Inhomogeneity Model	96
6.4	Time Series Analysis	102
6.5	Summary	106

7	Conclusions and Recommendations	109
7.1	Results	109
7.1.1	Radar Backscatter Directional Modulation from Erg Surfaces .	109
7.1.2	Radar Backscatter Spatial Inhomogeneity of Erg Surfaces . . .	110
7.1.3	Average Wind Behavior over Ergs from $\sigma^\circ(\theta, \phi)$ Response . . .	111
7.1.4	Microwave Emission Azimuth Modulation from Erg Surfaces .	111
7.1.5	Signatures of Amazon Vegetation	112
7.1.6	Consistency of Different Spaceborne Microwave Instruments .	112
7.2	Recommendations for Future Research	113
	Bibliography	115
A	Derivation of View Geometry Relationships	123
A.1	Local Incidence and Azimuth Angles	123
A.2	Grazing Angle	124
A.3	Bragg Look Directions	125
A.4	Maxima of Second Order Harmonic	126

List of Tables

2.1	Table listing selected study sites in the Sahara-Arabian desert	13
4.1	RMS errors for different σ° model versions applied to NSCAT data .	49
4.2	RMS errors for different σ° model versions applied to ESCAT data . .	50
4.3	Table listing ECMWF wind modes and slip-side orientations inferred from NSCAT and ESCAT data over different surface types	59
5.1	Table listing the parameters of T_b and ΔT_b model fits to observed data over longitudinal dunes at 19 and 37 GHz	82
5.2	Table listing RMS errors for T_b and ΔT_b models at 19 and 37 GHz . .	84

List of Figures

2.1	Diagram illustrating different dune shapes	11
2.2	Map of the Saharao-Arabian desert showing selected sites	13
2.3	Diagram showing the stratified sand subsurface used for radiometric emission model	21
3.1	Diagram showing a simple sand surface with surface and volume scattering components.	26
3.2	Plot showing volume scattering from sand as a function of θ	27
3.3	σ° θ -response and ϕ -modulation of Sand Sheets	29
3.4	Model of tilted rough facet with cosinusoidal surface ripples and Bragg backscattering response	31
3.5	Tilted rough surface model σ° response of single facet	33
3.6	Longitudinal dune σ° azimuth angle response	34
3.7	Longitudinal dune σ° incidence angle response	35
3.8	Longitudinal dune facet model	36
3.9	Longitudinal dune facet model response and scatterometer response	37
3.10	Transverse dune σ° azimuth angle response	38
3.11	Transverse dune σ° incidence angle response	39
3.12	Transverse dune facet model	40
3.13	Transverse dune facet model response and scatterometer response	41
4.1	Spaceborne scatterometer σ° observation geometry parameters	44
4.2	NSCAT and ESCAT $\sigma^\circ(\theta)$ for different sand surfaces	46
4.3	NSCAT and ESCAT measurement θ - ϕ sampling and σ° model surface fit over complex dunes	47
4.4	NSCAT $\sigma^\circ(r, \beta)$ model fit over complex dunes	52
4.5	σ° model fits with and without considering σ° spatial inhomogeneity over a complex dune field	53

4.6	Plots illustrating θ dependence of the σ° model parameters	56
4.7	Plots of $q_\theta(\phi)$ and $h_\theta(r, \beta)$ computed using the full model	57
4.8	A slice through $q_\theta(\phi)$ surface fit defining azimuth angle of a peak . . .	58
4.9	NSCAT ψ and m as a function of θ over different sand surfaces	58
4.10	Spatial maps of the σ° model parameters from NSCAT and ECMWF wind map of Saharan Ergs during January	61
4.11	Spatial maps of ψ_1 from ESCAT and QSCAT, and ECMWF wind map of Saharan Ergs during June	63
4.12	Spatial maps of ψ_1 from NSCAT, ESCAT and QSCAT; and wind map over Empty Quarter	64
4.13	Temporal behavior of ECMWF wind and ψ_1 derived from NSCAT and ESCAT	66
4.14	Long-term temporal behavior of ECMWF wind and ψ_1 derived from ESCAT	66
5.1	Diagram showing surface and volume emission from sand	68
5.2	Diagram showing vertical temperature profile of sand subsurface . . .	70
5.3	T_b and ΔT_b θ dependence model simulations	71
5.4	Area of facet projection onto antenna beam	73
5.5	Computed T_b and ΔT_b ϕ -response for single facets	74
5.6	Longitudinal dune three-facet-model and its cross section	76
5.7	T_b and ΔT_b responses from model simulation over triple facet dune models and spaceborne radiometers at 19 GHz	77
5.8	Transverse dune three-facet-model and its cross section	78
5.9	Dual polarization 19 GHz T_b diurnal modulation from TMI and SSM/I over different sand surfaces	79
5.10	Dual polarization 19 GHz T_b azimuth angle modulation from TMI and SSM/I over different sand surfaces	80
5.11	ϕ - t_d sampling of data from combined TMI and SSM/I data	81
5.12	Surface of the T_b and ΔT_b model fits and slices through fits for a lon- gitudinal dune at 19 GHz	83
5.13	Simulated T_b and ΔT_b responses over triple facet dune models com- puted at 37 GHz	85
6.1	σ° θ response from bare dry soil and dense vegetation	90

6.2	Multi-spectral σ° versus θ from multiple radars	92
6.3	A and B images of Amazon computed from TRMM-PR and NSCAT σ° measurements	93
6.4	Multi-spectral V-pol σ° and T_b variation over different land cover types in the Amazon forest	95
6.5	A sub-region of Amazon basin comparing A values with and without spatial inhomogeneity model	97
6.6	σ° and T_b spatial inhomogeneity parameters	98
6.7	Multi-spectral σ° and T_b images of Amazon basin	100
6.8	Difference of Ku- and C-band A values	101
6.9	ESCAT and NSCAT σ° time series for different vegetation types . . .	103
6.10	Comparison of σ° spatial maps from SASS, NSCAT and QSCAT . . .	104
6.11	Time Series of A and B values from C- and Ku-band data	107
6.12	Slope of the ESCAT A decade long time series	108

Chapter 1

Introduction

Tropics have very diverse topographical, climatological, seasonal and biological characteristics. The land cover in the tropic and subtropical regions consists of both sand covered deserts and densely vegetated forests. Arid regions are defined to be the parts of tropics that receive less than 250 mm of annual rainfall. The physical processes in these areas are completely different than other terrestrial regions and mainly involve soil erosion, saltation and sedimentation. Aeolian processes, mainly driven by solar energy, continue to reshape the physical appearance of these regions.

Vegetation transforms solar energy into the chemical energy and recycles the soil nutrients that help sustain life on Earth. In addition to keeping oxygen-carbon dioxide balance in the atmosphere, it prevents soil erosion and recycles water through transpiration. The diminishing rain forest area has generated a great deal of concern by the scientific community during the last few decades. Many researchers believe that increased hydrocarbon-based-fuel consumption and reduction in global vegetation are a primary cause of CO₂ rise in the atmosphere, contributing to the greenhouse effect. The boundary areas of rain forests and deserts (such as Sahel) are wide transitional zones characterized by smooth change in vegetation density. These are very dynamic regions and their spatial location varies with climate and thus can serve as indicator of global climate change.

Due to the very large geographical sizes of deserts and rain forests, it has always been difficult to conduct detailed studies in such areas. Remote sensing has become an established tool for investigating and monitoring such vast regions. Microwave remote sensing instruments are of significant utility due to their sun and

weather independence. Microwave observations are sensitive to the surface, volume, geometric, and dielectric properties of the target. During the last few decades, many scientists have investigated and related these observations to key geophysical parameters of the target surface. However, many new questions have been raised and many still remain unanswered. This dissertation addresses some of these questions by developing and applying new methods to understand the relationship between microwave remote sensing data and geophysical parameters in the sand and vegetation.

1.1 Description of the Problem

Satellite microwave earth remote sensing has proven to be a very useful tool for studying various earth phenomena. Scatterometers (active remote sensors) and radiometers (passive remote sensors) measure radar backscatter (scattering) and radiometric temperature (emission), respectively, of the target surface. Radar backscatter (σ°) depends upon the geometrical and dielectric properties of the surface, whereas radiometric temperature (T_b) is a function of surface thermal, geometrical and dielectric characteristics. Moreover, the all weather coverage and sun independence of microwave instruments makes them suitable for studying tropical regions mostly covered with clouds. σ° and T_b vary with the look geometry and this dependence has been used to classify different land surface types.

In this dissertation, the Saharan ergs are investigated to relate the near surface winds and geophysical properties of sand formations to the radar and radiometric response. The governing electromagnetic scattering and emission processes are modeled and applied to the available scatterometer, precipitation radar and radiometer data to extract key geophysical parameters. The spatial and temporal variability of the Amazon forest is studied using data from multiple microwave sensors. Multi-frequency and multi-polarization data over the tropical vegetation is used to study differences between vegetation types. These goals are discussed further below.

Tropical Arid Regions

Although arid lands comprise nearly one-third of the Earth's land surface, the physical processes taking place in these regions are not fully understood. In the deserts, wind is a major agent of erosion, transportation, and sedimentation. These aeolian processes continue to shape the desert surface especially *Ergs*, which are vast expanses of sand. The wind action results in a variety of dune shapes and sizes. In 1941, Ralph A. Bagnold, a World War II veteran, pioneered the study of wind action over sand and reports his research in the book titled "*The Physics of Blown Sand and Deserts*" [1]. Since then a wide range of studies have been conducted to understand the aeolian processes of the deserts.

Deserts comprise more than 20% of the world's land surface. The Sahara and the Arabian deserts, collectively called Saharo-Arabian desert, represent the most spatially diverse terrain of the terresphere. About one-fourth area of Saharo-Arabian desert is composed of ergs. Beside small portion of flat terrain ergs, most of the area consists of dunes of different sizes, shapes and spatial orientations. Along with ergs, Saharo-Arabian desert consists of mountainous regions called *Hamadas* and boulder/gravel covered terrains called *Regs*. Due to the harsh climate and inaccessibility, there is very little *in-situ* data available over the desert regions. Very few investigators have used remote sensing tools to study such regions.

Ergs have very low moisture content and have a homogeneous, temporally stable distribution of dielectric constant. Thus, temporal variabilities of scattering and emission from sand are mainly a function of geometrical characteristics. Emission also has an additional dependence upon the thermal characteristics of sand.

View angle anisotropy of σ° and T_b measurements is used to study the sand surface geomorphology. The σ° measurements over ergs from the Ku-band NASA scatterometer (NSCAT), SeaWinds Scatterometer (QSCAT), Tropical Rain Monitoring Mission's Precipitation Radar (TRMM-PR), and C-band ERS Scatterometer (ESCAT), are used to study the surface characteristics. Dual polarization T_b measurements at various frequencies from the Special Sensor Microwave Imager (SSM/I)

aboard the Defense Meteorological Satellite Program (DMSP) and the TRMM Microwave Imager (TMI) are used to relate radiometric response of erg surfaces to the bedform geometrical characteristics. The bedform characteristics result from the aeolian processes induced by the prevailing wind. The European Centre for Medium-Range Weather Forecasts (ECMWF) predicted wind data is used to validate the results.

Tropical Vegetation

Natural vegetation cover is a collection of diverse plant species with varying characteristics and distributions. In tropical rain forests, many plant and animal species coexist symbiotically to form a naturally balanced ecosystem. With the increasing interest in tropical rain forests, many remote sensing tools have been developed to investigate vegetation characteristics such as spatial extent, distribution, concentration and temporal variability. These characteristics are interdependent and also depend on climatic and anthropogenic factors.

For a better understanding of vegetation dynamics, it is imperative that spatial boundaries and transitions be accurately mapped, different plant communities and their distribution be identified, and temporal variations be related to the climate. The topsoil underneath the vegetation cover plays an important role in the sustenance of biota through recycling chemical compounds necessary for life. In a forest, the vegetation cover type, distribution and density are dependent upon the characteristics of the soil. Radar backscatter measurements at large wavelengths have considerable contribution from soil.

The Amazon basin contains the largest tropical rain forest reserves of Earth. The Amazon basin has been studied extensively using both optical and microwave sensors. Long time series of σ° from multiple microwave sensors are available. Due to the temporal and radiometric stability of the Central Amazon, it has also been used to calibrate various spaceborne instruments. These data sets have been used individually to retrieve useful vegetation information and monitor changes. A comprehensive study involving data fusion of multi-frequency scatterometer and radiometer

data is required to better understand its relationship to geophysical parameters and processes.

QSCAT, ESCAT, NSCAT, Seasat scatterometer (SASS), TRMM-PR and SSM/I data are used to study the multi-spectral microwave response of Amazon vegetation. The multi-frequency signatures and spatial variations of σ° and T_b are also studied. Temporal variability of the Amazon basin is studied using C-band ERS data and a Ku-band time series formed by SASS, NSCAT and QSCAT data.

1.2 Research Contributions

Valuable contributions are made by this research in understanding the arid and vegetated areas of the tropics. These contributions include remote sensing applications to geophysical, multi-sensor, and modeling studies.

This research explains the σ° view angle response over ergs. It is shown that the σ° is mainly dependent upon the surface geometry of ergs. The slopes and orientations of the dune facets alter the σ° coupled θ and ϕ dependence. This dependence reflects the slopes and orientations of the dominant facets in the measurement footprint. The facets are modeled as tilted random surfaces with Gaussian tilt distribution. Simple dunes are modeled as simple geometrical shapes composed of tilted random surfaces and their σ° response is modeled as a weighted average of σ° response of individual tilted facets. The small scale ripples of the erg surface are treated as cosinusoidal ripples on the tilted facets and are modeled to result in Bragg scattering. This study is published in the *IEEE Transactions on Geoscience and Remote Sensing* [2] and in conference proceedings [3, 4, 5].

The next contribution of this research is the dynamic study of ergs and relationship between ECMWF predicted wind and dune orientations inferred from the σ° view angle behavior. Due to the large scatterometer measurement footprint size, the σ° measurements exhibit measurement centroid displacement variability which depends upon the spatial inhomogeneity of the erg surface. A new model is devised that takes into account both σ° view angle modulation and σ° spatial inhomogeneity. The model is sensitive to the observation θ and model parameters dependence on θ is

related to the erg surface characteristics. The parameters at incidence angle 30° – 35° are shown to provide orientations of the slip-sides which reflect the dominant wind directions on the surface. The seasonal variation of the dominant facet orientation and ECMWF winds is generally consistent. This work is currently in review for the *IEEE Transactions on Geoscience and Remote Sensing*.

Another contribution of this dissertation is the passive remote sensing of ergs. The research shows that spaceborne dual polarization T_b measurements are effected by the surface geometry of ergs. It is shown that TMI and SSM/I have a good inter-calibration and the T_b measurements from the two sensors in combination improve the azimuth-sampling density of the data. The difference of the two polarizations (ΔT_b) is independent of the thermal characteristics of the surface and is shown to exhibit ϕ -modulation related to the dominant facets in the measurement footprint. An empirical observation model is proposed to extract the ΔT_b ϕ -modulation in the raw T_b measurements. The extracted ϕ -modulation is shown to provide information about the dominant facets of the ergs. The research is published in the *IEEE Transactions on Geoscience and Remote Sensing* [6].

The last contribution of this research is a multi-spectral and multi-temporal microwave remote sensing of Amazon vegetation. The backscatter θ response is studied in relation to vegetation density. σ° and T_b measurements at different frequencies are used to differentiate between vegetation density. σ° and T_b spatial inhomogeneity model is related to the spatial geophysical characteristics of Amazon basin. C-band and Ku-band σ° time series from spaceborne scatterometers are used to identify areas of possible deforestation exhibited by reduced σ° response. The results indicate a possible mismatch between ERS-1 and ERS-2 scatterometers. Some of this work is published in *International Geoscience and Remote Sensing Symposium* conference proceedings [7, 8]. This material is in preparation for submission to *IEEE Transactions on Geoscience and Remote Sensing*.

1.3 Dissertation Outline

The dissertation provides a study of the remote sensing of ergs and vegetation. Various chapters address different but related problems of modeling active and passive microwave remote sensing and their application to extract important geophysical characteristics of ergs and vegetation. A brief outline of each chapter is given in the following paragraphs.

Chapter 2 provides a general background for the studies conducted in this dissertation. A review of the geophysical characteristics of the Saharan ergs and Amazon basin is also given. It also lists the characteristics of the scatterometers and radiometers used. A review of literature related to the geophysical characteristics and active and passive remote sensing of ergs and vegetation is also provided.

Chapter 3 provides the models to explain the σ° behavior of erg surfaces. Results of model simulation and model inversion of spaceborne σ° measurements are compared. In Chapter 4 the model is applied to perform spatial and temporal analysis of erg geometry to infer the wind directions. The wind direction results are compared to ECMWF predicted wind data. Chapter 5 explains the ϕ -modulation of spaceborne T_b measurements in relation to the erg surface geometry.

The results of multi-spectral and multi-temporal study of the Amazon basin are given in Chapter 6. Chapter 7 provides conclusions, and recommendations.

Chapter 2

Background

Spaceborne active and passive microwave remote sensing has proven to be a useful tool to study land surfaces. Many past and present instruments have shown the advantages of using microwave frequencies to study land and vegetation targets. This chapter provides a description of Saharan ergs and Amazon vegetation. It also provides details of the spaceborne scatterometers and radiometers used in this research and a review of previous work related to this dissertation. Section 2.1 introduces the erg bedforms and corresponding aeolian processes. The locations selected to do point based analysis are also described. Section 2.2 introduces the Amazon rain forest. Section 2.3 provides the active sensors and review of literature of active remote sensing of ergs and rain forest. The corresponding information about passive remote sensing is given in Section 2.4. An brief introduction to ECMWF winds is given in Section 2.5.

2.1 Sand and Wind

Deserts comprise more than 20% of the world's land surface [9]. Ergs constitute more than a quarter of the global desert surface [10]. Formed from sand, erg bedform morphology depends upon the grain size distribution of the inherent material. Sand is generally defined as particles 0.0625–2.0 mm in diameter [11]. The ergs of the Sahara consist of large sand-dune fields which are variable shapes due to the wind action. Aeolian processes such as wind erosion and sediment transport continue to reshape the dune fields which in turn govern the near surface wind patterns, thus resulting in diverse and dynamic bedforms [12]. Aeolian bedform research is relatively

recent. The first detailed analysis of erg geomorphology is presented in [1]. A detailed history of the aeolian bedform research is presented in [9] and [10].

The proportion of different particles and mixing of clay particles play an important role in the aeolian transport. Ergs consist of a hierarchy of aeolian bedforms consisting of three components called *ripples*, *dunes* and *draas*. Some erg areas also exist as sand sheets with no dominant dunes. Some sand sheets have small scale ripples due to wind action. Under the action of wind, sand grain entrainment and deposition result in surface undulations in the form of surface ripples. Surface ripple patterns are repetitive in the downwind direction and can have wavelengths of 1–25 cm and amplitudes of 0.2–5 cm. The ripples have a quick response to local wind variations that can indicate short term changes in the wind direction.

Dunes are formed by sand deposition over extended periods of time. They occur in various forms depending upon the prevailing wind regimes and available sand material. Dunes have 3–600 m wavelength and 0.1–100 m amplitude. Most dunes include at least one slip-side that is formed by the sand sliding from the dune summit and has a slope equal to the angle of repose of sand (30° – 35°). There may be other sides which have shallower slopes than the slip-side. The number of sides and their slopes are used to characterize the type of the dune [12].

Erg bedform hierarchies depend upon both sand and wind characteristics, including the wind speed and direction and their annual variabilities. The annual distribution of the wind direction may be characterized as narrow or wide unimodal, acute or obtuse bimodal, or complex (multi-modal) based on its directional variability over time. Narrow unimodal, wide unimodal and acute bimodal wind direction distributions result in *transverse* dunes where the dune axis is perpendicular to the average wind direction as shown in Fig. 2.1(a). The downwind side is a slip-side whereas the upwind side, called the windward-side, has a slope of 10° – 15° . For a limited supply of sand mass, similar wind regimes result in crescent shaped dunes (*barchans*) shown in Fig. 2.1(b). Obtuse bimodal wind direction distributions form *longitudinal* dunes [Fig. 2.1(c)] that have axes almost parallel to the average wind direction. Such dunes are characterized by two slip-sides, one on each side of the

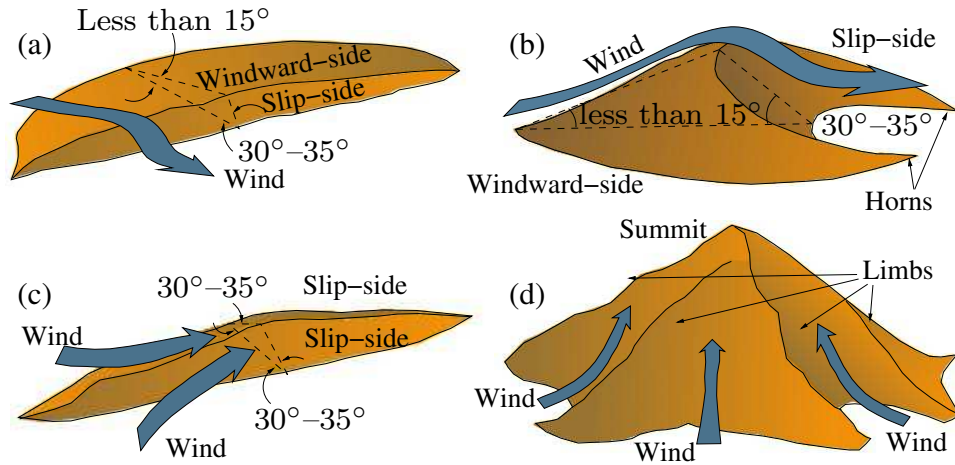


Figure 2.1: Diagram illustrating the shapes of a) transverse, b) barchan, c) longitudinal, and d) star dunes.

central ridge. Both transverse and longitudinal dunes can extend to a few kilometers and occur in the form of dune fields with inter-dune flat areas. Complex wind direction distributions result in complex dune formations. The most common formation is called a *star* or *pyramidal* dune [Fig. 2.1(d)] which has multiple limbs extending from a summit. Complex winds can also result in the complex forms consisting of mixtures of the simpler dune forms [11].

Nineteen sites in various ergs of the Sahara desert that include transverse, longitudinal and complex dune types are selected to study the σ° response from different dune shapes. A map showing the selected sites is presented in Fig. 2.2. The site information is extracted from [11] and summarized in Table 2.1.

2.2 Rain Forest

The Amazon basin presents a large geographical zone that has undergone significant land cover changes during the last few decades due to accelerated logging and other anthropogenic influences. Amazon forest consists of diverse types of vegetation, which vary with various geophysical factors, like latitude, moisture, rainfall etc. Amazonia has the most diverse plant life forms of the world and contains a large

fraction of the global biomass. The vegetation cover of Amazonia includes tropical moist forest (evergreen and semi-evergreen rain forest), dry forest (intergrading into woodland) and open grassy Savannah.

Vegetation plays an important role in regulating climate through its role in the global hydrological cycle. Thus, long-term changes in vegetation can also serve as indicators of climate change. In recent years, the research community has been concerned about diminishing rain forests. Spaceborne remote sensing with high resolution instruments has shown that the southern fringes of the Amazon rain forest have undergone most deforestation during the last decade. Time series data of low resolution microwave scatterometers can provide observations of large scale deforestation.

2.3 Active Microwave Remote Sensing

During the last few decades, active remote sensing of land surfaces has gained interest. Radar remote sensing has been extensively used to study vegetation but little attention has been given to the analysis of sand surface. σ° measurements from multiple instruments are available at different frequencies and time periods. This section describes the spaceborne active instruments used to conduct microwave backscatter study of the Saharan ergs and Amazon vegetation. A brief review of the literature is also given. This review provides an introduction to the models used to understand the σ° response of sand and vegetation.

2.3.1 Spaceborne Active Microwave Sensors

Low resolution non-imaging radars called scatterometers were initially designed to estimate near-surface ocean wind fields. The first spaceborne scatterometer, operating in Ku-band, flew aboard Skylab platform in 1973. Land observations of σ° from the Skylab scatterometer indicated the potential of scatterometer to study terrestrial features and processes [13]. Although the experiment was limited in

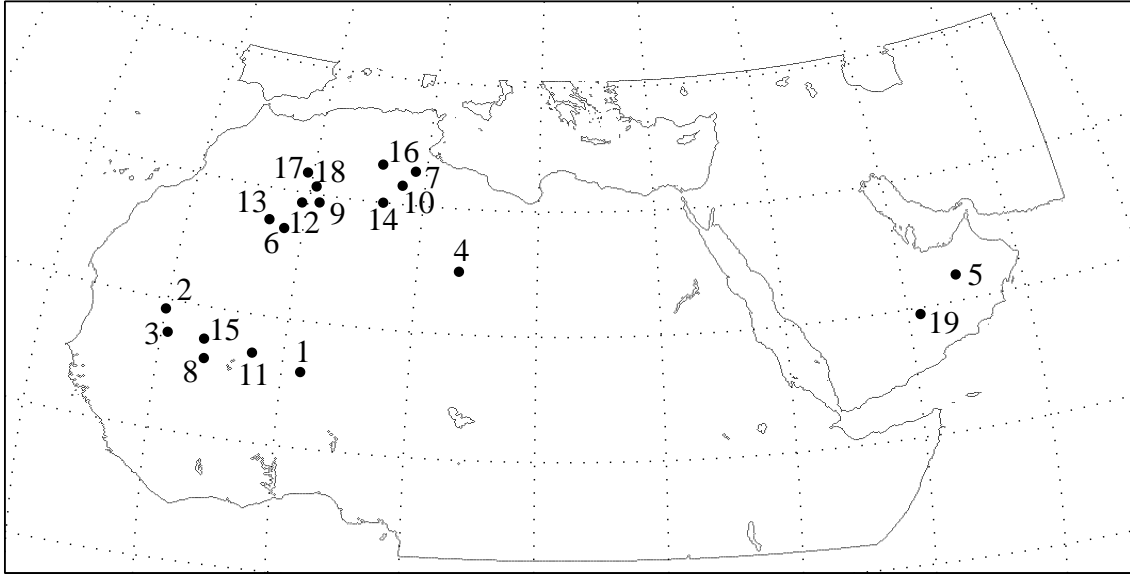


Figure 2.2: Map of the study area showing selected sites.

Table 2.1: Table listing the surface types over the selected study sites.

Location	Geographical Coordinates	Surface Dune Types
1	(16.00°N, 1.50°E)	Barchans
2	(19.25°N, 10.00°W)	Barchanoid Ridge
3	(17.50°N, 9.50°W)	Barchanoid Ridge
4	(25.00°N, 13.50°E)	Barchanoid Ridge
5	(22.00°N, 54.50°E)	Barchanoid Ridge
6	(27.00°N, 1.60°W)	Crescent Dunes Superimposed
7	(32.70°N, 9.00°E)	Fish-scale Pattern
8	(16.00°N, 6.25°W)	Linear Dunes
9	(29.40°N, 1.00°E)	Linear Dunes
10	(31.50°N, 8.00°E)	Linear Dunes
11	(17.00°N, 2.50°W)	Compound Linear Dunes
12	(29.20°N, 0.50°W)	Compound Linear Dunes
13	(27.50°N, 3.00°W)	Star Dunes Superimposed
14	(30.00°N, 6.50°E)	Chain Star Dunes
15	(17.50°N, 6.50°W)	Sand Sheets Streaks
16	(33.00°N, 6.00°E)	Sand Sheets Streaks
17	(31.60°N, 0.50°W)	Compound Sand Sheets Streaks
18	(30.60°N, 0.50°E)	Undifferentiated Complex Dunes
19	(19.50°N, 51.00°E)	Undifferentiated Complex Dunes

scope, the results were useful in designing future spaceborne microwave instruments. In 1978, Ku-band Seasat-A Satellite Scatterometer (SASS) flew aboard the Seasat satellite, which suffered an unfortunate failure after a hundred days of operation [14]. The instrument had four fan beam antennas operating in both horizontal (H-pol) and vertical (V-pol) polarizations making observations at 0° – 70° incidence angles. The combined ascending and descending pass data from four beams provided measurements at 8 different azimuth angles originally intended for ocean wind studies but has also been used for land studies. The small data set of global σ° thus produced has been studied for land and ice applications [15, 16, 17].

The failure of SASS led to a long data gap until 1991 when European Space Agency (ESA) launched first European Remote Sensing (ERS-1) Satellite with C-band Scatterometer ESCAT aboard. In 1996, ESA launched ERS-2 with an identical scatterometer aboard it to ensure an uninterrupted supply of C-band σ° data. ESCAT has three side-looking antennas operating at V-pol and provides near global coverage in 3-4 days. The σ° cover an incidence angle range of 18° – 57° and six azimuth angles from both ascending and descending passes [18].

In 1996, NSCAT, operating in Ku-band [19], was launched aboard Advanced Earth Observation Satellite (ADEOS). The instrument had six side looking antennas operating in H- and V-pol at 17° – 62° incidence angle range. Unfortunately, ADEOS suffered a solar panel failure after nine months of operation, once again disrupting the time series of Ku-band scatterometer σ° data.

In 1999, with a mission to quickly recover from the loss of NSCAT, NASA launched QuikScat with QSCAT aboard it [20]. QSCAT is a Ku-band instrument with two rotating pencil beam antennas operating in H- and V-pol at an incidence angle of 55° and 46° , respectively. The pencil beam design offers a very dense σ° sampling in the azimuth angle thus improving the ocean wind estimates.

The TRMM-PR, launched in 1997 aboard Tropical Rain Monitoring Mission (TRMM), is a narrow swath instrument and monitors the Earth's tropical regions [21]. TRMM-PR is a first of its kind sensor specifically designed to observe and measure the vertical profiles of precipitation to study the weather and storm structures.

It also provides near nadir V-pol Ku-band σ° measurements of the tropical surfaces covering an incidence angle range of 0° – 17° .

2.3.2 Active Microwave Remote Sensing of Sand

Radar backscatter from sand depends upon sand surface geometry and grain characteristics (grain size distribution, electrical permittivity, etc.). Very few researchers have used spaceborne remote sensing data to understand the geophysics of these surfaces. In a study of Egyptian desert using Shuttle Imaging Radars (SIR-A) data, Elachi et al. (1984) showed that imaging radar can image subsurface features for thin layer of low-loss material [22]. This effect was most pronounced in the horizontal polarization and large incidence angles.

Lancaster et al. (1992) used C-, L-, and P-band multipolarization radar data to study Kelso dunes in Mojave desert [23]. They found that backscatter from unvegetated dunes is controlled by dune topography and incidence angle of observation at all frequencies and polarizations. Blom et al. (1987) has reported similar observations using data from SASS, SIR-A, SIR-B, and SIR-C [24]. They also showed that unvegetated dune surfaces are quasi-specular reflectors at radar wavelengths. The return signal from these surfaces is significant when incidence angle equals the angle of repose of sand, and imaging direction is perpendicular to the dune trend.

σ° measurements over ergs have contributions from surface and volume scattering of the sand. Swift (1999) has provided a simple volume scattering [$\sigma_{vol}^\circ(\theta)$] model as a function of θ given by

$$\sigma_{vol}^\circ(\theta) = t^2 \left(\frac{n\sigma_b}{2\alpha} \right) \cos \theta \quad (2.1)$$

where t is the plane wave power transmission coefficient at θ , n is the number density of subsurface scatterers (cm^{-3}), σ_b is the backscatter cross section per particle (cm^2) and α is the bulk volume attenuation coefficient (cm^{-1}) [25]. The model is used to compute volume scattering of sea ice and can be used for sand with appropriate values of model parameters.

In order to model the backscatter from large-scale erg surface features (i.e., dunes) I adopt the general scattering model presented in [26]. The average co-polar scattering coefficient is expressed as a function of θ and ϕ given by

$$\sigma_{pp}^{\circ}(\theta, \phi) = \int_{-\infty}^{\infty} \int_{-\cot \theta}^{\infty} \sigma_{pp}(\theta', \phi) P_{\theta}(Zx', Zy') dZx dZy \quad (2.2)$$

where $\sigma_{pp}(\theta', \phi)$ is the generic response from the target surface as a function of local incidence angle (θ') and azimuth angle (ϕ). Zx and Zy are surface slopes in global x - and y -axis directions, respectively. The primed variables are in the local coordinate system defined by x' - and z' -axis in the wind flow and sensor direction, respectively. $P_{\theta}(Zx', Zy')$ is the joint probability function of the surface slope in the x' direction (Zx') and y' direction (Zy'). Zx' and Zy' are functions of Zx , Zy , θ and ϕ . The joint probability distribution is modeled as a function of incidence angle. This model is also described in [27] and [28]. A similar equation has been used in [29] for a two-scale model of polarimetric emissivity.

The shape of the small-scale ripples depends upon the angle of repose of the inherent material. The ripples are periodic in the wind direction and are skewed, resulting in two distinct sides. The downwind side is steeper than the windward side. The spectrum of sand surface ripples are narrow band. Thus, ripples are modeled as a cosinusoidal wave. The wavelength of the cosinusoid corresponds to the dominant wavelength of the ripple spectrum. The near surface wind direction changes rapidly over the undulating sand dune surface inducing local variabilities in the ripple direction.

The scattering from periodic surfaces results in enhanced response at discrete directions called Floquet modes. The derivation of the scattering amplitudes and directions of the modes is presented in [30]. The resulting Bragg scattering coefficient is a function of the surface orientation, surface ripple characteristics, incident wave characteristics and the Floquet mode considered. It is computed using incident

power (P_{inc}) and backscattered power (P_r) given by (Eqs. 3.2.61 and 3.2.62, [30])

$$P_{inc} = \frac{1}{2} \frac{\omega \epsilon}{k_s} \left(|a_0|^2 + \frac{\mu}{\epsilon} |a_0^{(h)}|^2 \right) \quad \text{and} \quad (2.3)$$

$$P_r = \frac{1}{2} \sum_n Re \left\{ \frac{\omega k_{zn}}{k_s^2} \left(\epsilon \frac{|b_n|^2}{|\beta_n|^2} + \mu \frac{|b_n^{(h)}|^2}{|\beta_n|^2} \right) \right\} \quad (2.4)$$

where n denotes the Floquet mode, ϵ and μ are electrical permittivity and permeability in free space, ω is the radian frequency of the incident wave. a_0 and $a_0^{(h)}$ are downward-going field amplitudes of the E- and H-waves. b_n and $b_n^{(h)}$ are upward-going field amplitudes of the E- and H-waves of the n th Floquet mode. $\beta_n = k_{zn}/k_s$, where k_s is the surface component of the wave number and k_{zn} is the z component of wave number of the n th Floquet mode.

σ° ϕ -modulation has been modeled with a second order harmonic equation given by

$$\sigma^\circ(\phi) = A + M_1 \cos(\phi - \phi_1) + M_2 \cos(2\phi - \phi_2) \quad (2.5)$$

where A is the mean σ° response of the surface. M_i and ϕ_i are the magnitude and phase of the i th harmonic. σ° ϕ -modulation is related to the surface gradient in Greenland [31]. In previous studies, σ° in the proximity of the point of interest (x_0, y_0) has assumed the surface to be homogeneous. This assumption does not apply in the areas of high spatial inhomogeneity such as Greenland [31] and Saharan ergs [14].

2.3.3 Active Microwave Remote Sensing of Forest

Spaceborne microwave remote sensing with its benefits of cloud penetration and sun independence provides a powerful tool to study extended areas like Amazon forest. Backscatter of the tropical rain forest exhibits temporal stability, spatial homogeneity and radiometric accuracy. These characteristics over the Amazon forest have been used for the external calibration and validation of many microwave instruments. The small data set of SASS scatterometer indicated the suitability of Amazon rain forest as a calibration target [16, 32], and later it was used to calibrate ESCAT aboard ERS-1 [18, 33] and ERS-2 [34]. A method for relative calibration was presented in [35], using SASS and ESCAT data, to correct errors in the σ° from different

antenna beams caused by the variations in the processing channel gain. A similar model was used to study bias in NSCAT σ° over the Amazon forest [36].

A few investigators have devised techniques to estimate surface moisture from the σ° measurements and found acceptable moisture distribution maps over various parts of the world [37, 38, 39]. Various land cover types of Amazon basin exhibit unique response in the different microwave bands. The σ° response with incidence angle has been used extensively to distinguish different land cover types. A simple model is a power law, expressed as

$$\sigma^\circ(\theta) = A + B(\theta - \theta_{ref}) \quad (2.6)$$

where A (in dB) is the σ° at $\theta = \theta_{ref}$ and B (in dB/°) is the slope of the line fit to the data at θ_{ref} [16, 32]. Long and Hardin (1994) have reported A and B responses derived from SASS σ° data for different vegetation classes in the Amazon basin [40, 41]. Similar analysis has been conducted by Mougín et al. (1995) using the ESCAT σ° measurements [42, 43, 44, 45, 46, 47]. Another study shows that TRMM-PR σ° measurements also provide a useful vegetation discriminant [48]. A cross calibration of TRMM-PR and NSCAT data has been conducted and, over Amazon basin, shows a bias of 4.7 dB at $\theta = 10.5^\circ$ [49]. TRMM-PR data has also been useful in observing diurnal changes in the Amazon vegetation [50].

Watt (1999) has shown that σ° temporal signatures over the Amazon vegetation are unique for various vegetation classes and has provided a methodology to perform vegetation classification based on temporal signature discrimination [51]. A similar study over the continent of Africa has also been conducted [52].

2.4 Passive Microwave Remote Sensing

Passive remote sensing provides useful information about the thermal characteristics of surface. Dual polarization T_b measurements at multiple frequencies are available and can provide useful insight into the thermal, dielectric and geometrical characteristics of the surface. This section describes the spaceborne passive instruments used to conduct microwave backscatter study of the Saharan ergs and Amazon

vegetation. A brief review of the literature is also given. This review provides an introduction to the models used to understand T_b response of sand and vegetation.

2.4.1 Spaceborne Passive Microwave Sensors

The SSM/I radiometers have operated aboard various Defense Meteorological Satellite Program (DMSP) satellites since 1990 [53, 54]. The SSM/I is a seven channel radiometer operating in dual polarization at 19, 37 and 85 GHz and in V-pol at 22.235 GHz. T_b values measured at 53.4° incidence angle, depend upon target physical temperature and emissivity and have been used for land surface type classification. The T_b observations of a target is considerably altered in the presence of clouds and various algorithms exist to remove this effect from the data [55].

The TMI is a nine channel radiometer operating in dual polarization at 10, 19, 37 and 85 GHz, and in V-pol at 22.235 GHz [56]. T_b is measured at 52.75° incidence angle. The orbit inclination of the TRMM satellite ($\approx 30^\circ$) results in shifting of the longitude of the ascending node every repeat cycle. This permits TMI T_b acquisition at various times-of-day, which can be used to study diurnal response of the target.

2.4.2 Passive Microwave Remote Sensing of Sand

Ergs have very low moisture content and have a homogeneous, temporally stable distribution of dielectric constant. Thus, the temporal variabilities of emission from sand are mainly a function of physical temperature and geometrical characteristics. Over a rough surface, T_b measurements are modulated by the look direction and also depend upon the frequency and polarization of the instrument.

Microwave emission are a function of surface thermal and geometrical characteristics and spaceborne radiometric temperature measurements have been used to classify different land surface types [57, 58, 59, 60, 61]. Azimuthal anisotropy of radiometric temperature has also been investigated. Yu [62] has reported directional radiometric temperature variations caused by canopy geometry and row structure in cultivated maize fields. Prigent et al. [63] reports insignificant azimuth angle dependence over dry sand surface whereas Macelloni et al. [64] combines spaceborne

radiometric temperature and backscatter measurements to study soil and vegetation. Some investigators have shown that there is strong azimuth angle modulation of microwave emission over the Antarctic surface caused by geometry of the surface [65].

Sand emission depends upon the desert surface geometry and volumetric dielectric and thermal characteristics. T_b is given by

$$T_b(\theta, \phi; f, p) = e(\theta, \phi; f, p)T \quad (2.7)$$

where θ and ϕ are the incidence and azimuth angles of observation, respectively, while f , p , T and e denote the frequency, polarization, physical temperature and emissivity, respectively. p is replaced by v and h for vertical and horizontal polarizations, respectively. For very dry soil, the electromagnetic wave penetration depth (δ_p) is approximately equal to its free space wavelength [27, 63]. The depth of sand that contributes to the measured T_b is called the sampling depth (τ) and is related to the penetration depth by $\tau \approx 3\delta_p \cos \theta$ [27]. For soils in the deserts, microwave radiation is estimated to come from soil layers down to depths of five wavelengths. The emission at frequencies greater than 15 GHz is proportional to the surface skin temperature [63].

Tsang et al. (2000) derived a radiometric emission model for a layered dielectric material (Eqs. 5.2.36a and 5.2.36b, [66]). This model is based on the fluctuating electromagnetic field theory of dissipative materials. The electromagnetic field is produced by the spontaneous local electric and magnetic moments arising from the thermally-induced random motion of its charges. This model is derived for a stratified material with a temperature profile (see Fig. 2.3) and is given by

$$\begin{aligned} T_{bh}(\theta) = & \frac{k_0}{\cos \theta} \sum_{l=1}^n \frac{\epsilon_l'' T_l}{2\epsilon_0} \left\{ \frac{|A_l|^2}{k_{lz}''} (e^{2k_{lz}'' d_l} - e^{2k_{lz}'' d_{l-1}}) - \frac{|B_l|^2}{k_{lz}''} (e^{-2k_{lz}'' d_l} - e^{-2k_{lz}'' d_{l-1}}) \right. \\ & \left. + \frac{iA_l B_l^*}{k_{lz}'} (e^{-i2k_{lz}' d_l} - e^{-i2k_{lz}' d_{l-1}}) - \frac{iA_l^* B_l}{k_{lz}'} (e^{i2k_{lz}' d_l} - e^{i2k_{lz}' d_{l-1}}) \right\} \\ & + \frac{k}{\cos \theta} \frac{\epsilon_t'' T_t}{2\epsilon_0 k_{tz}''} |T_{01}^{TE}|^2 e^{-2k_{tz}'' d_n} \quad \text{and} \end{aligned} \quad (2.8)$$

$$\begin{aligned}
T_{bv}(\theta) = & \frac{k_0}{\cos \theta} \sum_{l=1}^n \frac{\epsilon_l'' T_l (|k_{lz}|^2 + k_x^2)}{2\epsilon_0 |k_l|^2} \\
& \times \left\{ \frac{|C_l|^2}{k_{lz}''} (e^{2k_{lz}'' d_l} - e^{2k_{lz}'' d_{l-1}}) - \frac{|D_l|^2}{k_{lz}''} (e^{-2k_{lz}'' d_l} - e^{-2k_{lz}'' d_{l-1}}) \right. \\
& \quad + \left(\frac{|k_{lz}|^2 - k_x^2}{|k_{lz}|^2 + k_x^2} \right) \frac{C_l D_l^*}{i k_{lz}'} (e^{-i2k_{lz}' d_l} - e^{-i2k_{lz}' d_{l-1}}) \\
& \quad \left. - \left(\frac{|k_{lz}|^2 - k_x^2}{|k_{lz}|^2 + k_x^2} \right) \frac{C_l^* D_l}{i k_{lz}'} (e^{i2k_{lz}' d_l} - e^{i2k_{lz}' d_{l-1}}) \right\} \\
& + \frac{k}{\cos \theta} \frac{\epsilon_t'' T_t (|k_{tz}|^2 + k_x^2)}{2\epsilon_0 k_{tz}'' |k_t|^2} |T_{01}^{TM}|^2 e^{-2k_{tz}'' d_n} \tag{2.9}
\end{aligned}$$

where k_0 , θ and ϵ_0 are the wave number, incidence angle and electrical permittivity in the air, respectively. The i is the imaginary number $\sqrt{-1}$. The stratified subsurface has $n + 1$ layers where the $(n + 1)$ th ($= t$ th) layer extends infinitely below the n th layer. d_{l-1} and d_l denote the distance of the l th layer's upper and lower boundaries,

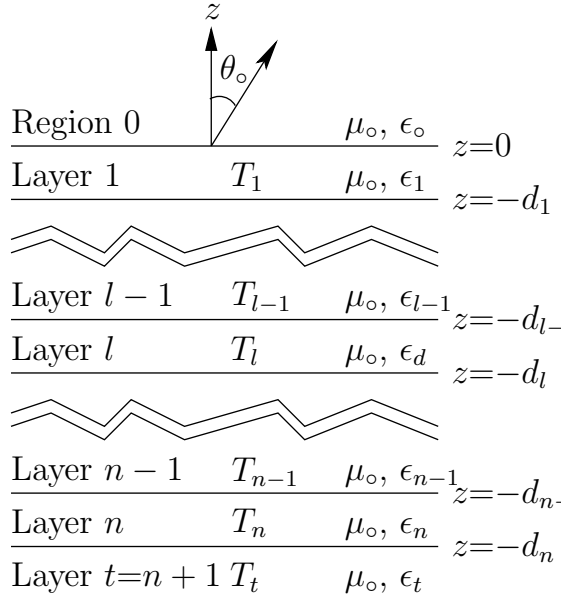


Figure 2.3: Diagram showing the stratified sand subsurface used to compute radio-metric emission.

respectively, from the air-sand boundary. k_l and k_{lz} are the wave number and its z component of the l th layer in the sand, respectively. ϵ_l'' and k_{lz}'' denote the imaginary parts of complex electrical permittivity and k_{lz} of the l th layer in the sand, respectively. k_t , k_{tz} , ϵ_t'' and k_{tz}'' correspond to the t th layer. $k_x = k_0 \sin \theta$ is the surface component of incident wave number. T_{01}^{TE} and T_{01}^{TM} denote the transmission coefficients between air and sand for H- and V-pol, respectively. A_l and B_l denote the amplitudes of upward and downward H-pol waves, respectively. C_l and D_l are the corresponding amplitudes of V-pol waves. T_l and T_t are the physical temperatures of l th and t th layer, respectively. In the derivation of Eqs. 2.8 and 2.9, Tsang [66] has taken into account the effect of reflections between layers.

2.4.3 Passive Microwave Remote Sensing of Forest

Passive microwave remote sensing has contributed significantly to the global study of vegetation. The radiometric emission from rain forest consist of contribution from soil and vegetation. The emissivity has a strong dependence on the moisture content [67, 68].

Amazon basin land cover types exhibit unique radiometric response in the different microwave bands. Neale et al. (1990) reported T_b responses derived from SSM/I channels for dense vegetation in the Amazon basin [60]. Hardin et al. (1996) combined the ESCAT, SSM/I imageries with optical spaceborne data that helped improve classification accuracy [69].

Airborne passive remote sensing has shown sensitivity of multi-frequency emission to forest type and biomass. The normalized difference of temperatures at different frequencies is sensitive to crown transparency and has the potential to monitor vegetation stress condition [70]. Macelloni et al. (2003) has also demonstrated the potential of combining ESCAT and SSM/I data to categorize land surface types [64].

2.5 ECMWF Winds

The European Centre for Medium-Range Weather Forecasts (ECMWF) provides global wind fields generated by a numerical weather prediction model using meteorological data as input. The input wind data is acquired from various sources such as meteorological stations and spaceborne sensors. The predicted winds are spatial and temporal interpolations via a complex global weather model [71]. The data is provided over a regular grid of $1^\circ \times 1^\circ$ every 6 hours.

Chapter 3

Microwave Backscatter Modeling of Erg Surfaces – Static

Radar backscatter over ergs depends upon the geometrical and dielectric properties of the surface and varies with the look geometry. In this chapter, $\sigma^\circ(\theta, \phi)$ measurements as a function of θ and ϕ are used to study the sand surface geomorphology of Saharan ergs. The σ° measurements from NSCAT, ESCAT, QSCAT and TRMM-PR are used.

Simple models are presented to relate the scatterometer backscatter to surface orientation probability distributions termed as tilt distribution and surface ripple distribution. Section 3.1 provides models to represent $\sigma^\circ(\theta, \phi)$ for large- and small-scale erg structures. The results of the forward projection of the proposed model over simulated surfaces are compared to the observed data from spaceborne sensors in Section 3.2. This material has been published in [2, 3, 4, 5].

3.1 Surface Backscatter Model

The total backscattering coefficient σ° from the sand as a function of incidence and azimuth angle is modeled as

$$\sigma^\circ(\theta, \phi) = \sigma_{surf}^\circ(\theta, \phi) + \sigma_{vol}^\circ(\theta) \quad (3.1)$$

where $\sigma_{surf}^\circ(\theta, \phi)$ is surface scattering in the θ, ϕ direction and $\sigma_{vol}^\circ(\theta)$ is volume scattering as a function of incidence angle. The model is shown pictorially in Fig. 3.1. The volume scattering component results from incident electromagnetic waves that have penetrated into the subsurface. Sand material generally has a very low dielectric constant and this allows the electromagnetic waves to penetrate as deep

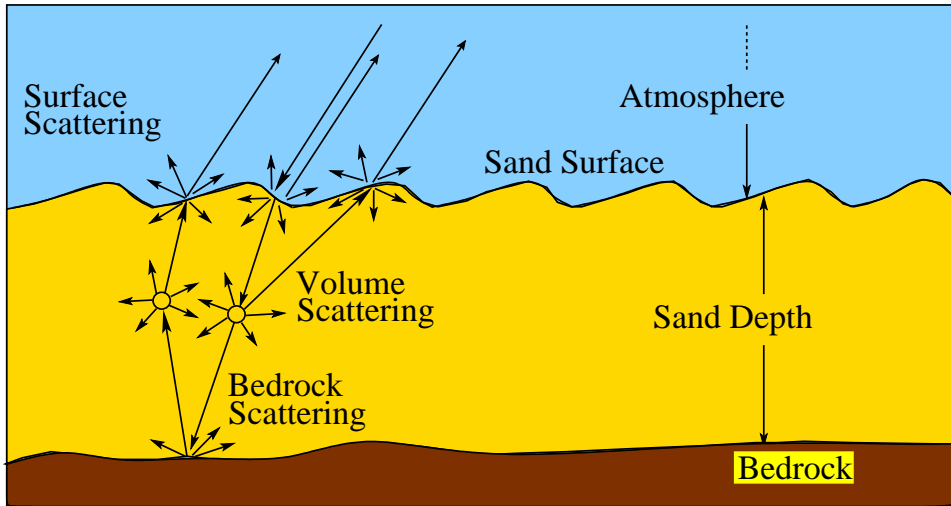


Figure 3.1: Diagram showing a simple sand surface with surface and volume scattering components.

as the parent bedrock, depending on the moisture content of the sand. Scattering from the subsurface is primarily caused by the sand particles that are assumed to be homogeneous and result in isotropic backscattering. A simple volume scattering model given in Eq. 2.1 is used to estimate the volume backscatter contribution [25]. I use nominal values for the model parameters in Eq. 2.1, e.g. the number density of sand particles of $4000 \text{ particles/cm}^3$, a cross section per scatterer of 10^{-8} cm^2 , and an attenuation coefficient of 0.05 cm^{-1} . With these values, the sand volume scattering contribution (Fig. 3.2) is estimated to be small (-5 dB or less) relative to the total scattering so that the volume scattering component can be ignored and model the return backscatter as the contribution from only the sand surface.

Surface scattering is predominantly due to the geometrical characteristics of the surface. The erg surface profile has two main spatial frequency components, corresponding to the two predominant land features. The low spatial frequency (wave number) components are due to large scale dunes whereas the high wave number components are due to small ripples on the surface of the dunes. The surface scattering coefficient consists of contribution from large scale dunes and small scale ripples on

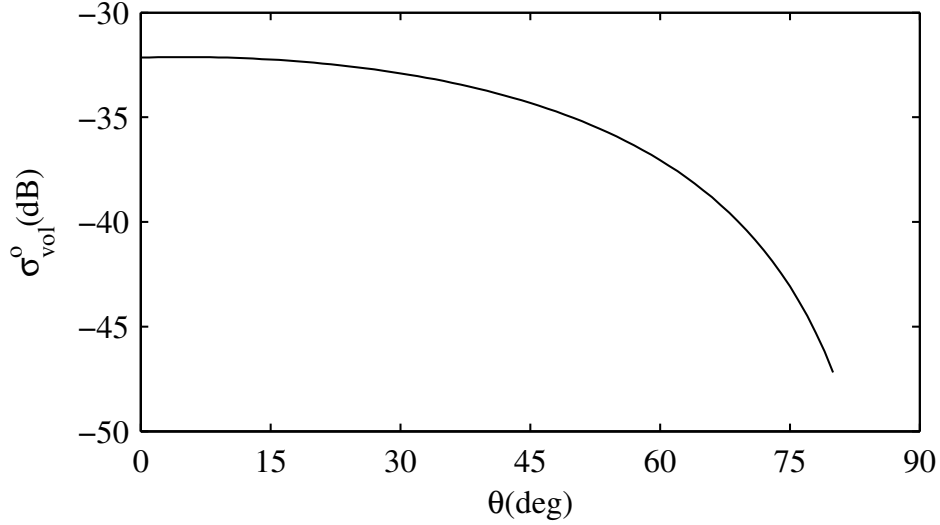


Figure 3.2: Plot showing volume scattering from sand as a function of incidence angle computed using Eq. 2.1 and parameter values given in the text.

the dunes. The contribution from small scale ripples is dominated by Bragg scattering that occurs at discrete θ and ϕ directions. The look directions at which Bragg scattering occurs are dependent on the spectrum of the small scale ripples.

In next subsection, a model of σ_{surf}° is proposed and constitutes composite tilted rough facets. This model relates the surface $\sigma^\circ(\theta, \phi)$ response to the weighted sum of responses from dominant facets on the surface (Section 3.1.1). The area covered by different facets is used to identify the type of dunes. Scattering from small ripples is modeled as Bragg scattering where the ripples are modeled as cosinusoidal surface waves (Section 3.1.2).

3.1.1 Rough Facet Model

Eq. 2.2 is modified to use the probability density function of the surface tilt angles. The backscatter from a single rough facet (σ_{facet}°) is modeled as

$$\sigma_{facet}^\circ(\theta, \phi) = \int_0^{2\pi} \int_0^{\frac{\pi}{2}} P(\theta_s, \phi_s) \sigma_s(\theta', \phi') u(\theta_g - \theta) d\theta_s d\phi_s \quad (3.2)$$

where the integration is over all possible tilts in the upper hemisphere. $P(\theta_s, \phi_s)$ is the tilt distribution of the facet and $\sigma_s(\theta', \phi')$ is the flat surface response of the sand material. θ' and ϕ' are local incidence and azimuth angle for each facet, respectively. θ_g is the facet grazing angle and $u(\theta_g - \theta)$ is a unit step function that results in zero response when $\theta > \theta_g$.

The sand dune field is modeled as a composite of tilted rough facets. The $\sigma_{dunes}^\circ(\theta, \phi)$ component of the scatterometer measurement is the sum of the returns from all the rough facets in the footprint. It is given by

$$\sigma_{dunes}^\circ(\theta, \phi) = \sum_n F_n \int_0^{2\pi} \int_0^{\frac{\pi}{2}} P_n(\theta_s, \phi_s) \sigma_s(\theta', \phi') u(\theta_g - \theta) d\theta_s d\phi_s \quad (3.3)$$

where the summation is over all facets in the footprint and F_n is the fraction of the footprint area covered by the n th rough facet. $P_n(\theta_s, \phi_s)$ is the tilt distribution of the n th rough facet. The model states that the returned power from the dune field, when an electromagnetic wave is incident from θ and ϕ direction, is the sum of the contributions from all the surface slopes oriented to contribute to the return signal within the beam illuminated area. The unit step function $u(\theta_g - \theta)$ assures zero return when a tilted facet is not illuminated.

NSCAT V-pol and TRMM-PR σ° measurements are used to estimate the flat surface Ku-band $\sigma_s(\theta', \phi')$ response of the surface. For a flat surface the sensor incidence angle and local incidence angle have the same value, i.e., $\theta' = \theta$. Moreover, the response is independent of ϕ and can be written as $\sigma^\circ(\theta', \phi') = \sigma^\circ(\theta)$. NSCAT V-pol σ° observations are made over a 17°-62° incidence angle range at ten azimuth angles whereas TRMM σ° are at near nadir 0°-17° incidence angles and have very narrow azimuth angle range. Figure 3.3(a) shows $\sigma^\circ(\theta')$ for NSCAT V-pol and TRMM-PR measurements over location 15 (see Fig. 2.2). The quadratic fit through the data is used to represent the flat surface response with no dependence on ϕ' . Lacking σ° measurements for $\theta' > 62^\circ$, a quadratic roll off is assumed at grazing angles ($\theta' > 62^\circ$). Figure 3.3(b) shows the azimuth angle response of σ° which has been corrected for incidence angle dependence.

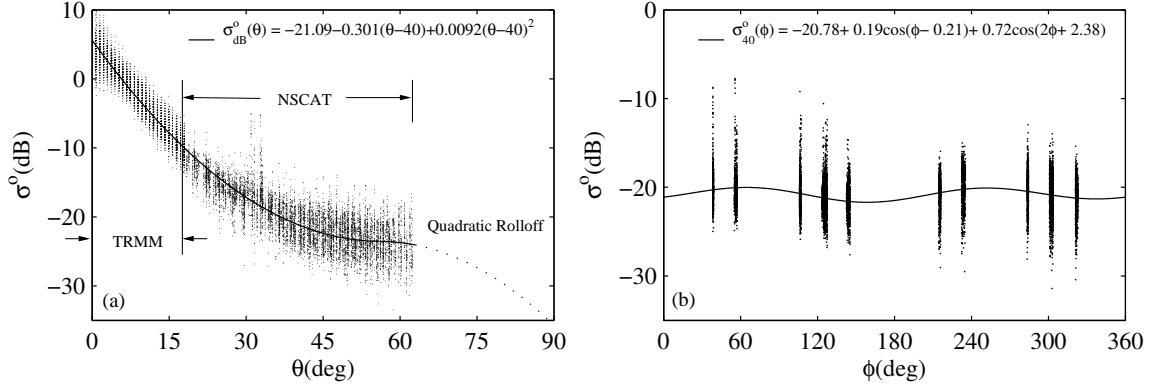


Figure 3.3: (a) σ^o incidence angle response at Ku-band from combined TRMM and NSCAT data, which is assumed to be the flat surface response of sand that does not vary with ϕ . A quadratic roll off close to the grazing angles is assumed, given by $\sigma_{dB}^o = -56.51 + 1.177\theta - 0.0105\theta^2$. (b) σ_{40}^o vs ϕ with second order harmonic fit where σ_{40}^o is incidence angle corrected σ_{dB}^o normalized to 40° i.e., $\sigma_{40}^o = \sigma_{dB}^o + 0.301(\theta - 40^\circ) - 0.0092(\theta - 40^\circ)^2$.

In general, it is difficult to determine the probability distribution of the surface angles. However, by modeling sand dunes as composed of a finite number of rough facets, an estimate of the probability distribution can be made. For example, a transverse dune with a slip- and a windward-side can be modeled as two rough facets tilted at $(30^\circ\text{-}35^\circ, \phi_n)$ and $(10^\circ\text{-}15^\circ, \phi_n + 180^\circ)$ mean tilt respectively. A third facet at $(0^\circ, 0^\circ)$ accounts for inter-dune flat area in dune fields.

Lacking a better model, the surface tilt distribution is assumed to be Gaussian. If $\alpha = [\theta_s, \phi_s]$ represents a vector whose elements are the tilt angles of the facet, then a two-dimensional Gaussian distribution for the surface tilt is given by

$$P(\theta_s, \phi_s) = P_\alpha(\alpha) = \frac{1}{2\pi\sqrt{|R_\alpha|}} e^{-\frac{1}{2}(\alpha - \mu_\alpha)R_\alpha^{-1}(\alpha - \mu_\alpha)^T} \quad (3.4)$$

where $\mu_\alpha = [\theta_n, \phi_n]$

and $R_\alpha = \begin{bmatrix} \varsigma_\theta^2 & \varsigma_{\theta\phi} \\ \varsigma_{\phi\theta} & \varsigma_\phi^2 \end{bmatrix}$.

θ_n and ϕ_n are the mean values of θ_s and ϕ_s . ς_θ and ς_ϕ are the corresponding standard deviations. $\varsigma_{\theta\phi} = \varsigma_{\phi\theta}$ is the covariance of θ and ϕ .

3.1.2 Cosinusoidal Ripple Model

The sand surface is modeled as a composite of tilted rough facets with cosinusoidal ripples (corresponding to the small ripples). Figure 3.4(a) depicts one such tilted rough facet. $\hat{\mathbf{n}}$ denotes the rough facet unit normal vector that is oriented in the (θ_s, ϕ_s) direction in spherical coordinates. The rough facet is characterized by a probability distribution of tilt $P(\theta_s, \phi_s)$ with a mean (θ_n, ϕ_n) . \mathbf{k} denotes the incident wave vector with a wavelength λ and wave number $k = 2\pi/\lambda$. It is represented by (k, θ, ϕ) in spherical coordinates where θ and ϕ are the incidence and azimuth angles of the incident wave. $\hat{\mathbf{k}}_g$ is a unit vector in the direction of the projection of \mathbf{k} on the facet. The incidence angle of $\hat{\mathbf{k}}_g$ is called grazing angle (θ_g) which depends on the facet tilt θ_s and sensor azimuth angle ϕ . For $\theta > \theta_g$ the facet is not illuminated. \mathbf{K} represents the wave vector of the surface cosinusoidal ripples with wave length λ_s and wave number $K = 2\pi/\lambda_s$. (K, θ_K, ϕ_K) are the spherical coordinates of \mathbf{K} . \mathbf{K} is always perpendicular to $\hat{\mathbf{n}}$. Vectors $\hat{\mathbf{n}}$, \mathbf{k} and \mathbf{K} define the sensor-surface geometry. The transformation to the local or natural coordinate system of the tilted facet gives us the local incidence (θ') and azimuth (ϕ') angles of the sensor. The derivation of θ' , ϕ' and θ_g is given in the Appendices A.1, A.2 and A.3, respectively. Models for both large- and small-scale surface scattering are described in the next two subsections. In this section ripples are treated as not having any directional variability.

The scattering from the sand surface ripples is mostly Bragg scattering. The derivation of Bragg backscattering look directions for a given surface tilt and cosinusoidal ripple is given in the Appendix A.3. For the surface geometry given by $\hat{\mathbf{n}}$ and \mathbf{K} , the incident wave vector \mathbf{k} that results in Bragg backscattering obeys the following conditions

$$(\hat{\mathbf{K}} \times \hat{\mathbf{n}}) \cdot \hat{\mathbf{k}} = 0 \text{ and } \hat{\mathbf{K}} \cdot \hat{\mathbf{k}} = -\frac{mK}{2k}. \quad (3.5)$$

The first condition means that $\hat{\mathbf{k}}$ lies in the plane formed by $\hat{\mathbf{n}}$ and $\hat{\mathbf{K}}$, i.e., the incident wave is directed along the direction of periodicity. The second condition is equivalent to $\sin \theta' = mK/2k$, specifying the Bragg incidence angles on a flat surface. The

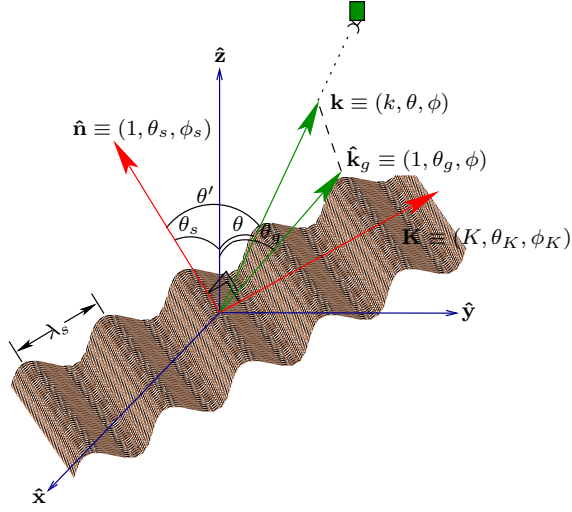


Figure 3.4: Model of tilted rough facet with cosinusoidal surface ripples.

solution of these two equations is given by

$$\hat{\mathbf{k}}_m = \pm \sqrt{1 - \left(\frac{mK}{2k}\right)^2} \hat{\mathbf{n}} - \frac{mK}{2k} \hat{\mathbf{K}} \quad (3.6)$$

where $\hat{\mathbf{k}}_m$ is the incident wave vector that results in backscatter of m th Floquet mode. The backscatter response from a cosinusoidal surface ripple is

$$\sigma_{wave}^{\circ}(\theta, \phi) = \sum_m \sigma_B(\hat{\mathbf{n}}, \mathbf{K}, h, \mathbf{k}, \hat{\mathbf{e}}, m) \delta(\hat{\mathbf{k}} - \hat{\mathbf{k}}_m) \quad (3.7)$$

where $\sigma_B(\hat{\mathbf{n}}, \mathbf{K}, h, \mathbf{k}, \hat{\mathbf{e}}, m)$ is the Bragg scattering coefficient, h is the surface wave amplitude, and m is the Floquet mode. $\hat{\mathbf{e}}$ denotes the polarization of the incident wave. The delta function in the model assures that only modes in the backscatter direction contribute. The zeroth order mode Bragg backscattering direction ($\hat{\mathbf{k}}_0$) occurs when $\hat{\mathbf{k}} = \hat{\mathbf{n}}$. Bragg backscattering from surface ripples occurs only at discrete points in the θ - ϕ space which are symmetric about the zeroth order mode direction. The Bragg backscatter directions closer to the zeroth order mode direction have a relatively higher backscattering return that decreases at higher local incidence angles.

The sand ripples are periodic and band limited; hence, the total backscatter for N surface cosinusoids is

$$\sigma_{ripples}^{\circ}(\theta, \phi) = \sum_{n=1}^N \sum_m \sigma_B(\hat{\mathbf{n}}, \mathbf{K}_n, h_n, \mathbf{k}, \hat{\mathbf{e}}, m) \delta(\hat{\mathbf{k}} - \hat{\mathbf{k}}_m) \quad (3.8)$$

where \mathbf{K}_n and h_n are the n th surface cosinusoidal ripple's wave vector and amplitude, respectively.

Eq. 3.8 incorporated in Eq. 3.3 results in a model of the total surface backscatter. In Eq. 3.3, $\sigma_s(\theta', \phi')$ is estimated from observed σ° measurements and *a priori* has contribution from the small ripples. The small-scale ripple characteristics of sand change rapidly. In order to analyze the affect of the large-scale dune structures, the contribution of small-scale ripples is ignored. With this assumption, the problem at hand is simplified as shown in the next section.

3.2 Rough Facet Model Simulation

In this section, model simulations over simple dunes (transverse and longitudinal) are presented. First, the result for a single rough facet is illustrated. Figure 3.5 shows the modeled backscatter response from a single rough surface facet with a Gaussian tilt distribution with $\theta_n=30^{\circ}$, $\phi_n=75^{\circ}$, $\varsigma_{\theta}=\varsigma_{\phi}=1$ and $\varsigma_{\theta\phi}=0$. Although covariance between θ_s and ϕ_s is related through the wind characteristics and the grain distribution, in this analysis I assume θ_s and ϕ_s are uncorrelated in order to keep the simulation simple. The $\sigma_s(\theta)$ used is the quadratic fit and extension from Fig. 3.3. The simulated $\sigma^{\circ}(\theta, \phi)$ response peaks when $\theta=\theta_n$ and $\phi=\phi_n$ and thus clearly reflects the facet characteristics. The standard deviations of the tilt angles affect the height of the peak and gradient in its vicinity. The parabolic bite at high incidence angles corresponds to directions beyond the grazing angle of the facet and hence do not result in any backscattering.

When modeled as composed of rough surface facets, the $\sigma^{\circ}(\theta, \phi)$ response of dunes is the linear combination of the individual rough facet responses. The next two subsections describe the rough surface facet models for transverse and longitudinal dunes and their $\sigma^{\circ}(\theta, \phi)$ response when applied to the model. The results are

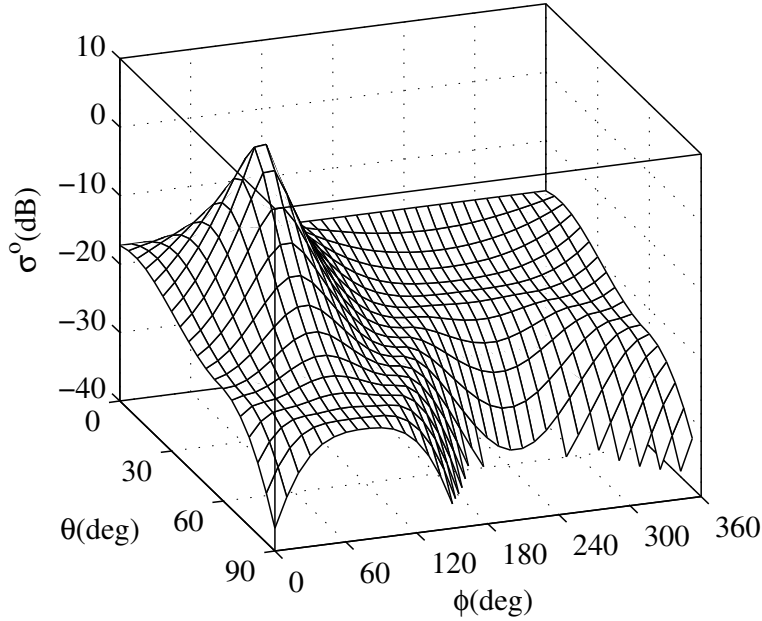


Figure 3.5: Model σ° response (Equation 3.2) from a single rough surface facet with $\theta_n=30^\circ$, $\phi_n=75^\circ$ and Gaussian tilt distribution having $\varsigma_\theta=\varsigma_\phi=1$, $\varsigma_{\theta\phi}=0$ with $\sigma_s = -21.09 - 0.301(\theta - 40^\circ) + 0.0092(\theta - 40^\circ)^2$

compared to the observations made by NSCAT and ESCAT over areas of known dune types.

3.2.1 Longitudinal Dune

A longitudinal dune has two opposite slip-sides. The slip-sides have a slope equal to the angle of repose of the parent sand which is nominally taken to be 30° - 35° and corresponds to a mean tilt angle of θ_n . The azimuth orientation of the two slip-sides are, in general, separated by 180° .

In order to model the longitudinal dune field, the $\sigma^\circ(\theta)$ and $\sigma^\circ(\phi)$ responses observed by NSCAT, ESCAT and QSCAT are analyzed. Figure 3.6 illustrates the azimuth angle modulation of σ° observations at $(17.5^\circ\text{N}, 15.35^\circ\text{W})$. NSCAT and ESCAT give similar results in which the two maxima correspond to the orientation of the two slip-sides of the longitudinal dune. The two maxima are separated by

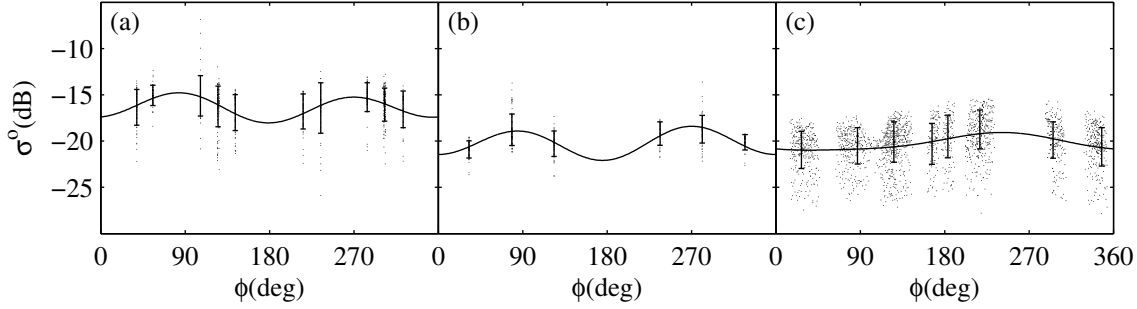


Figure 3.6: σ° azimuth angle response over a longitudinal dune field at (17.5°N, 15.35°W) from (a) NSCAT V-pol for θ in the range 30°-35°, (b) ESCAT for θ in the range 30°-35°, and (c) QSCAT for $\theta=55^\circ$. Solid line is a second order harmonic fit.

approximately 180° in azimuth. The NSCAT and ESCAT incidence angles in Fig. 3.6 result in normal local incidence angle observation of the slip-sides at the azimuth angles of the graph maxima. Since these slip-sides are a result of an average wind direction parallel to the axis of the dune, the average wind direction producing this dune lies between the two peaks with an ambiguity of 180°. The ESCAT σ° is lower than NSCAT due to its longer wavelength resulting in greater penetration and thus higher loss. QSCAT has reduced ϕ -modulation because of its high incidence angle which does not result in normal incidence angle observation of the slip-sides.

The effect of slip-sides in the observed σ° is further confirmed by analyzing the $\sigma^\circ(\theta)$ response at the azimuth angles corresponding to the maxima in azimuth modulation. Figure 3.7 presents such plots for both ESCAT and NSCAT measurements. The data is fit with a non-parametric line curve. A rise in the σ° measurements in the 30°-35° incidence angle range is observed, particularly in Figs. 3.7(a) and 3.7(c).

The analysis of $\sigma^\circ(\theta)$ and $\sigma^\circ(\phi)$ responses from the observed data confirms that the σ° behavior can be explained by considering the sides of the longitudinal dune as rough facets. The longitudinal dune field is modeled as two tilted rough facets and a flat rough facet between parallel dunes. Figure 3.8 shows the correspondence between a typical longitudinal dune and the rough facet model. The two rough facets

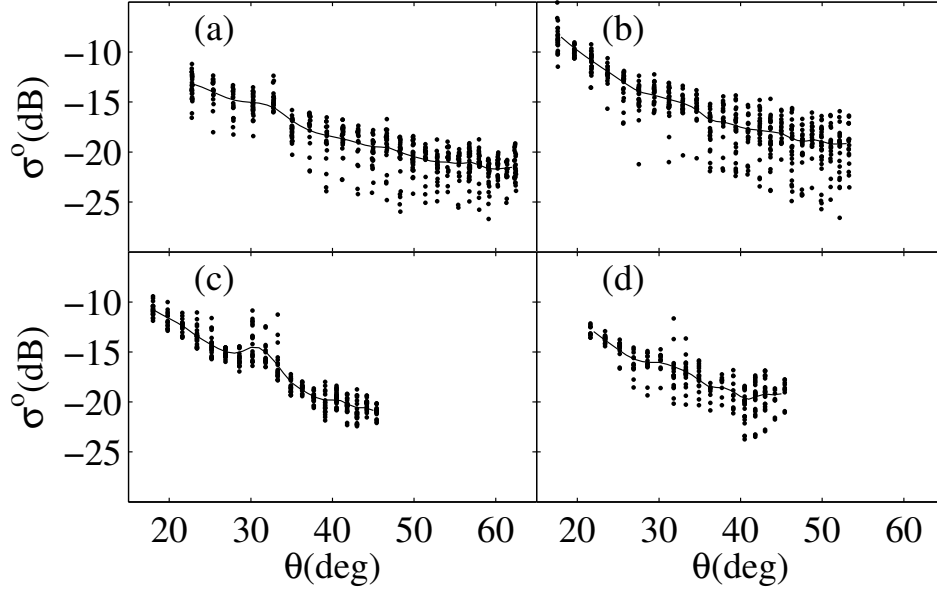


Figure 3.7: σ° incidence angle response over a longitudinal dune field at (17.5°N, 15.35°W) from NSCAT V-pol and ESCAT. (a) and (b) are NSCAT measurements at $\phi=56^\circ$ and $\phi=284^\circ$, respectively. (c) and (d) are ESCAT measurements at $\phi=79^\circ$ and at $\phi=218^\circ$, respectively.

have mean tilts ($32^\circ \pm 2^\circ$, ϕ_n) and ($32^\circ \pm 2^\circ$, $\phi_n + 180^\circ$) and the third rough facet with mean tilt (0° , 0°) (flat) is used to represent the inter-dune space in a longitudinal dune field. All of these facets are modeled with a Gaussian tilt distribution. The fraction of the footprint covered by each slip-side (F_s) is the same due to the symmetry of the longitudinal dunes and hence the flat rough facet covers a $F_f = 1 - 2F_s$ fraction of the footprint.

In order to apply Equation (3.3) as a forward model, the order of integrations and summation is interchanged to obtain

$$\sigma_{dunes}^\circ(\theta, \phi) = \int_0^{2\pi} \int_0^{\frac{\pi}{2}} P_T(\theta_s, \phi_s) \sigma_s(\theta', \phi') u(\theta_g - \theta) d\theta_s d\phi_s \quad (3.9)$$

where $P_T(\theta_s, \phi_s) = \sum_n F_n P_n(\theta_s, \phi_s)$ is the weighted total of the tilt distributions of the dominant facets in the footprint. Figure 3.9(a) shows the cumulative tilt distribution for the modeled longitudinal dune field. The two peaks at (30° , 60°) and (30° , 240°) are due to two slip-sides with equal weights of 25% and the third long

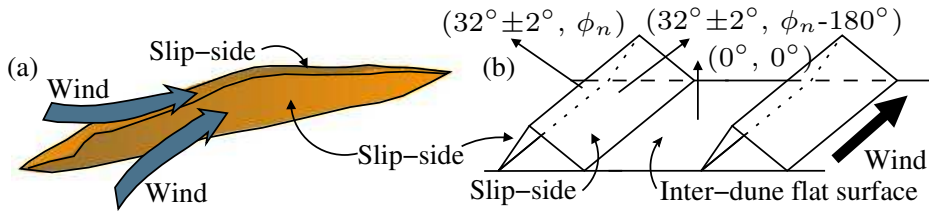


Figure 3.8: (a) Longitudinal dune and (b) its facet model.

peak corresponds to the flat rough facet $(0^\circ, 0^\circ)$ with a 50% weight. The σ° response for this tilt distribution is shown in Fig. 3.9(b) where $\sigma_s(\theta)$ is computed from NSCAT and TRMM data at $(17.5^\circ\text{N}, 15.35^\circ\text{W})$, similar to Fig. 3.3. The presence of three dominant facets shows up in the modeled σ° response in the form of peaks. This result is consistent with the observations made by NSCAT [Fig. 3.9(c)] and ESCAT [Fig. 3.9(d)] over the areas of longitudinal dune fields in the Sahara. The mesh NSCAT and ESCAT $\sigma^\circ(\theta, \phi)$ response is prepared by using the σ° vs θ observations at each ϕ sample and fitting the data with non-parametric curve similar to Fig. 3.7. The line fits for different ϕ directions are then connected at regular θ intervals to achieve the mesh plots in Figs. 3.9(c) and 3.9(d) for comparison with model simulation. The peaks at $(32^\circ, 106.5^\circ)$ and $(32^\circ, 302.5^\circ)$ in NSCAT data and at $(31^\circ, 79^\circ)$ and $(31^\circ, 281^\circ)$ in ESCAT data are the responses due to the two slip-sides of the longitudinal dunes in the footprint. Since the slip-sides have slopes nearly equal to the angle of repose, they are almost devoid of any surface ripples.

3.2.2 Transverse Dune

A typical transverse dune has two sides, a slip-side similar to longitudinal dunes and a windward-side which is opposite to the slip-side in azimuth and has a slope of 10° - 15° . Figure 3.10 shows $\sigma^\circ(\phi)$ plots for NSCAT, ESCAT and QSCAT over a transverse dune field at location 3 ($17.5^\circ\text{N}, 9.3^\circ\text{W}$). The single maximum corresponds to the single slip-side of a transverse dune. In this case, ϕ corresponding to this maximum is the mean wind direction that produces this dune field.

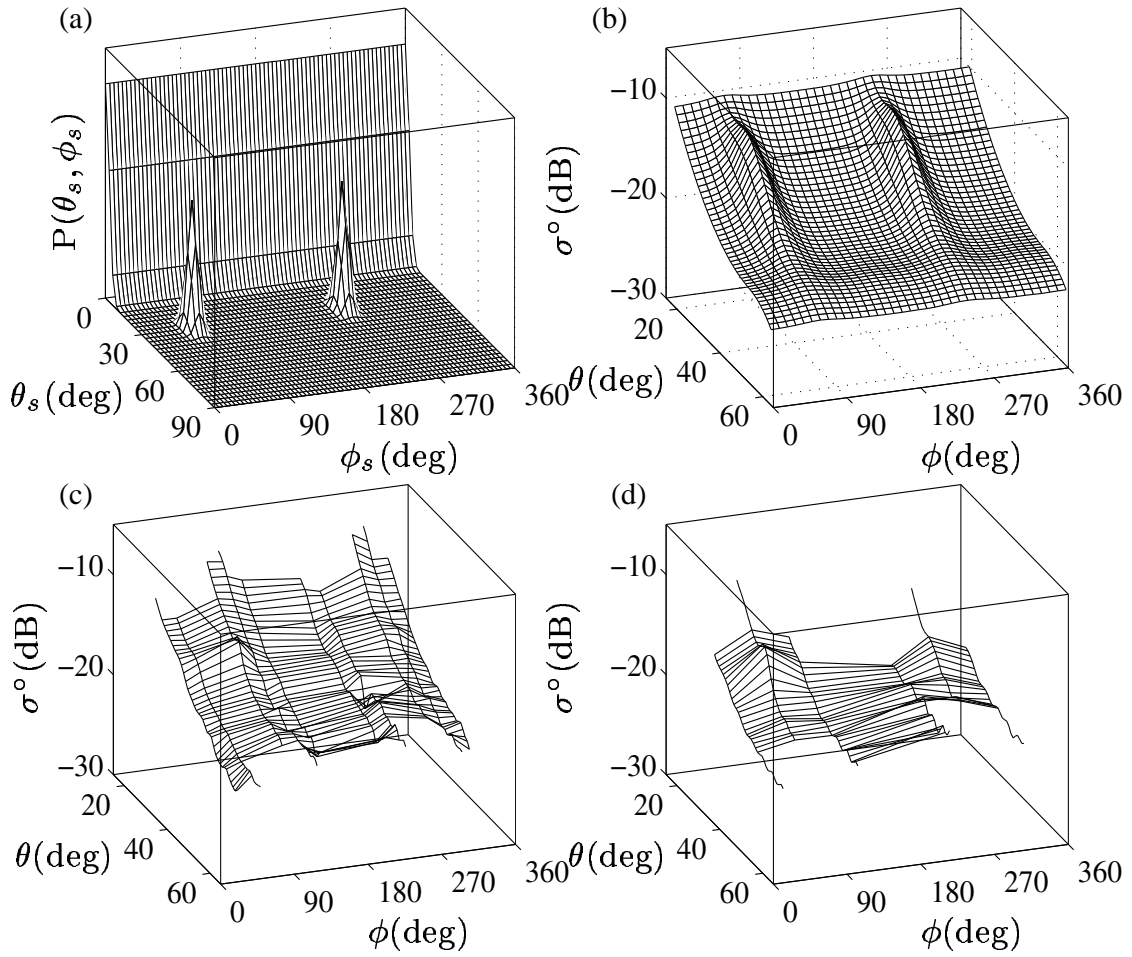


Figure 3.9: (a) Tilt distribution of a longitudinal dune with each slip-side covering 25% of footprint. The orientation of the slip-sides is $(30^\circ, 60^\circ)$ and $(30^\circ, 240^\circ)$ with $\varsigma_\theta=3^\circ$, $\varsigma_\phi=5^\circ$ and $\varsigma_{\theta\phi}=0$. Inter-dune flat area covers the remaining 50% of surface with $\varsigma_\theta=3^\circ$, $\varsigma_\phi=6^\circ$ and $\varsigma_{\theta\phi}=0$. (b) is its corresponding simulated σ^o response using $\sigma_s = -18.82 - 0.24(\theta - 40^\circ) + 0.0088(\theta - 40^\circ)^2$. Observation over actual longitudinal dune field at $(17.5^\circ\text{N}, 15.35^\circ\text{W})$ by (c) NSCAT V-pol and (d) ESCAT.

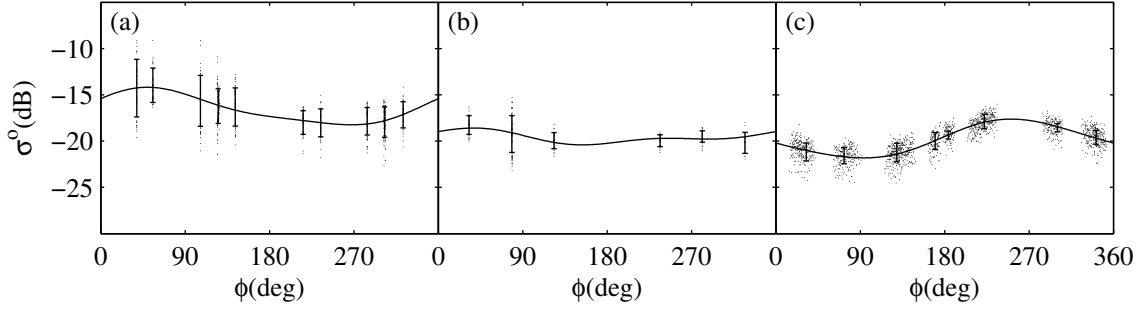


Figure 3.10: σ° azimuth angle response over a transverse dune field at (17.5°N, 9.3°W) from (a) NSCAT V-pol for θ range 30°-35°, (b) ESCAT for θ range 30°-35°, and (c) QSCAT for $\theta=55^\circ$. Solid line is a second order harmonic fit.

Figure 3.11 shows $\sigma^\circ(\theta)$ modulation over the slip- and windward-side of a transverse dune from NSCAT and ESCAT observations. The slip-side response has a rise in σ° in the incidence angle range of 30°-35° similar to the longitudinal slip-side. This observation is consistent in both Ku- and C-band data. Since the slope of the windward-side is lower than the slip-side, it results in a similar σ° rise at incidence angles of 10°-15° (not observed by scatterometers).

The $\sigma^\circ(\theta)$ and $\sigma^\circ(\phi)$ responses of the observations show that the sides of a transverse dune can be viewed as facets. The slip- and windward-sides of transverse dunes are modeled as rough surface facets with (30°-35°, ϕ_n) and (10°-15°, ϕ_n+180°) mean tilt, respectively. The dune fields are modeled as composed of many simple dunes with inter-dune areas modeled as zero tilt rough facets similar to longitudinal dune fields. The model is shown in Fig. 3.12.

The geometry of the transverse dunes suggests that the ratio of windward- and slip-side area (F_w/F_s) is in the range 2.2–2.8, and that the flat area fraction is $F_f = 1 - F_w - F_s$. Figure 3.13(a) shows the cumulative tilt distribution for the modeled transverse dune field. The two peaks at (30°, 60°) and (12°, 240°) are due to slip- and windward-side with weights of 15% and 35%, respectively. The third long peak corresponds to the flat rough facet (0°, 0°) with 50% weight. The σ° response for this tilt distribution is shown in Fig. 3.13(b) where $\sigma_s(\theta)$ is computed from NSCAT and TRMM data at location 3, similar to Fig. 3.3. The presence of three dominant facets

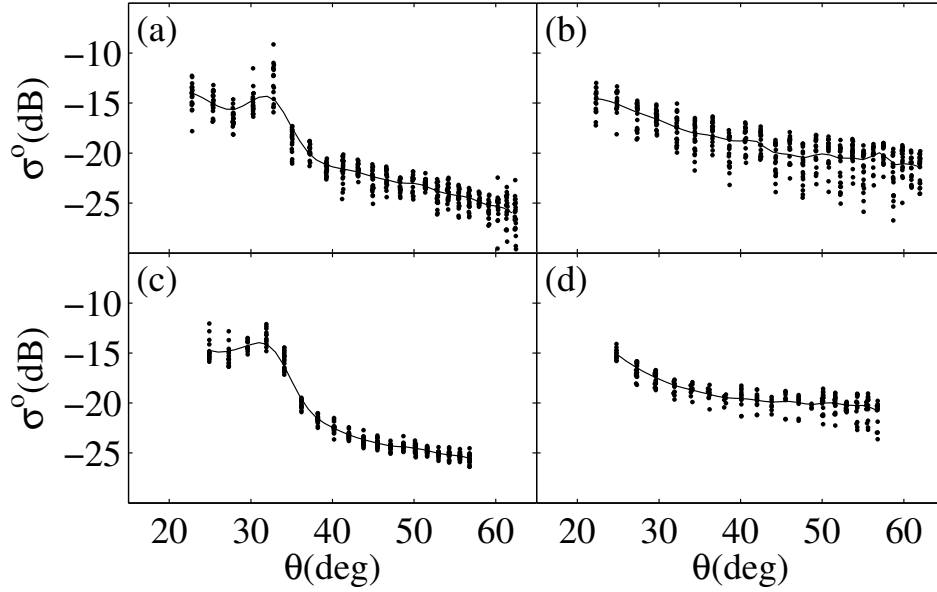


Figure 3.11: σ^0 incidence angle response over a transverse dune field at (17.5°N, 9.3°W) from NSCAT V-pol and ESCAT. (a) and (b) are NSCAT measurements at $\phi=56^\circ$ and $\phi=284^\circ$, respectively. (c) and (d) are ESCAT measurements at $\phi=33^\circ$ and at $\phi=236^\circ$, respectively.

shows up in the modeled σ^0 response in the form of peaks. This result is consistent with observations made by NSCAT [Fig. 3.13(c)] and ESCAT [Fig. 3.13(d)] over areas of transverse dune fields in the Sahara. The observations are similar to longitudinal dunes but have only one slip-side response. However, unlike longitudinal dunes, there is a peak 180° in azimuth from the slip-side at higher incidence angles. This peak is due to Bragg Scattering from the small scale ripples on the windward-side of the transverse dune.

The model simulation results for both longitudinal and transverse dune fields significantly resemble the scatterometer observations. This is further confirmed by the consistent response from the two scatterometers operating at different frequencies. The results can be extended to more complicated dunes where the number of facets increases and facet orientation is more variable. Crescent shaped barchan facets have the same tilts as transverse dunes but with higher ϕ_s variance. The high variance

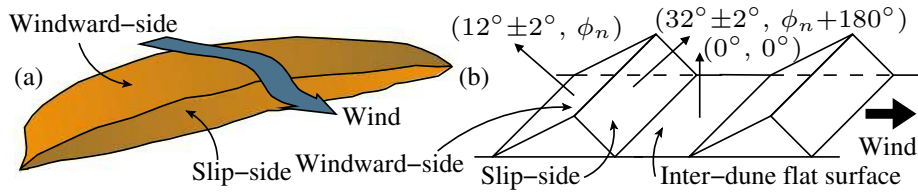


Figure 3.12: (a) Transverse dune and (b) its facet model.

reflects the directional variability of the tilted facets in the form of the curvature of barchan slip- and windward-side.

Star dunes, due to multiple limbs extending in various directions, result in increased σ° variability with the look direction. Sand sheets without dunes show negligible azimuth angle modulation and have linear incidence angle response (in dB scale). Observations show that the incidence angle response becomes more quadratic with increasing thickness of the sand layer.

3.3 Summary

Ergs represent diverse and dynamic parts of the Sahara that undergo a continuous surface reformation due to wind action. Ergs have two scales of surface features, i.e., large scale dunes and small-scale ripples. The electromagnetic scattering from erg surfaces is modeled as composed of scattering from large scale dunes and small scale ripples. The dunes are modeled as composed of tilted rough facets. The total scattering due to dunes is the sum of scattering from all of the rough facets in the footprint weighted by the fraction of their area in the footprint. Small scale ripples are modeled as cosinusoidal ripples that scatter the incident electromagnetic waves in discrete directions called Floquet modes. The backscattering from the cosinusoidal ripples occurs in the directions that have Floquet modes directed towards the sensor. The total backscattering response of surface ripples is the sum of scattering from all of the surface components.

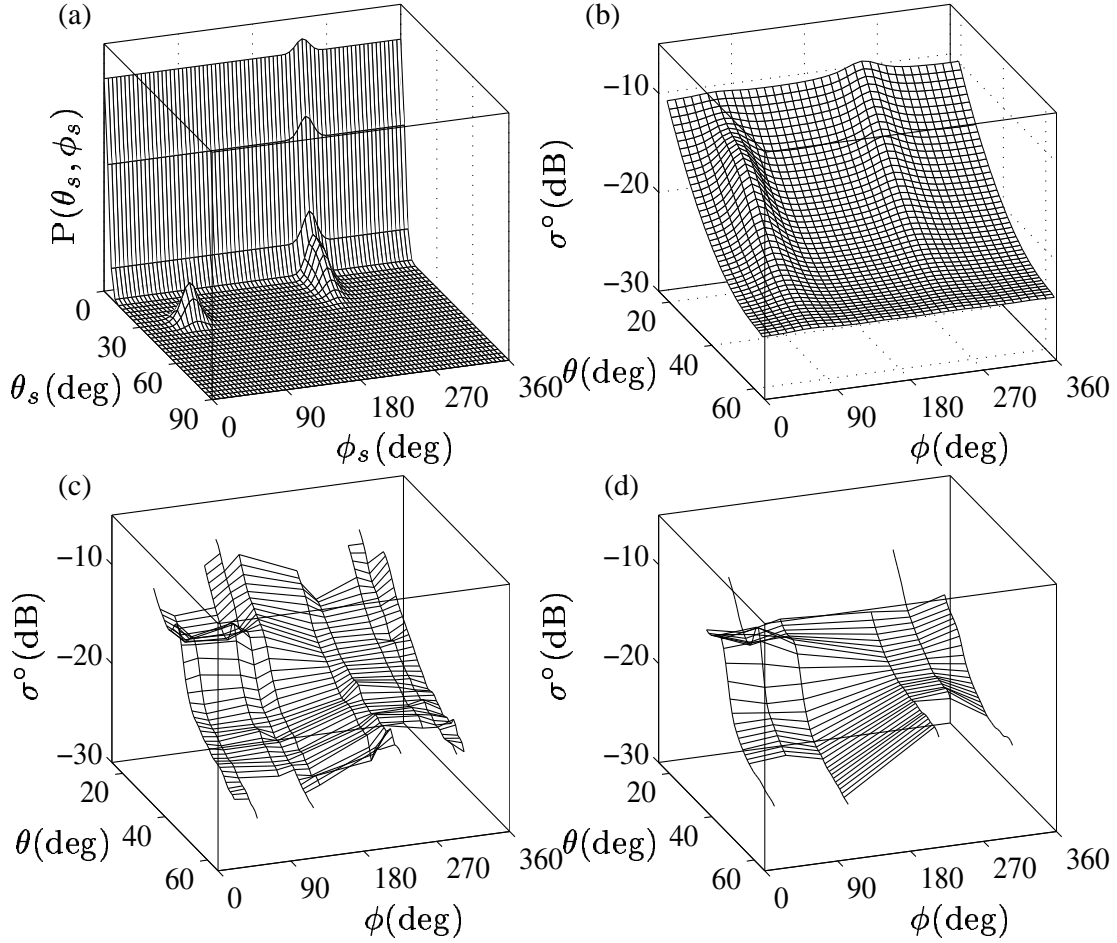


Figure 3.13: (a) Tilt distribution of a transverse dune with slip- and windward-side covering 15% and 35% of footprint, respectively. Slip-side is oriented in $(30^\circ, 60^\circ)$ direction with $\varsigma_\theta=3^\circ$, $\varsigma_\phi=10^\circ$ and $\varsigma_{\theta\phi}=0$. Windward-side is oriented in $(30^\circ, 240^\circ)$ direction with $\varsigma_\theta=8^\circ$, $\varsigma_\phi=8^\circ$ and $\varsigma_{\theta\phi}=0$. Inter-dune flat area covers the remaining 50% of surface with $\varsigma_\theta=3^\circ$, $\varsigma_\phi=8^\circ$ and $\varsigma_{\theta\phi}=0$. (b) is its corresponding simulated σ° response using $\sigma_s = -20.05 - 0.328(\theta - 40^\circ) + 0.0075(\theta - 40^\circ)^2$. Observation over actual transverse dune field at $(17.5^\circ\text{N}, 9.3^\circ\text{W})$ by (c) NSCAT V-pol and (d) ESCAT.

Longitudinal and transverse dune fields are modeled as composed of three dominant rough facets. Two of these facets correspond to the two slip-sides in the case of longitudinal dunes. For transverse dunes they correspond to windward- and slip-side. The third facet is flat and accounts for the inter-dune flat area. The proposed rough facet model is applied to the modeled dune fields. The results indicate a strong signature of the rough facets in the backscatter response. The look directions at which the peak value occurs, give the mean tilt of the facet. The simulation results are similar to NSCAT and ESCAT observations over the Saharan longitudinal and transverse dune fields.

It is found that an erg surface modulates the Ku- and C-band σ° measurements with the look direction. The incidence angle modulation reflects the presence of slip-sides on the surface in the form of a slight rise in backscatter at the incidence angles equal to the angle of repose of sand. At these incidence angles, the azimuth modulation indicates the number of slip-sides present that can be used to identify the transverse and longitudinal dunes. This can be used to determine the average wind direction in the area which is addressed in Chapter 4.

Chapter 4

Microwave Backscatter Modeling of Erg Surfaces – Dynamic

The previous chapter shows that radar backscattering from ergs exhibit coupled θ - and ϕ -modulation that depends upon the surface geometrical characteristics. In this chapter, a more comprehensive model of σ° response over sand is introduced and σ° variations due to observation geometry parameters are studied. Data and the model are used to study the spatial characteristics and temporal dynamics of the Saharan ergs. The temporal variability of both σ° spatial inhomogeneity and ϕ -modulation are used to investigate short- and long-term behavior of sand bedforms.

In Section 4.1, a model of σ° modulation as a function of observation geometry is introduced. The σ° variability due to view angle and measurement centroid displacement are addressed. In Section 4.2, model inversion results are presented to understand and relate the model parameters to the surface characteristics. The dependence of model parameters on θ over different sand surfaces is presented. The spatial and temporal behaviors of model parameters in comparison to ECMWF winds are also given. The material is currently in review for publication in *IEEE Transactions on Geoscience and Remote Sensing*.

4.1 Observation geometry induced σ° modulation

The backscattering over erg surfaces measured by spaceborne scatterometers depends upon the wind-dependent sand surface geometrical characteristics and instrument observation geometry parameters. The observation geometry parameters are incidence angle, azimuth angle (sensor-target view angles) and antenna foot print

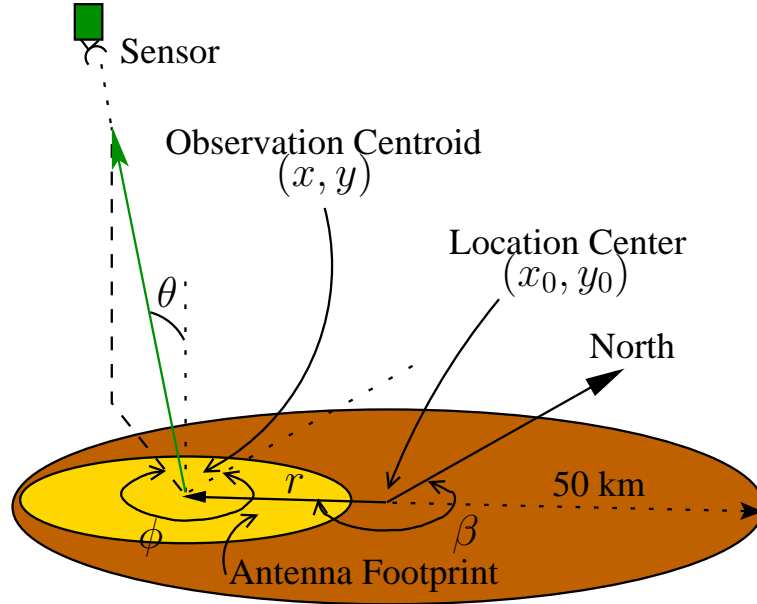


Figure 4.1: σ° observation geometry parameters for a single resolution element with in a circular area with a radius of 50 km centered at (x_0, y_0) .

centroid (x, y) (target location) (see Fig. 4.1). σ° is modulated with the displacement of observation centroid from the study center point (x_0, y_0) , herein termed as “centroid displacement variability”. I define (r, β) as the observation displacement from (x_0, y_0) where r is the distance (in kilometers) of the observation centroid and β is the bearing angle from (x_0, y_0) as shown in Fig. 4.1.

NSCAT σ° measurements for which the centroid of the measurement footprint is within 50 km of each of the selected locations are used. In case of ESCAT and QSCAT, 100 km and 10 km radii are used, respectively.

The erg surface geometry varies with time and has a complex dependence on the variability of prevailing winds. Thus, σ° measurements are also a function of observation time. σ° variability induced by the temporal variations in the sand bedform is reduced by using data from a narrow time window. I use σ° measurements from a 30 day temporal window, effectively assuming that surface characteristics do

not change significantly during this time. The effectiveness of this time window diminishes in the areas of highly variable winds. The selected spatial radii for each instrument and temporal window size provide sufficient measurement samples to estimate the model parameters. The model parameters are computed every 15 days with overlapping windows to study seasonal effects.

Over sand surfaces, the σ° measurements (in dB) as a function of observation geometry are modeled as

$$\sigma^\circ(\theta, \phi, r, \beta) = A_\theta + q_\theta(\phi) + h_\theta(r, \beta) \quad (4.1)$$

where $\sigma^\circ(\theta, \phi, r, \beta)$ is the scatterometer measurement with view angles (θ, ϕ) the centroid of its measurement footprint at (r, β) from (x_0, y_0) . The dependence of the model terms on incidence angle is represented by the subscript θ . A_θ is the mean response of the surface which depends upon θ . $q_\theta(\phi)$ and $h_\theta(r, \beta)$ are the observation-azimuth-angle-modulation and observation-centroid-displacement-variability, respectively, as a function of θ . In this model, the time dependence is neglected by selecting a narrow time window.

In previous chapter, σ° θ dependence has been modeled with a quadratic dependence. The quadratic model adequately models θ dependence over erg sand sheets, which are approximately a single facet. The response over tilted sand sheets is similar, but shifted in θ depending upon the θ' . Dune fields are composed of multiple tilted facets and result in a complicated σ° incidence angle dependence as revealed in Fig. 4.2 during Julian Days (JD) 1-31, 1997. As noted in the Chapter 3, in such areas, σ° response at a given θ is sum of responses from individual facets as a function of θ' and weighted by the facets area projected in the direction of the sensor. Note that the σ° variation with θ is different for different dunes. Thus, model parameters are computed separately for different θ bins. The model in Eq. 4.1 states that for a given θ , the observed σ° is given by the sum of mean surface response, a ϕ -modulation, and variability due to measurement centroid. In the next two subsections, the observation ϕ -modulation and centroid displacement variability are discussed.

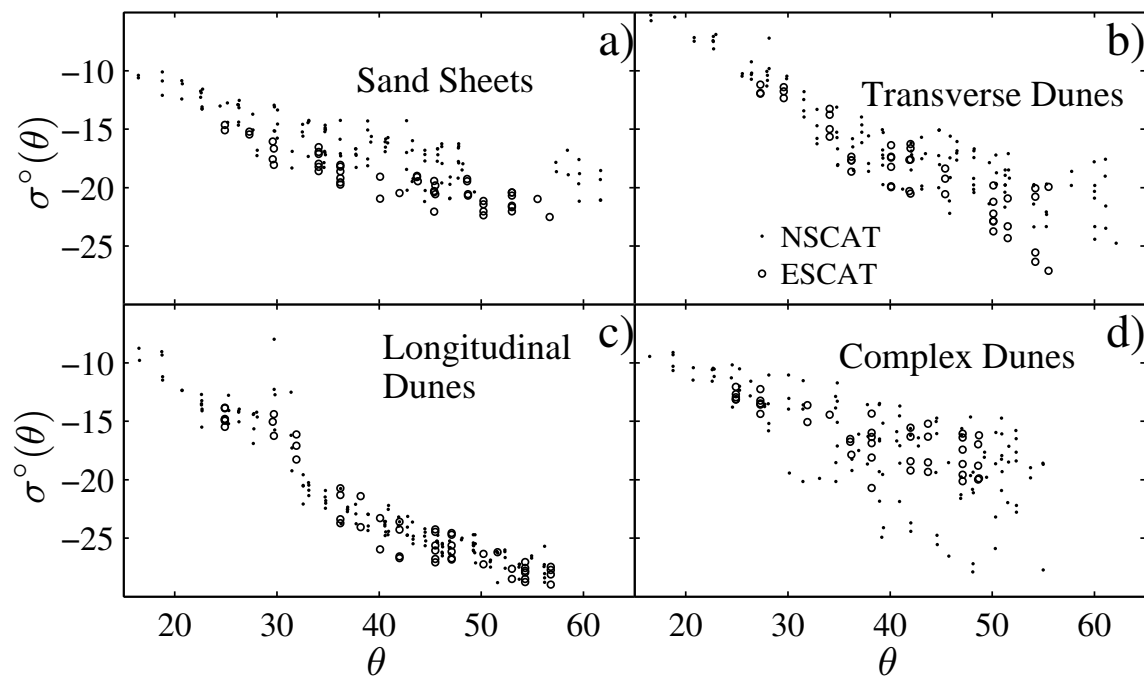


Figure 4.2: NSCAT and ESCAT $\sigma^\circ(\theta)$ at $\phi = 127^\circ$ during JD 1-31, 1997 for a) sand sheets, b) transverse dunes, c) longitudinal dunes and d) complex dunes corresponding to locations 16, 5, 10 and 18, respectively.

4.1.1 σ° Azimuth Angle Modulation

NSCAT and ESCAT provide σ° measurements at multiple θ and ϕ angles. σ° from a flat sand surface is maximum at near-nadir, whereas a tilted surface with slope θ_s and orientation ϕ_s has maximum backscatter when $\theta = \theta_s$ and $\phi = \phi_s$. Thus, the presence of large-scale slip-sides results in a strong σ° ϕ -modulation return at $\theta = 30^\circ$ – 35° . The azimuth angle at which the maximum of the ϕ -modulation occurs is equal to the orientation of the slip-side, which is related to the dominant wind direction (Chapter 3).

NSCAT and ESCAT measure V-pol σ° at ten and six azimuth angles, respectively. QSCAT V-pol σ° measurements have relatively higher azimuth sampling, but only at one incidence angle (54°). Previous studies use a second order harmonic

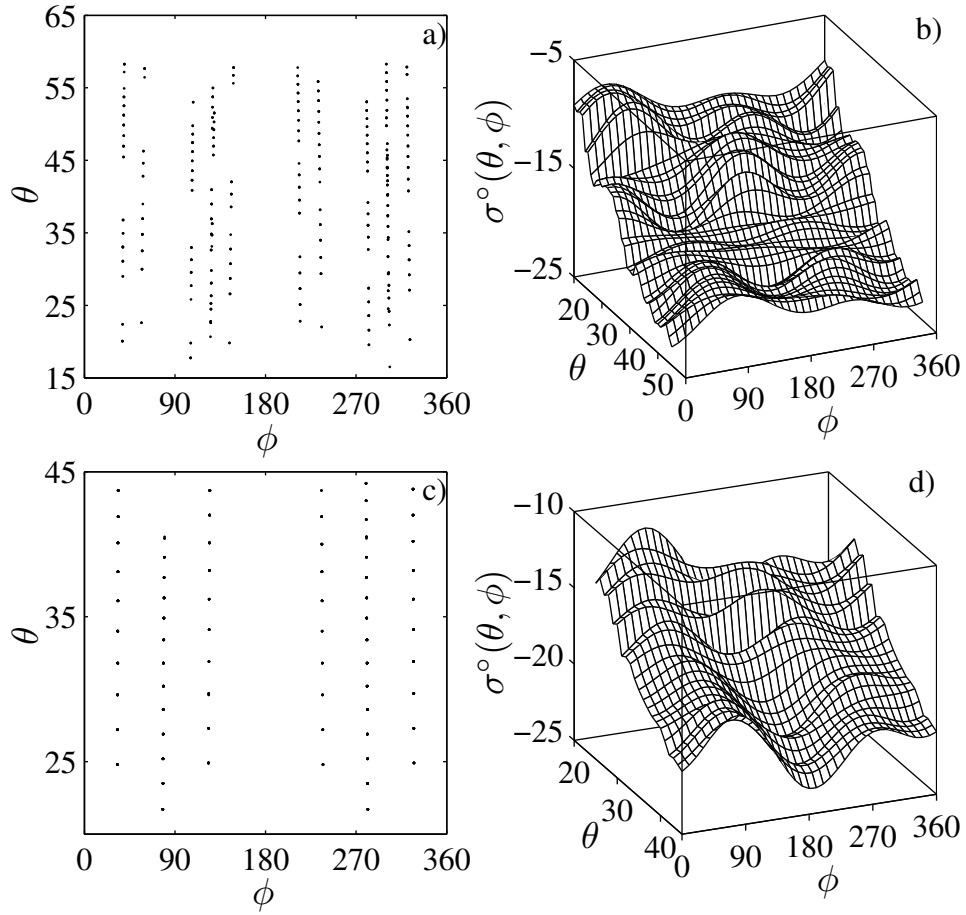


Figure 4.3: a) and c) Plots of θ and ϕ for each measurement during JD 1-30, 1997 at location 18 from NSCAT and ESCAT, respectively. b) and d) $\sigma^\circ(\theta, \phi)$ model surface fits as a function of θ and ϕ from NSCAT and ESCAT, respectively. The RMS errors of model fits for NSCAT and ESCAT are 3.63 and 2.97 dB, respectively.

model to represent the σ° ϕ -modulation without accounting for incidence angle dependence, i.e.,

$$q(\phi) = M_1 \cos(\phi - \phi_1) + M_2 \cos(2\phi - \phi_2) \quad (4.2)$$

where M_i and ϕ_i are the magnitude and the phase of i th order harmonic. Over dune surfaces, M_i and ϕ_i are a function of θ . Due to a complicated dependence on the incidence angle, the second order harmonic model is used separately for each θ given by

$$q_\theta(\phi) = M_{\theta 1} \cos(\phi - \phi_{\theta 1}) + M_{\theta 2} \cos[2(\phi - \phi_{\theta 2})] \quad (4.3)$$

where M_{θ_i} and ϕ_{θ_i} are the magnitude and phase, respectively, of the i th harmonic computed for incidence angle θ . The quality of this model fit depends upon the θ and ϕ sampling density of σ° measurements. Figs. 4.3(a) and (c) show the σ° measurement θ and ϕ sampling of NSCAT and ESCAT, respectively, over location 18 with complex dunes. In order to estimate the model parameters at a given θ , σ° measurements with incidence angles within $\theta \pm 3.5^\circ$ and a 7° wide Gaussian weighting kernel centered at the given θ are used to perform a weighted least squares fit.

Figures 4.3(b) and (d) show the $\sigma^\circ(\theta, \phi) = A_\theta + q_\theta(\phi)$ model fits to NSCAT and ESCAT data, respectively. Tables 4.1 and 4.2 list the RMS errors of the model applied to NSCAT and ESCAT data over each of the study locations. RMS errors of other models are discussed in the following sections. The incidence angle dependent model $q_\theta(\phi)$ has lower RMS error than $q(\phi)$ (where θ is not considered) and its surface fit provides a comprehensive view of the σ° dependence on the view angles. The reduction in RMS error is similar at all locations. The locations with high RMS error have high surface inhomogeneity not accounted for in these two models. Although the ϕ -modulation is adequately modeled, there exists data variance due to the centroid displacement variability discussed in the next subsection.

Figure 4.3 reveals that the model parameters change significantly with incidence angle. The difference in the ϕ -modulation at lower and higher incidence angles depends upon the sand surface geometry. The wind-induced changes in large- and small-scale surface geometry add, remove, and/or shift peaks in the ϕ -modulation. Generally, short-term changes in the winds are reflected by the changes in the small-scale surface ripples, which are periodic in the wind direction. This alignment of surface ripples to the wind becomes complicated over tilted facets of existing large-scale dunes. Orographic wind flow over the tilted dune facets may deviate from the average prevailing wind. Thus, the orientation of small-scale ripples on a facet may not align exactly with the average wind direction. Since the simple model presented in this paper relies on the σ° dependence on surface geometry to infer average winds, its accuracy reduces over the areas with complex sand bedforms.

Table 4.1: RMS errors for different model versions applied to NSCAT data at 19 locations during JD 1-30, 1997.

Site #	$q(\phi)$	$q_\theta(\phi)$	$h(r, \beta)$	$h_\theta(r, \beta)$	$q_\theta(\phi) + h_\theta(r, \beta)$
1	2.25	0.97	2.19	0.69	0.68
2	4.48	2.16	4.46	1.74	1.48
3	3.69	1.09	3.70	1.37	0.95
4	5.20	2.21	5.20	2.52	1.54
5	4.80	1.64	5.21	1.82	1.47
6	3.55	2.27	3.03	1.40	1.33
7	6.07	1.95	6.25	1.94	1.65
8	2.61	1.49	2.33	0.64	0.63
9	2.93	1.92	2.57	1.17	1.14
10	5.69	1.25	5.80	1.44	1.17
11	3.38	1.04	3.37	0.77	0.74
12	5.54	3.99	4.61	1.98	1.81
13	3.59	1.79	3.36	1.08	1.08
14	3.17	1.08	3.18	0.80	0.77
15	3.45	1.87	3.40	1.77	1.24
16	3.18	2.16	2.84	1.61	1.39
17	2.48	0.87	2.44	0.65	0.63
18	5.09	3.63	4.21	1.75	1.58
19	4.74	1.34	5.20	1.86	1.27

4.1.2 σ° Centroid Displacement Variability

σ° varies with the centroid displacement due to the surface spatial variability. This variability reflects the inhomogeneity of the underlying surface, which in the case of the ergs is caused by varying dune shapes, dune density, sand depth and large-scale slope. Compound dune fields and mixed dune fields have varying dune shapes and spatial densities. The varying sand depth also introduces variations in the θ dependence of displacement variability. The varying large-scale slope from the middle to the fringes of the erg basins appear to play a significant role in the centroid displacement variability. At the fringes of the ergs the surface topography transitions from a sandy to a rocky surface and results in maximum σ° spatial inhomogeneity.

Analysis of σ° observations over various locations suggests that the σ° centroid displacement variability [$h(r, \beta)$] is best modeled by a variable coefficient

Table 4.2: RMS errors for different model versions applied to ESCAT data at 19 locations during JD 1-30, 1997.

Site #	$q(\phi)$	$q_\theta(\phi)$	$h(r, \beta)$	$h_\theta(r, \beta)$	$q_\theta(\phi) + h_\theta(r, \beta)$
1	1.41	0.74	1.39	0.54	0.55
2	4.60	1.89	4.70	2.26	1.47
3	3.42	1.11	3.49	1.48	1.00
4	4.26	2.52	4.21	2.49	1.86
5	5.32	1.80	5.33	1.97	1.61
6	2.72	1.59	2.20	1.03	0.90
7	3.95	2.37	3.77	1.70	1.47
8	1.88	1.47	1.37	0.48	0.48
9	2.86	2.42	2.07	1.01	0.90
10	4.23	1.22	4.44	1.30	1.04
11	2.28	1.34	2.02	0.68	0.64
12	3.56	2.42	3.15	1.24	1.07
13	2.97	1.84	2.57	0.93	0.86
14	3.60	1.95	3.49	1.04	0.98
15	3.37	1.79	3.62	1.82	1.32
16	2.86	2.25	2.27	0.85	0.79
17	1.41	0.86	1.23	0.58	0.54
18	4.01	2.97	3.65	1.63	1.41
19	3.95	1.64	3.85	1.38	1.01

second order harmonic equation given by

$$h(r, \beta) = H_1 r \cos(\beta - \beta_1) + H_2 r^2 \cos[2(\beta - \beta_2)] \quad (4.4)$$

where the first term on the right side is a plane with the steepest ascent of H_1 (dB/km) in the direction β_1 and the second term is a hyperbolic paraboloid with the highest curvature H_2 (dB/km²) in the direction β_2 . H_1 and H_2 represent the magnitudes of a plane and a hyperbolic paraboloid, linearly combined and added to the mean response.

Figure 4.4(a) shows the $\sigma^\circ(r, \beta) = A + h(r, \beta)$ model fit (A is the mean σ° with no θ dependence) to NSCAT σ° measurements with an RMS error of 4.21 dB. Two slices through the fit at $r = 15$ km and $r = 30$ km are shown in Fig. 4.4(b). Their comparison to the σ° measurements within 3 km of these radii shows that $h(r, \beta)$ does not represent the behavior of all data measurements. By taking into

account the strong dependence of σ° on θ , the model fit is improved by computing the model parameters separately for different incidence angles using

$$h_\theta(r, \beta) = H_{\theta 1} r \cos(\beta - \beta_{\theta 1}) + H_{\theta 2} r^2 \cos[2(\beta - \beta_{\theta 2})] \quad (4.5)$$

where the subscript θ of model parameters represents their θ dependence. Figures 4.4(c) and (e) are the model fit of $\sigma^\circ(\theta, r, \beta) = A_\theta + h_\theta(r, \beta)$ for θ ranges 25° – 35° and 40° – 50° . Comparison reveals the strong incidence angle dependence of the σ° spatial inhomogeneity. Table 4.1 5th and 6th columns present the RMS errors of $h(r, \beta)$ and $h_\theta(r, \beta)$ model fits to the NSCAT σ° measurements over the selected locations. The incident angle dependent model significantly reduces the RMS error over complex bedforms. The RMS errors of fits to ESCAT data show similar behavior (Table 4.2). These results confirm that θ -dependent σ° spatial inhomogeneity is significant over the complex erg bedforms.

4.2 σ° Full Observation Model Results

σ° azimuth angle modulation and spatial inhomogeneity depend upon θ . In the following analysis, the full observation geometry model in Eq. 4.1 is used with the incidence angle dependent azimuth angle modulation and centroid displacement variability models given in the last two subsections. This model is applied to the NSCAT and ESCAT data used in Fig. 4.3. The model fit results are shown in Fig. 4.5. The full model shows a significant improvement in the fit by removing the σ° spatial inhomogeneity. This improvement is consistent in all scatterometers, but is most obvious in the NSCAT data at $\theta = 37^\circ$. The surface fits achieved with the full observation model reduce the RMS error for NSCAT and ESCAT to 1.58 and 1.41 dB, from 3.63 and 2.97 dB when spatial dependence is ignored [see Tables 4.1 and 4.2]. The corresponding QSCAT data, only available at $\theta = 54^\circ$, results in RMS errors of 0.6 and 1.57 dB, with and without considering spatial inhomogeneity.

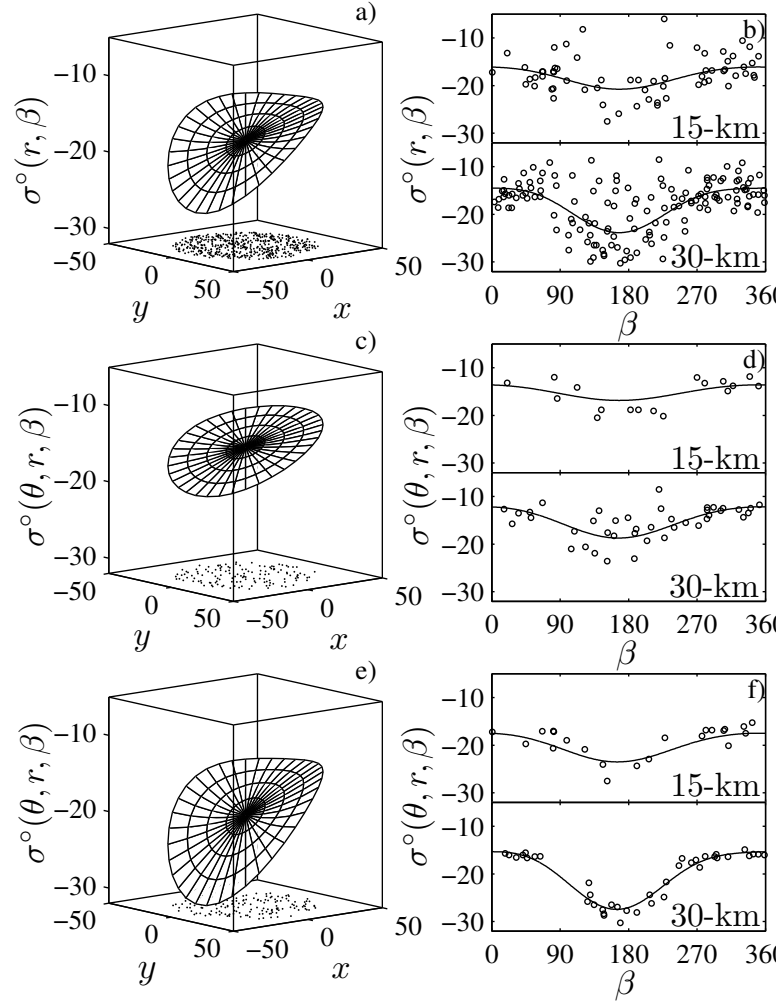


Figure 4.4: a) $\sigma^\circ(r, \beta)$ model fit to NSCAT σ° measurements during JD 1-30, 1997 at location 18. The centroid locations of measurements within 50 km of location 18 are shown at the bottom of the box to indicate the density of spatial samples used in the model fit. b) Two slices through the spatial model fit at 15 and 30 km from the center. Raw σ° measurements within 3 km from each radius are also shown to analyze the quality of model fit. c)-f) Similar plots for measurements with incidence angle ranges $25^\circ-35^\circ$ and $40^\circ-50^\circ$. The RMS error of model fits in a), c) and e) is 4.21, 2.45 and 1.87 dB, respectively.

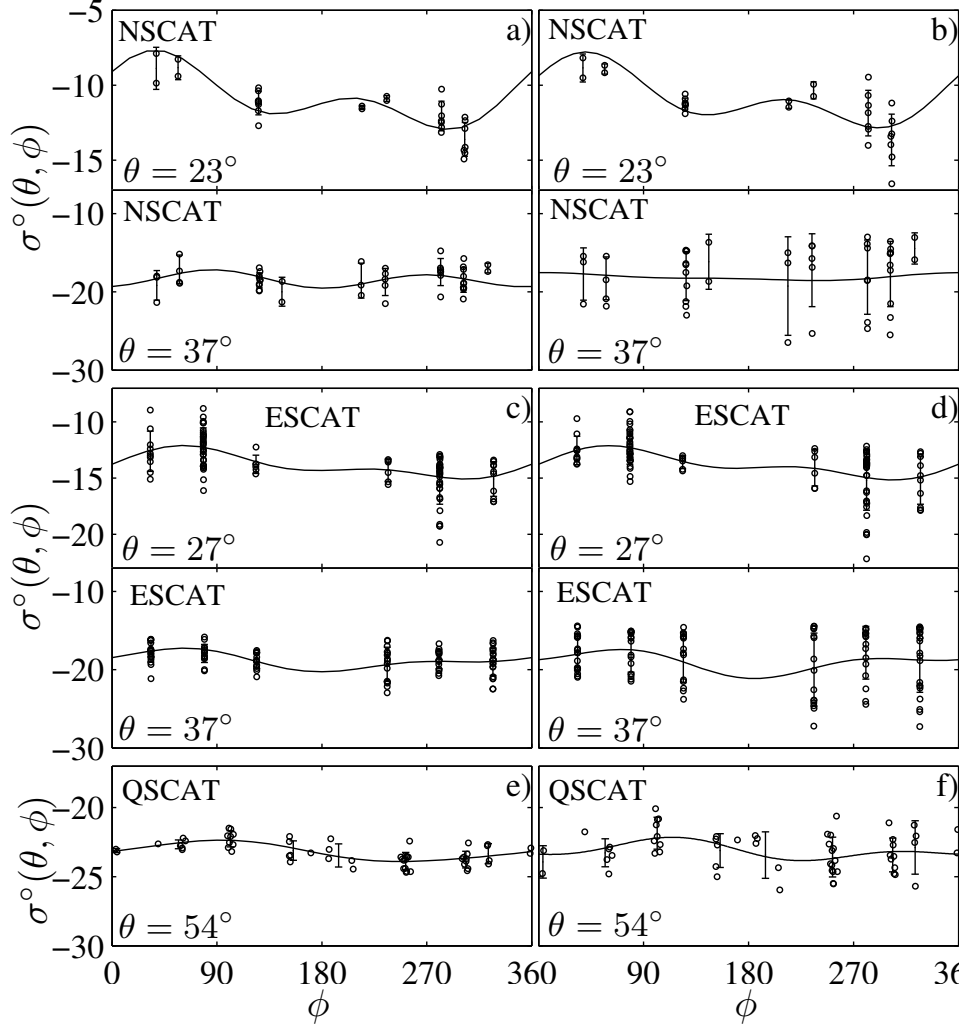


Figure 4.5: Model fits with (left) and without (right) considering σ° spatial inhomogeneity at location 18. Solid lines are the ϕ -modulation at selected incidence angles. In the left plots, the raw σ° measurements within 2° of selected θ are shown whereas the right plots show the raw measurements after subtracting the σ° spatial inhomogeneity term $h_\theta(r, \beta)$. a) c) and e) are the results from NSCAT, ESCAT and QSCAT data, respectively, using the model with spatial inhomogeneity term. b), d) and f) are the corresponding results from the model without spatial inhomogeneity term.

Tables 4.1 and 4.2 list the full observation model RMS errors over all selected locations for NSCAT and ESCAT. The full observation model reduces the RMS fit error by more than 2 dB at locations 12 and 18 which are highly inhomogeneous bedforms. In relatively homogeneous locations such as 1, 3, 5, 10 and 17, RMS error reduction is less than 0.5 dB, confirming the spatial inhomogeneity.

4.2.1 Incidence Angle Dependence of Model Parameters

The incidence angle dependence of the model results in model parameters that are a function of incidence angle. The θ dependence of model parameters depends upon the nature of the surface geometry. Figure 4.6 shows the plots of model parameters as a function of incidence angle for sand sheet, transverse dunes, longitudinal dunes and complex dunes.

Sand sheets are generally flat erg surfaces with a general slope and small-scale ripples. This results in a less complicated incidence angle dependence of σ° compared to dunes. In such areas σ° mainly depends upon the sand depth (i.e., relative surface and volume scattering at different incidence angles). Over sand sheets, a coupled contribution from varying general slope and small-scale geometry results in σ° spatial variation. The first order σ° spatial inhomogeneity (plane) has little dependence on the incidence angle and is directed at 310° with a magnitude of less than 0.1 dB/km. This spatial inhomogeneity is due to the varying general slope of the sand sheet. The second order σ° spatial inhomogeneity (hyperbolic paraboloid) is less than 0.001 dB/km² and has a direction almost equal to $\beta_{\theta 1}$. I conjecture that the second order inhomogeneity is primarily caused by spatially varying small-scale geometry. The θ dependence of the magnitude of second order inhomogeneity results from variations in the illumination of the small-scale ripples at different incidence angles. The first and second order harmonics of the azimuth angle modulation over sand sheets are caused by the general slope of the surface and small-scale geometry, respectively.

Transverse dunes have a slip-side and a windward-side. The windward-side has a slope of 10° – 15° . Longitudinal dunes have two facets that are both slip-sides. A_θ

difference between low and high incidence angles over such dune types is higher than sand sheets due to the presence of more than one dominant facet. These facets result in increased σ° at certain θ and ϕ angles which are related to the slope and orientation of constituting facets. In comparison to sand sheets, transverse and longitudinal dune fields exhibit greater θ dependence of the magnitudes and phases of the two harmonics. The first order σ° spatial inhomogeneity magnitude is about half that of sand sheets whereas the second order inhomogeneity has magnitude comparable to sand sheets. The directions $\beta_{\theta 1}$ and $\beta_{\theta 2}$ have greater variability with θ . σ° spatial inhomogeneity over these dune fields is primarily introduced by spatially varying slopes, orientations and densities of the dune facets. Spatial variations in the directions of dune axes, merging of dunes, splitting of dunes. and spatial transitions between different types of dune fields also contribute to this inhomogeneity.

Complex dunes have significant spatial variability that results in high σ° spatial inhomogeneity. The magnitudes of the σ° spatial inhomogeneity increase with θ and almost double at the far range incidence angles whereas the directions have little dependence on θ .

σ° θ -dependent ϕ -modulation $q_\theta(\phi)$ and spatial inhomogeneity $h_\theta(r, \beta)$ are computed for locations 5 and 16 and shown in Fig. 4.7. $h_\theta(r, \beta)$ is shown for $\theta = 33^\circ$. The sand sheet $q_\theta(\phi)$ plot has two peaks at 100° and 270° for all incidence angles, indicating a single facet surface. The shape of $h_\theta(r, \beta)$ indicates the extent and direction of σ° spatial inhomogeneity caused by varying slopes and small scale geometry. Other sand surfaces' $q_\theta(\phi)$ modulation significantly changes with the incidence angle. Complex dune $q_\theta(\phi)$ has various peaks caused by the dominant facets of these dunes.

The second order harmonic modulation results in 1–2 maxima depending upon the magnitudes and phases of the two harmonics (see Appendix A.4). ψ is defined to be the azimuth angle at which the peak occurs and m as the magnitude of modulation at this angle [see Fig. 4.8(a)]. Over the erg regions, the two peaks at ψ_1 and ψ_2 are generally separated by 180° . Figure 4.8(b) shows the histogram of their difference at $\theta = 33^\circ$ with the mean value of 188° .

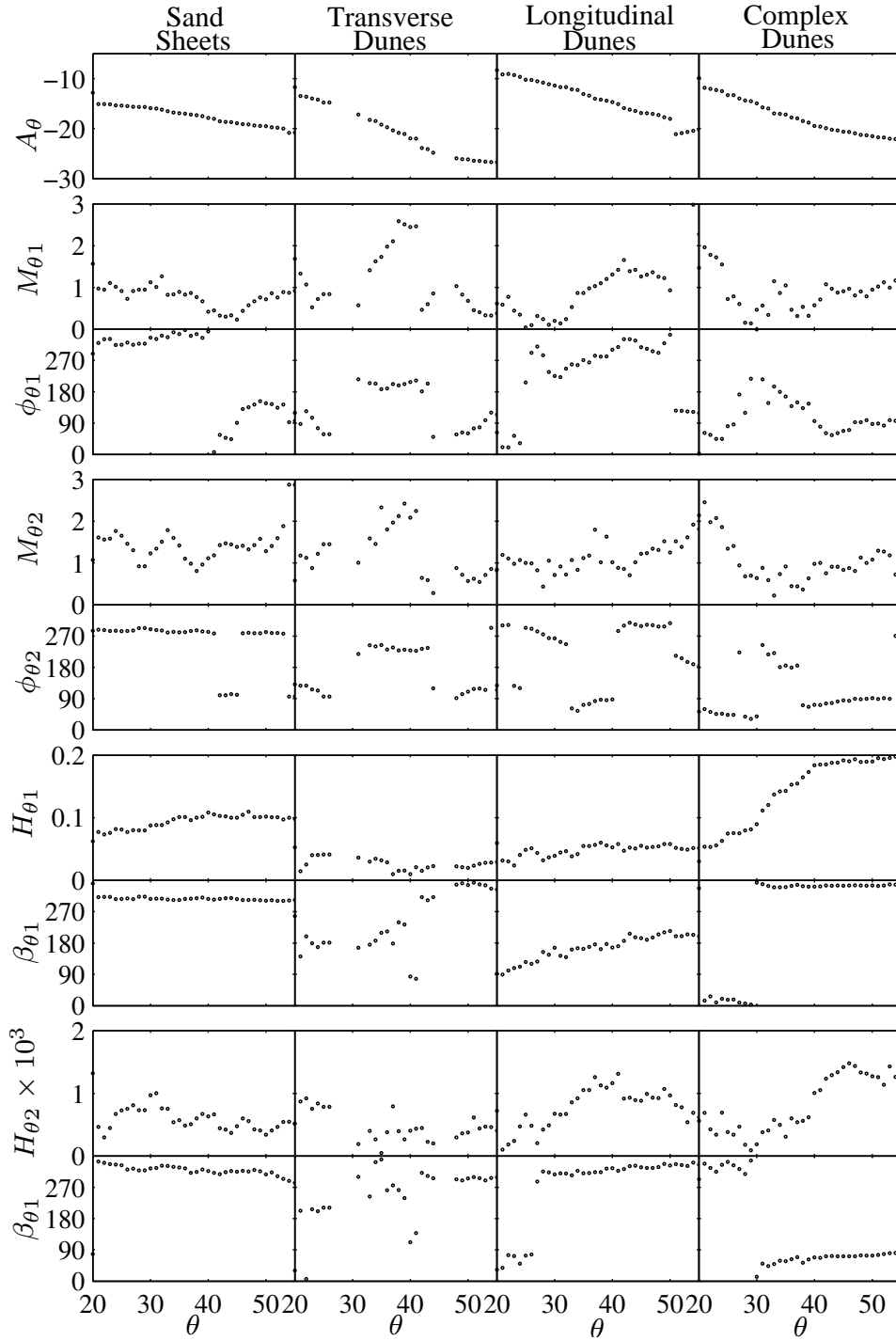


Figure 4.6: Plots illustrating the incidence angle dependence of the model parameters for sand sheets (1st column), transverse dunes (2nd column), longitudinal dunes (3rd column) and complex dunes (4th column) at locations 16, 5, 10 and 18, respectively. The nine rows of the plot array correspond to the model parameters A_θ , $M_{\theta 1}$, $\phi_{\theta 1}$, $M_{\theta 2}$, $\phi_{\theta 2}$, $H_{\theta 1}$, $\beta_{\theta 1}$, $H_{\theta 2}$, and $\beta_{\theta 2}$.

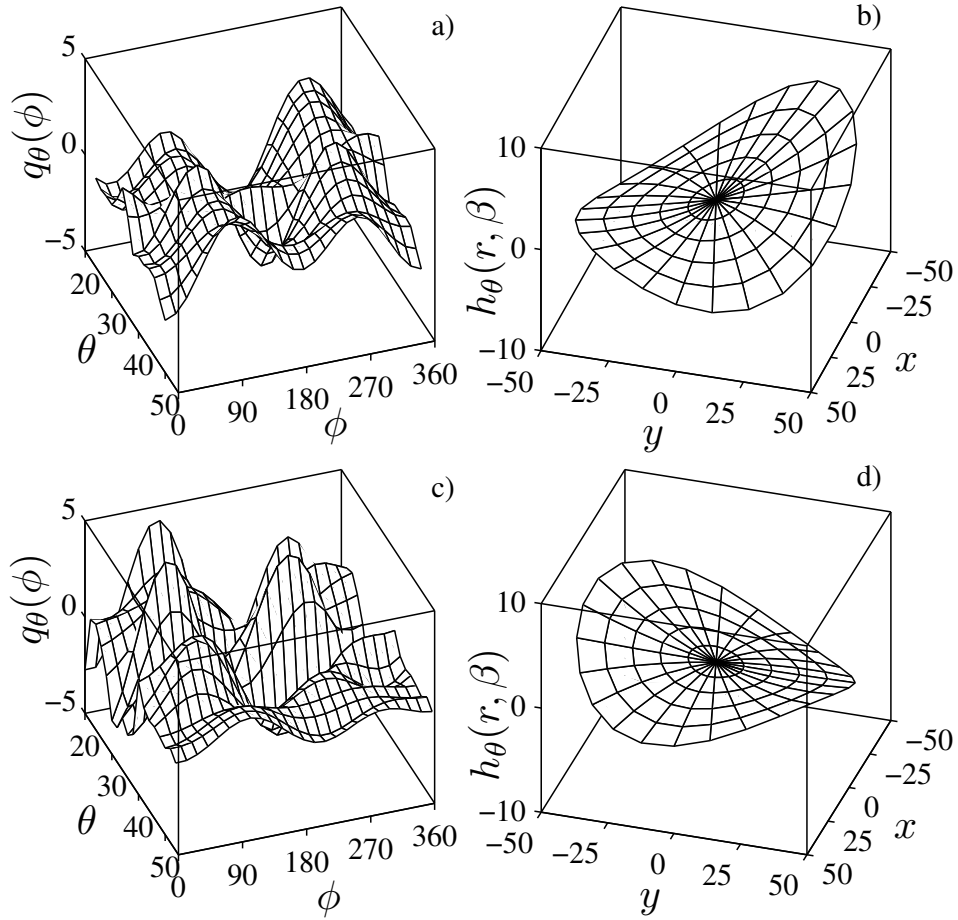


Figure 4.7: Plots of $q_\theta(\phi)$ (a, c) and $h_\theta(r, \beta)$ at $\theta = 33^\circ$ (b, d) computed using the full model for sand sheets (a, b) and transverse dunes (c, d).

The azimuth angle and magnitude of the maxima of ϕ -modulation depend upon the incidence angle. Figure 4.9 shows the plots of ψ and m as a function of θ for the four sand surface types. There is no dominant peak over the sand sheets. Transverse and longitudinal fields have one and two peaks between 30° and 35° incidence angles, respectively indicating one and two slip-sides of these dunes, respectively. The complex dunes show more complicated behavior. The azimuth angles of peaks of the σ° ϕ -modulation at 33° incidence angle are aligned to the average surface wind direction in the area. This method is used to find slip-side orientations from NSCAT and ESCAT data over all the selected locations (Table 2.1) and are listed in

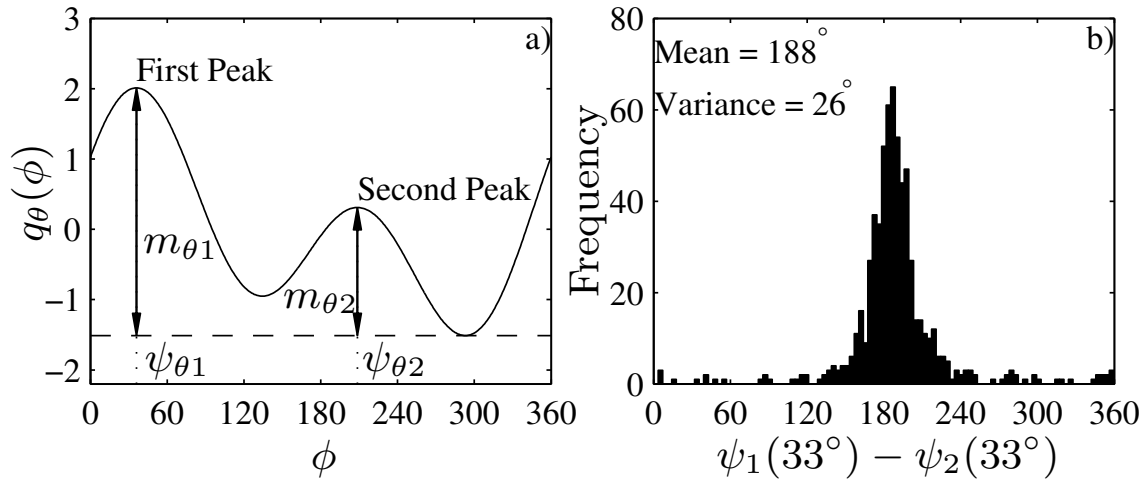


Figure 4.8: a) A slice through $q_\theta(\phi)$ surface fit is shown to define azimuth angle of a peak (ψ) and magnitude (m) of ϕ -modulation at ψ . b) Histogram of angular difference between two peaks over all the ergs showing that in general, two peaks of ϕ -modulation are separated by 180°.

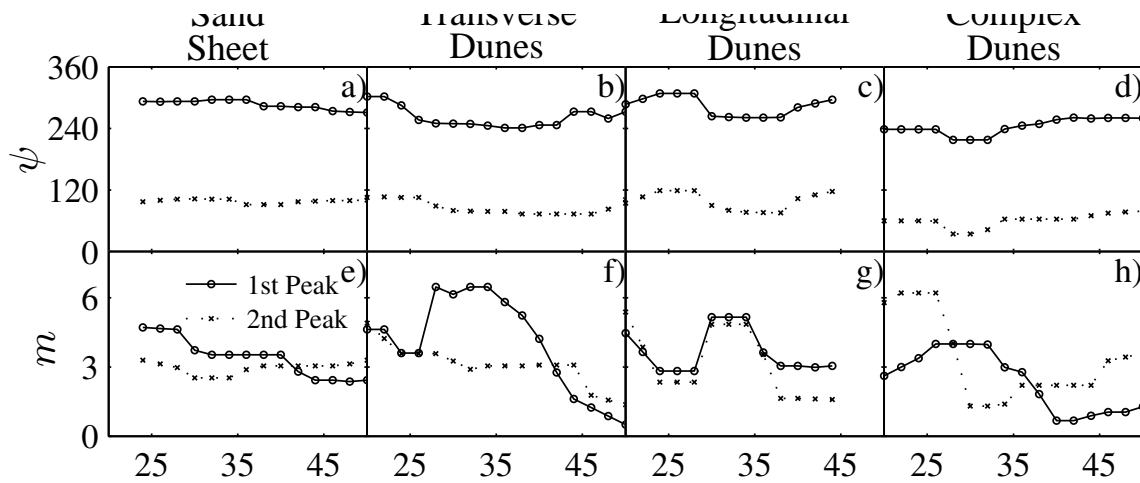


Figure 4.9: a)-d) ψ as a function of θ showing both ψ_1 and ψ_2 over the four sand surface types at locations 16, 5, 10 and 18. e)-h) Similar plots of m as a function of θ showing both m_1 and m_2 .

Table 4.3: Table listing the surface types and ECMWF wind modes over the selected study sites. Narrow and wide wind modes are symbolized by ‘NR’ and ‘WD’, respectively. The orientations of slip-sides estimated from the two scatterometers are also given.

#	ECMWF Winds Modes	$q_{\theta}(\phi)$ Peaks at $\theta = 33^{\circ}$	
		NSCAT	ESCAT
1	255° NR	289°	250°
2	255° NR	271°	278°
3	255° NR	258°	164°
4	274° WD	104°	113°
5	228° NR	297°	291°
6	255° WD, 45° WD	213° & 44°	240° & 71°
7	Multi-modal	290° & 115°	254° & 107°
8	255° NR	266°	285°
9	265° WD, 36° WD	228° & 37°	216° & 56°
10	Multi-modal	192° & 25°	286° & 108°
11	254° NR	262°	274°
12	255° WD, 35° WD	227° & 340°	201° & 48°
13	255° WD, 35° WD	268° & 71°	263° & 77°
14	235° WD, 35° WD	351° & 173°	266° & 77°
15	255° NR	259°	265°
16	35° WD	118°	89°
17	45° WD 244° WD	28° & 222°	71° & 270°
18	255° WD, 24° WD	189° & 2°	250° & 54°
19	235° NR	354°	300°

Table 4.3. Table 4.3 also lists the wind modes estimated from ECMWF predicted winds during JD 256, 1996 and JD 256, 1997. The estimated slip-side orientations reasonably match the ECMWF wind modes over the areas of simple dune bedforms. The estimates have higher deviation from ECMWF wind modes over the areas of compound and complex dunes. These results confirm that $q_{\theta}(\phi)$ at $\theta = 33^{\circ}$ has a peak ψ approximately equal to the mean wind direction. In the next section the spatial maps of the model parameters are analyzed and compare the results to the ECMWF winds.

4.2.2 Spatial Behavior of Model Parameters

In this section, the spatial behavior of the model parameters is considered. Since the presence of slip-sides is manifested in the ϕ -modulation at incidence angle range 30° – 35° , the spatial maps are shown at $\theta = 33^\circ$.

Figure 4.10 shows the spatial maps of parameters estimated from NSCAT data during January 1997. Figure 4.10(a) is the map of NSCAT mean response, A_θ , showing that the ergs have a mean σ° response below -20 dB. Figure 4.10(b) shows average wind behavior during January 1997 over the major ergs of the Sahara. ECMWF mean wind directions are shown on a $1^\circ \times 1^\circ$ resolution grid whereas model parameters are computed on a $0.5^\circ \times 0.5^\circ$ resolution grid. m_1 and m_2 have high magnitudes over ergs compared to the other parts of the Sahara desert. Since the maps are plotted for $\theta = 33^\circ$, these magnitudes reflect the relative strength of the signal caused by slip-sides in different ergs. Note that in almost all ergs, the difference in the directions ψ_1 and ψ_2 is approximately equal to 180° . Comparing 4.10(b) and (d) reveals that, in general, ψ_1 is similar to the average wind direction in the ergs. Most of the slip-sides in northern ergs have their orientation eastwards, matching the direction of westerly trade winds whereas the southern ergs match the easterly trade winds.

The Sahara desert includes large mountain ranges called *Hamadas* that block and divert the near-surface winds, resulting in wind shadows. We note that ergs are large bowl-like basins formed in the inter-mountain regions. The ECMWF winds do not include mountain effects but the ergs do effect the intra-erg wind behavior. ψ is computed based on the surface geometrical characteristics and thus reflects the near surface wind characteristics. The observed ψ reveals the wind diversion caused by the mountains. This is reflected in the ψ spatial variability between the wind inlets and outlets of the ergs. These results are further confirmed when compared to the average January wind maps reported by [72] and shown with thick arrows in 4.10(b). The RMS deviation of ψ_1 to ECMWF mean winds is 27° .

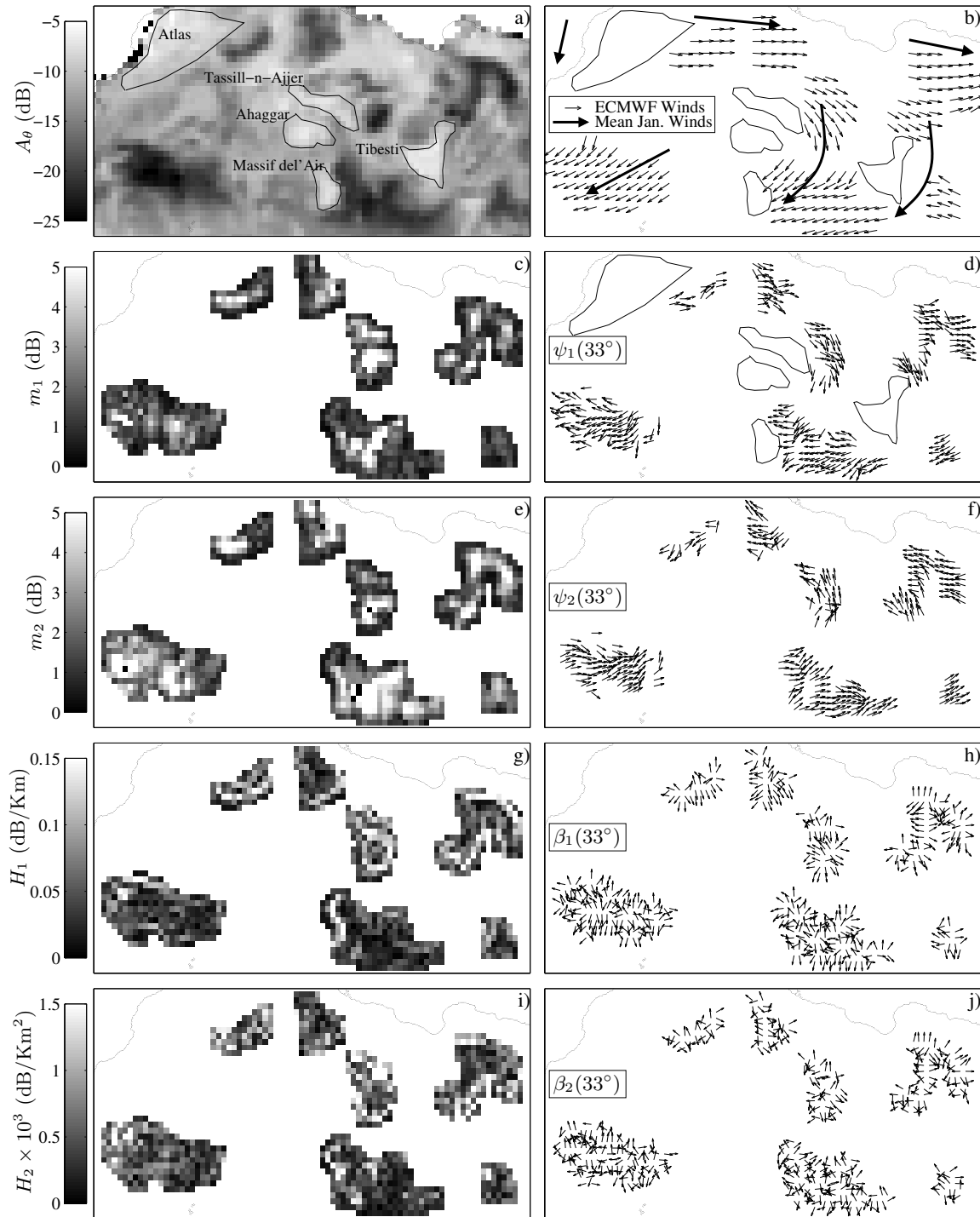


Figure 4.10: Spatial maps of the model parameters at $\theta = 33^\circ$ from NSCAT data during JD 1-30, 1997 for Saharan ergs. a) A_θ , c) m_1 , d) ψ_1 , e) m_2 , f) ψ_2 , g) H_1 , h) β_1 , i) H_2 and j) β_2 . b) Average wind behavior over the ergs during January.

The magnitude of the first order spatial inhomogeneity is highest at the erg boundaries consistent with a change of terrain from sandy surface to Hamadas. The high first order spatial inhomogeneity magnitudes mark the boundaries of major ergs [see Fig. 4.10(g)]. In the central erg regions, H_1 is lower indicating that the σ° is mainly effected by $q_\theta(\phi)$ and has lesser contribution from $h_\theta(r, \beta)$. The second order inhomogeneity is also high closer to the fringes of the ergs and its direction is almost equal to first order inhomogeneity at most parts of the erg boundaries.

Fig. 4.11(a) and (b) compare the average July, 1997 ECMWF winds to ψ_1 computed from ESCAT data and are similar to NSCAT. ESCAT ψ_1 has smoother spatial behavior because of the coarser ESCAT resolution and the fact that a 100 km radius is used to compute the model parameters. The RMS deviation of ESCAT ψ_1 from ECMWF winds is 29° . The first and second order inhomogeneities are consistent with NSCAT. Fig. 4.11(c) is the spatial map of ψ_1 directions computed from QSCAT data. Average winds during July reported by [72] are also shown with thick arrows. We note that QSCAT ψ_1 is computed at 54° and does not always reflect the orientation of the slip-side. This is evident by the higher deviations of its spatial map from the ECMWF winds.

Figure 4.12 shows a similar comparison in the Empty Quarter of the Arabian peninsula. NSCAT and ESCAT provide similar ψ directions, which deviate from ECMWF winds. These ψ directions are similar to the aeolian sand transport directions reported by [73] shown with dashed arrows in Fig. 4.12(a). The spatial behavior of ψ is similar to the spatial behavior of the near-surface dominant wind directions. The model results have higher error in complex surface bedforms with more than two slip-sides. These bedforms result from highly variable wind directions and thus the surface bedform response to winds is more complicated compared to areas with simple dunes caused by less variable winds.

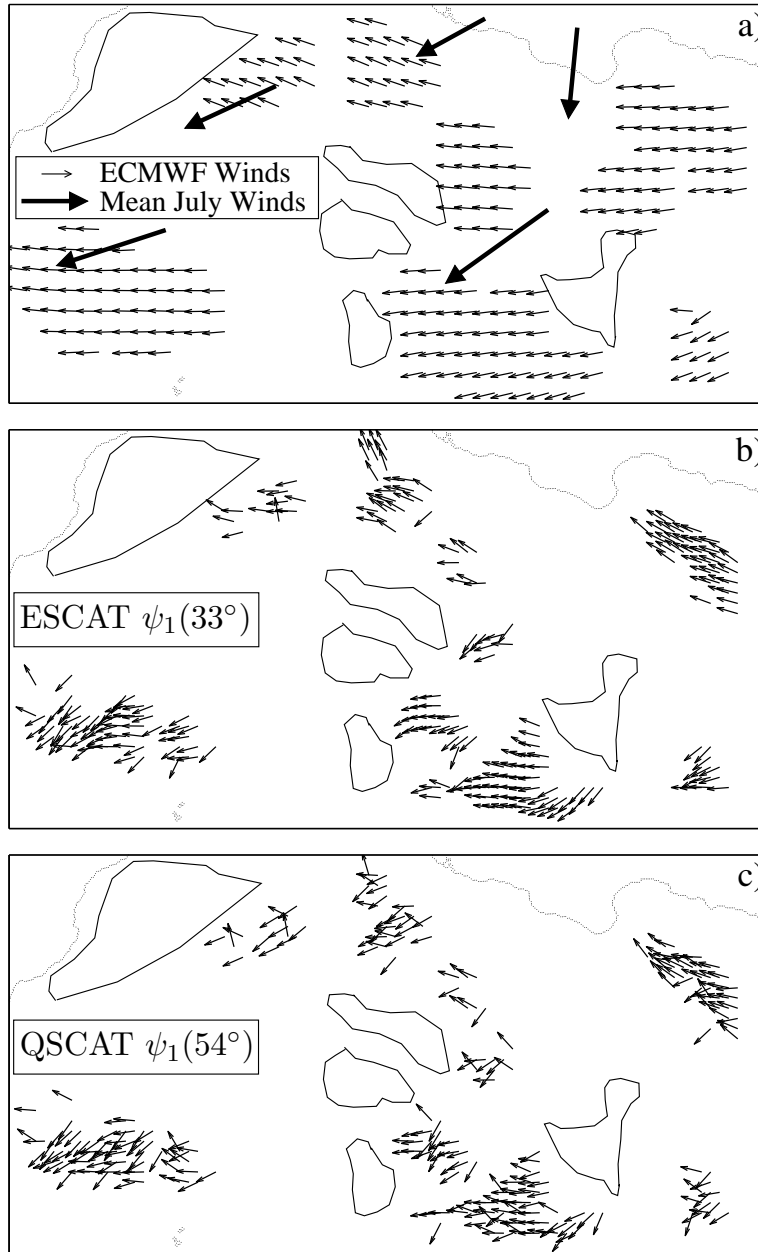


Figure 4.11: a) Average wind map JD 182-212, 1997. b) ψ_1 computed for ESCAT data corresponding to a) and c) ψ_1 computed for QSCAT data during JD 182-212, 2000.

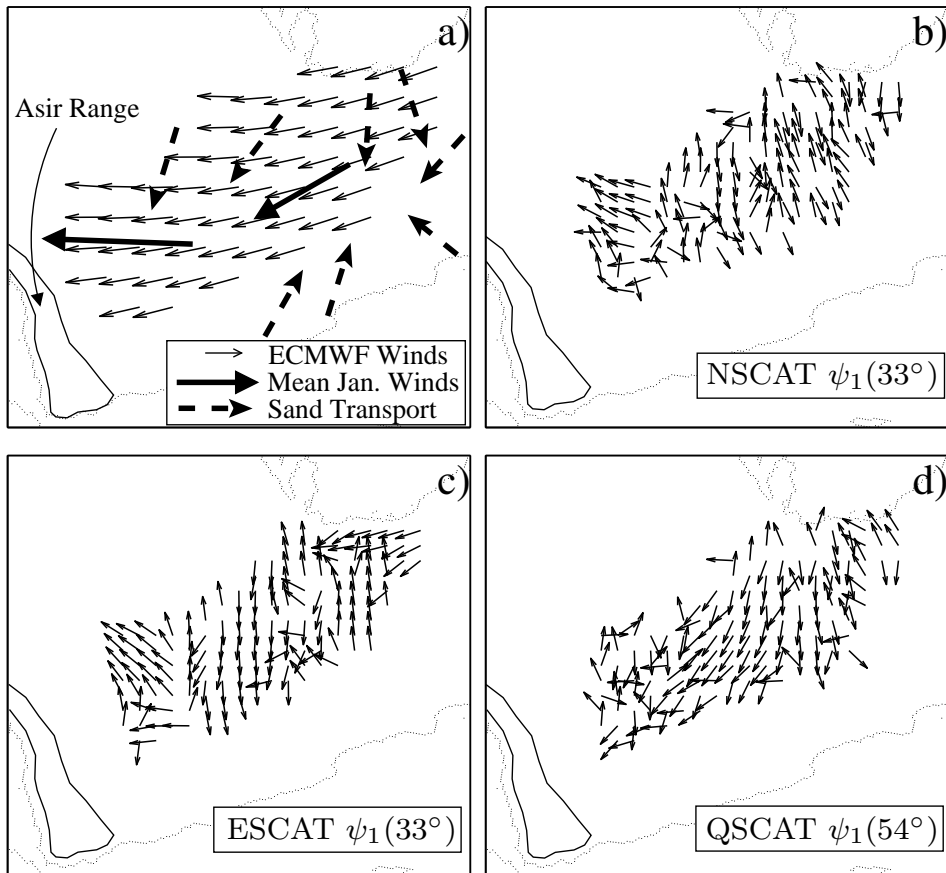


Figure 4.12: a) Average wind behavior in Empty Quarter during JD 1-30, 1997. b) and c) ψ spatial maps computed from NSCAT and ESCAT data during JD 1-30, 1997. d) ψ spatial map computed from QSCAT data during JD 1-30, 2000.

4.2.3 Temporal Behavior of Model Parameters

In this section, the temporal variability of ECMWF average winds is compared to the derived ψ orientations. Figure 4.13 shows plots of the monthly average ECMWF wind directions and ψ orientations computed every 15 days between October, 1996 and July, 1997. In these locations, the ECMWF wind directions match reasonably to the ψ orientations. The temporal variations of ECMWF wind and ψ are similar, but differ in absolute values. This suggests that the small scale ripples are not absolutely aligned to the prevailing winds. Nevertheless they exhibit a temporal behavior consistent with temporal variations of the wind at all the selected locations. The deviation of the two measurements increases as the surface complexity of the bedform increases. Figure 4.14 shows the long-term comparison of ECMWF winds and ψ computed from ESCAT at two locations.

The time series of ψ and ECMWF wind direction are similar at many locations in the ergs. Where they differ, the difference is attributed to the different scopes of the two wind sources. ECMWF wind is numerically predicted and presents the large-scale average behavior of the prevailing wind whereas ψ is retrieved from the erg bedform geometry and is a measure of the near-surface aeolian phenomena.

4.3 Summary

The erg surface geometry response to the near-surface prevailing wind is very complicated. σ° measurements over ergs are influenced by the ergs' general topography and dune geometry, and are a function of sensor view angles and footprint centroid location. A new model provides measures of σ° ϕ -modulation and σ° spatial inhomogeneity, which shows that, over ergs, θ plays a key role in varying the ϕ -modulation and σ° centroid displacement variability. The ϕ -modulation of σ° measurements at $\theta = 33^\circ$ are used to relate the dune slip-side orientations to the prevailing wind over erg bedforms. Over the areas with simple dunes and less variable wind, the model-inferred wind is spatially and temporally similar to the ECMWF wind. The model accuracy is reduced over the areas with complex bedforms and high wind variability. NSCAT, ESCAT and QSCAT show similar results.

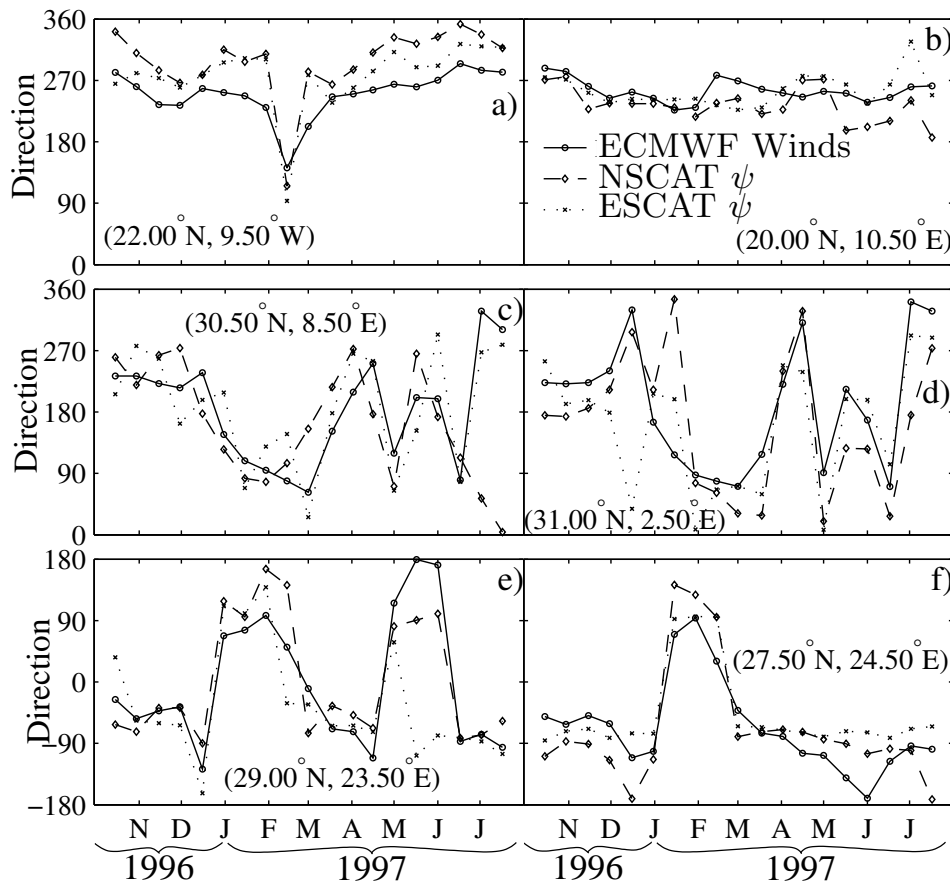


Figure 4.13: Plots of temporal behavior ECMWF mean wind directions and ψ_1 orientations derived from NSCAT and ESCAT σ° measurements at six locations in Saharan ergs.

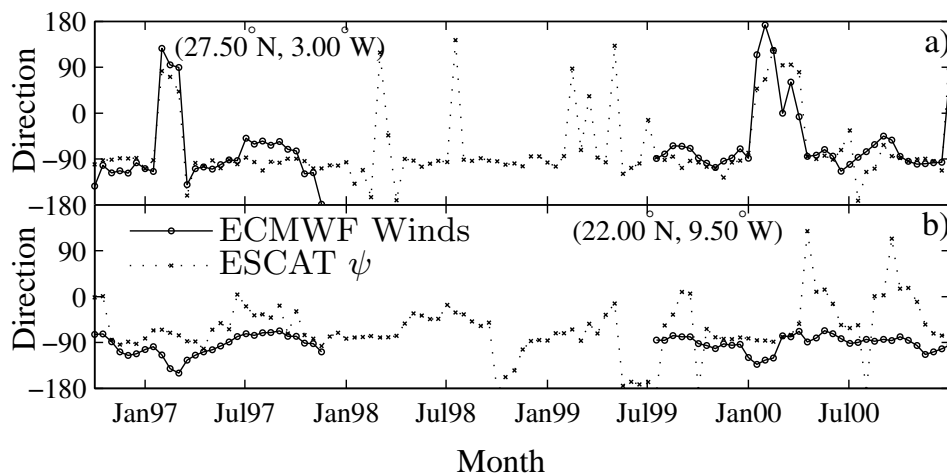


Figure 4.14: A comparison of the long-term temporal behavior of ECMWF mean wind directions and ψ_1 orientations derived from ESCAT data at two locations.

Chapter 5

Modeling Microwave Emissions of Erg Surfaces

This chapter studies the microwave emissions from erg surfaces. It shows that there is significant azimuth angle modulation of radiometric temperature over sand surfaces caused by sand bedform features. The dual polarization T_b measurements at 19 GHz and 37 GHz from SSM/I and TMI and simple electromagnetic models are used to study the radiometric response of erg surfaces. An observational empirical model is introduced that combines SSM/I and TMI data to estimate the T_b azimuthal anisotropy over sand surfaces. It is shown that the observed T_b is modulated by the look direction and that the modulation is a function of the surface profile. The modulation indicates the surface characteristics i.e., dune types and their orientation. Shadowing and sun illumination effects are ignored in explaining the radiometric behavior of sand. This material has been published in [6].

Sand radiometric emission is described in Section 5.1 along with a simple facet model to explain the dual polarization emission over sand dunes. Section 5.1 also includes the model simulation of T_b azimuth angle (ϕ) modulation over simple dunes. The ϕ -modulation and time-of-day (t_d) modulation of the observed T_b data and a comparison to model simulation results are given in Section 5.2. This section also compares the T_b observations at 19 GHz and 37 GHz frequencies.

Three erg sites that have flat sand sheets, transverse dunes and longitudinal dunes located at 31.7°N, 0.5°E (location 1), 17.5°N, 9.3°W (location 2) and 17.5°N, 15.35°W (location 3), respectively, are selected to study the T_b response.

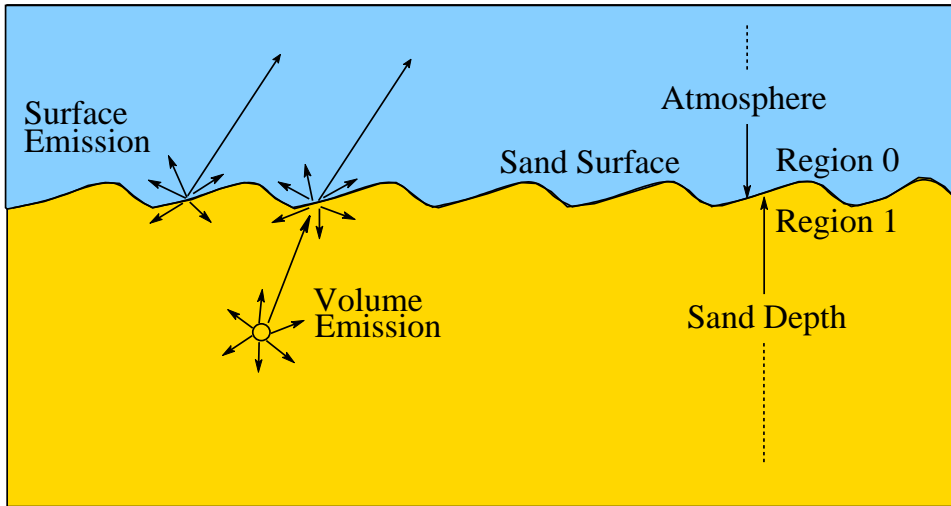


Figure 5.1: Diagram showing a simple sand surface with surface and volume emission components.

5.1 Radiometric Emission from Sand

In this section, a theoretical model of radiometric emission over sand is described in 5.1.1. It is followed by a description of a simple rough facet model of radiometric temperature in 5.1.2. Section 5.1.3 presents the simulation of the model over simple dune shapes.

5.1.1 Radiometric Emission Model

The total emission is the sum of volume and surface emissions [see Fig. 5.1]. Volumetric emission is nearly isotropic and unpolarized. The air-sand boundary transmission coefficient for V-pol and H-pol polarizations depends on θ , resulting in θ -dependence of T_b . Furthermore, local incidence angle (θ') of tilted dune facets changes with azimuth angle, resulting in ϕ -dependence of T_b . Thus, T_b observed by the radiometer is a result of volumetric emission of the sand, modulated by the look direction due to the local surface slope variations.

The radiometric emission model for a layered dielectric material given in (Eqs. 5.2.36a and 5.2.36b [66]) is used with $n + 1$ layers where the $(n + 1)$ th layer

extends infinitely below the n th layer. T_l and ϵ_l denote the physical temperature and electrical permittivity of the l th layer, respectively, and d_{l-1} and d_l denote the distance of the layer's upper and lower boundaries, respectively, from the air-sand boundary. In the model, the sampling depth is divided into n layers with the $(n + 1)$ th layer being the remaining half space of sand below sampling depth. Thus, the distance of the lower boundary of the n th layer is equal to the sampling depth i.e., $d_n = \tau$.

Sand is a spatially homogeneous medium. It is modeled as an infinite half space with isothermal horizontal strata and a smooth vertical temperature profile. Since sand in the Sahara desert has a low moisture content that does not change over time, sand is assumed to have a temporally stable dielectric constant. Moreover, it is assumed that the sand dielectric constant to be spatially homogeneous within the footprint of observation. The vertical temperature profile of sand depends on time-of-day and season (time-of-year). During the day time, the sand surface temperature is higher than the subsurface temperature, and lower at night. A mean diurnal temperature profile is applied to the model and assumed to fall off exponentially from a surface temperature (T_0) to a nominal subsurface temperature (T_τ) over the sampling depth τ (see Fig. 5.2). After applying these considerations, the radiometric temperature for H-pol (T_{bh}) and V-pol (T_{bv}) given in [66] becomes

$$T_{bh}(\theta) = \frac{k_0}{\cos \theta} \frac{\epsilon_1''}{\epsilon_0} |T_{01}^{TE}|^2 \left[T_t e^{-2k_{1z}'' d_n} - \sum_{l=1}^n \{ T_l (e^{-2k_{1z}'' d_l} - e^{-2k_{1z}'' d_{l-1}}) \} \right] \quad (5.1)$$

$$\text{and } T_{bv}(\theta) = \frac{k_0}{\cos \theta} \frac{\epsilon_1''}{\epsilon_0} \left(\frac{|k_{1z}|^2 + k_x^2}{|k_1|^2} \right) \left| \frac{k_0}{k_1} T_{01}^{TM} \right|^2 \times \left[T_t e^{-2k_{1z}'' d_n} - \sum_{l=1}^n \{ T_l (e^{-2k_{1z}'' d_l} - e^{-2k_{1z}'' d_{l-1}}) \} \right] \quad (5.2)$$

where k_0 , θ and ϵ_0 are the wave number, incidence angle and electrical permittivity in the air, respectively. k_1 and k_{1z} are the wave number and its z component in the sand, respectively. ϵ_1'' and k_{1z}'' denote the imaginary parts of complex electrical permittivity and k_{1z} in sand, respectively. $k_x = k_0 \sin \theta$ is the surface component of incident wave number. T_{01}^{TE} and T_{01}^{TM} denote the transmission coefficients between

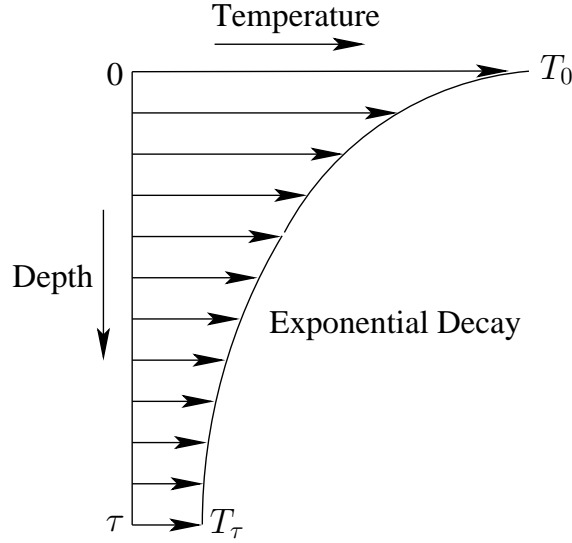


Figure 5.2: Diagram showing vertical temperature profile of sand subsurface.

air and sand for H- and V-pol, respectively. T_l and T_t are the physical temperatures of l th and $(n + 1)$ th layer, respectively.

Dry sand has a low relative electrical permittivity (ϵ_r) and I use a nominal value of $2 + i10^{-4}$ in the simulation of Eq. 5.1 [74]. The corresponding Brewster angle is approximately 55° . The diurnal mean surface and subsurface temperatures are assumed to be $330K$ and $310K$ with a sampling depth of 6 cm (about 4 wavelengths at 19 GHz) and $n=100$ (101 layers). Figure 5.3(a) shows θ -response of both T_{bh} and T_{bv} computed from Eq. 5.1. At nadir, V-pol and H-pol T_b have the same value and T_{bh} decreases as θ is increased. On the other hand, T_{bv} increases initially and reaches its maximum at the Brewster angle beyond which it rapidly rolls-off. T_{bv} is higher than T_{bh} for off-nadir incident directions and the difference between two radiometric temperatures is also a function of θ . The polarization difference (ΔT_b) is defined as

$$\Delta T_b(\theta, \phi) = T_{bv}(\theta, \phi) - T_{bh}(\theta, \phi). \quad (5.3)$$

The local incidence angle θ' is a function of look direction (θ, ϕ) and surface tilt (θ_s, ϕ_s) where θ_s and ϕ_s are the spherical angles of the facet's unit normal. Since SSM/I and TMI observations are made at fixed $\theta = 53^\circ$, for a fixed azimuth direction

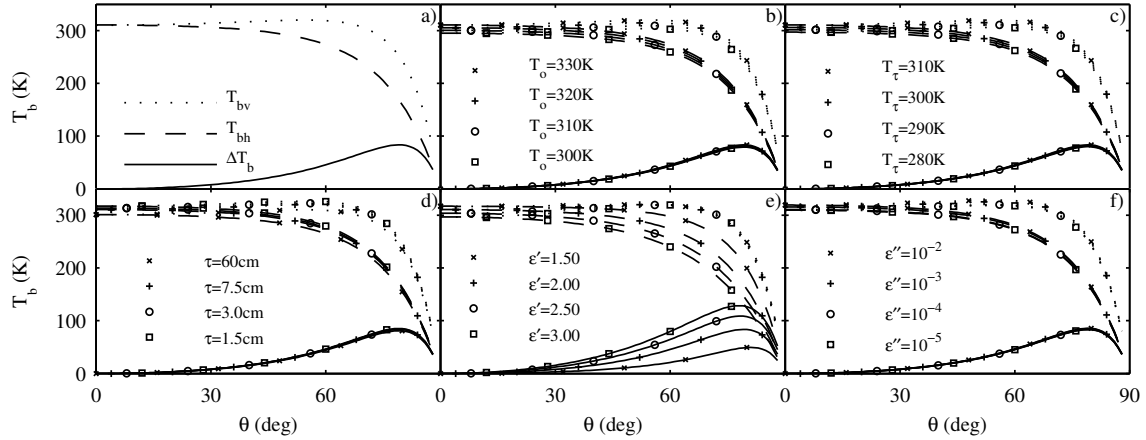


Figure 5.3: a) T_b and ΔT_b model simulations for $T_0=330K$, $T_\tau=310K$ and $\tau=6 cm$ when a radiometer observes sand material with $\epsilon_r=2 + i10^{-4}$ at 19GHz frequency. Plots b)-d) show changes in plot a) due to variations in model parameters. b) and c) depict the dependence on surface and subsurface nominal temperature, respectively. d) shows the variations with sampling depth. e) and f) illustrate the dependence on the real and imaginary parts of relative electrical permittivity of the material, respectively.

ϕ the local incidence angle θ' depends only on (θ_s, ϕ_s) . Thus, ΔT_b is a function of tilt of the surface. This also makes the polarization of the emitted wave a function of the surface tilt, i.e., a wave from a tilted surface has a different polarization than from a flat surface. Figure 5.3(a) also shows the incidence angle dependence of ΔT_b , which gradually increases with θ (ΔT_b is zero at nadir), and decreases rapidly back to zero at grazing incidence angles. Plots 5.3(b)-(f) illustrate the sensitivity of T_b and ΔT_b to other model parameters. The responses have insignificant dependence on surface temperature [Fig. 5.3(b)] and sampling depth [Fig. 5.3(d)]. Subsurface nominal temperature [Fig. 5.3(c)] and the imaginary part of complex electrical permittivity [Fig. 5.3(f)] alter the T_b response but do not have significant effect on ΔT_b . The real part of complex electrical permittivity has the most significant effect on ΔT_b [Fig. 5.3(e)]. This analysis demonstrates that ΔT_b mainly depends on the real part of ϵ_r and, for practical purposes, is insensitive to other model parameters. This makes ΔT_b very suitable for modeling the ϕ -response over the sand dune bedforms.

5.1.2 Facet Model

An erg is composed of large scale dunes that are modeled as rough facets with a tilt distribution. Each rough facet is characterized by a tilt distribution $P(\theta_s, \phi_s)$, which is the probability of occurrence of a local unit normal in the (θ_s, ϕ_s) direction. I model T_b from a tilted facet (denoted T_{bf}) as the weighted average of T_b from all parts of the facet where the probability distribution of tilt is used as the weighting function. T_{bf} as a function of look direction (θ, ϕ) and polarization p is given by

$$T_{bf}(\theta, \phi; p) = \int T_b(\theta'; p, T_o, T_\tau, \tau) P(\theta_s, \phi_s) d\theta' \quad (5.4)$$

where θ' is the local incidence angle, which is a function of the surface tilt (θ_s, ϕ_s) and radiometer's look direction (θ, ϕ) . $T_b(\theta'; p, T_o, T_\tau, \tau)$ is the radiometric response of a flat facet (with zero tilt) as given in Fig. 5.3(a). A zero-tilt facet is azimuthally isotropic, i.e., $T_b(\theta, \phi) = T_b(\theta)$ and $\theta' = \theta$; thus, any azimuthal anisotropy results from the non-zero tilt of the facet surface. ΔT_b of a facet is given by

$$\Delta T_{bf}(\theta, \phi) = \int \Delta T_b(\theta') P(\theta_s, \phi_s) d\theta'. \quad (5.5)$$

Note that dependence on polarization and thermal characteristics is dropped since ΔT_b is independent of these characteristics.

The response of the dunes is the linear combination of the responses from the individual dominant facets weighted by their projected area. Thus, I model the total radiometric response from dunes (denoted T_{bd}) at p -polarization to be

$$T_{bd}(\theta, \phi; p) = \frac{1}{A'} \sum_n A'_n \int T_b(\theta'; p, T_o, T_\tau, \tau) P_n(\theta_s, \phi_s) d\theta' \quad (5.6)$$

where A' and A'_n are the projected areas of the antenna foot print and n th rough facet, respectively (Fig. 5.4). The summation is over all the dominant rough facets in the footprint of the sensor. If \hat{A} is the surface area illuminated at an incidence angle θ , and A_n is the actual surface area of the facet with a local incidence angle θ'_n , then $A' = \hat{A} \cos \theta$ and $A'_n = A_n \cos \theta'_n$. The tilt angle θ_{sn} of the facet is related to its

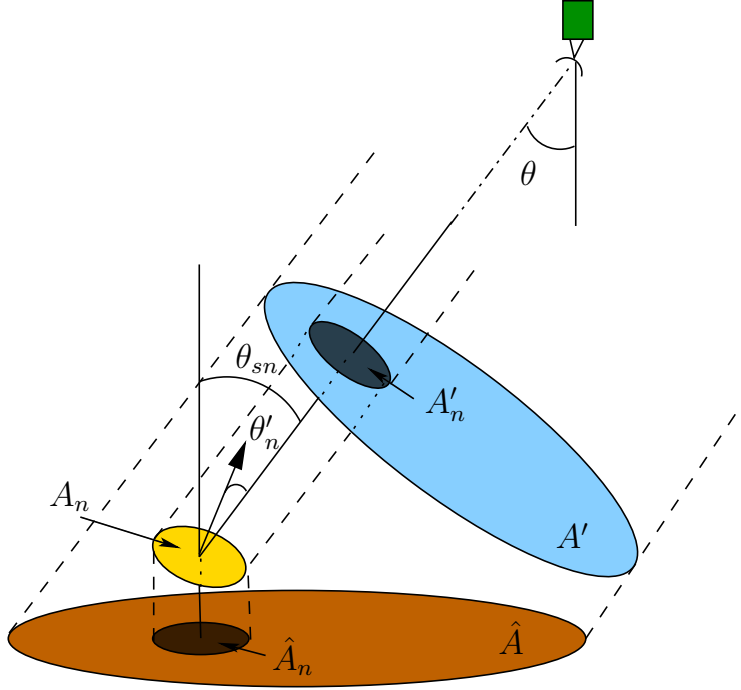


Figure 5.4: Area of facet projection onto antenna beam cross-section and ground surface.

horizontal projection (\hat{A}_n) by $\hat{A}_n = A_n \cos \theta_{sn}$. These relationships in Eq. 5.6 give

$$T_{bd}(\theta, \phi; p) = \sum_n \frac{F_n \cos \theta'_n}{\cos \theta_{sn} \cos \theta} \int T_b(\theta'; p, T_o, T_\tau, \tau) P_n(\theta_s, \phi_s) d\theta' \quad (5.7)$$

$$\text{where } F_n = \frac{\hat{A}_n}{\hat{A}}.$$

F_n is the fraction of footprint area covered by the n th facet that has a mean tilt angle θ_{sn} and a mean local incidence angle θ'_n . F_n is related to the dune shape and is easily estimated for simple dunes. The net ΔT_b over the dune field is given by

$$\Delta T_{bd}(\theta, \phi) = \sum_n \frac{F_n \cos \theta'_n}{\cos \theta_{sn} \cos \theta} \int \Delta T_b(\theta') P_n(\theta_s, \phi_s) d\theta'. \quad (5.8)$$

5.1.3 ΔT_b Response over Model Dunes

In this section the rough facet model (Eqs. 5.7-5.8) is used to determine the simulated T_b and ΔT_b response over simple dune surfaces. First, the simulation

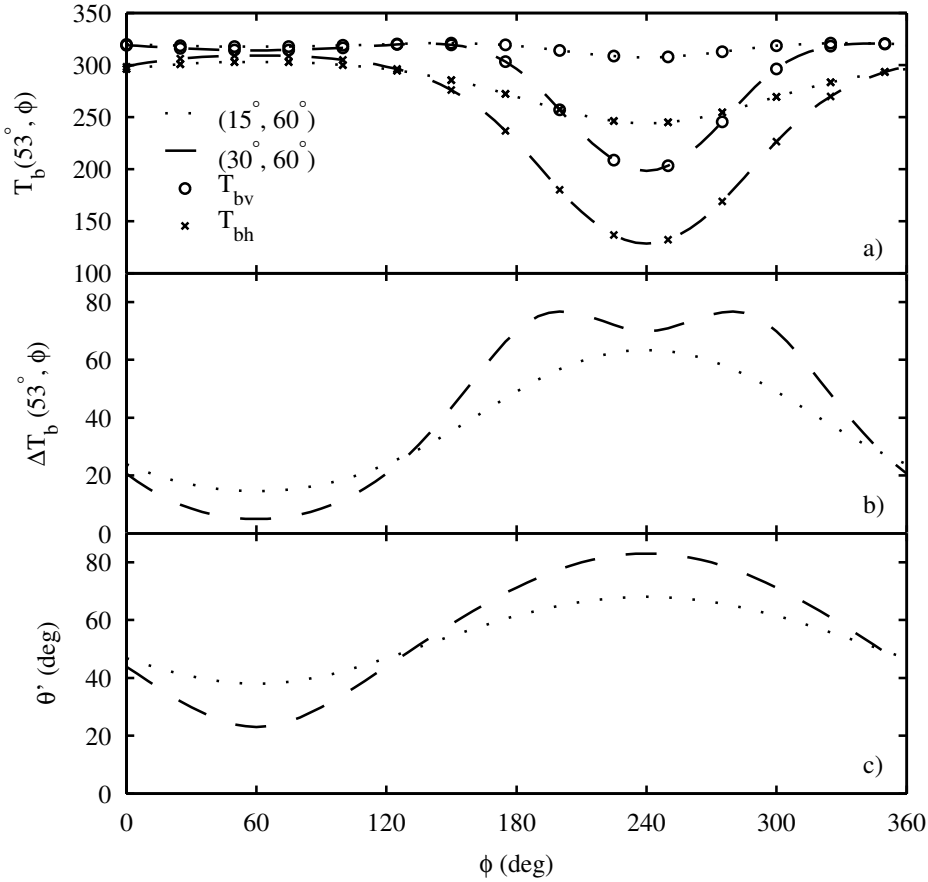


Figure 5.5: Computed a) T_b and b) ΔT_b ϕ -response over two different facets with Gaussian tilt distribution. c) plots corresponding θ' variations with ϕ .

results over single tilted facets are presented. The facet radiometric response model (Eqs. 5.4-5.5) is applied separately to two different facets tilted at 15° and 30° that correspond to the wind- and slip-side slopes of a transverse dune. The azimuth orientation ϕ_s of the facets is 60° . The α -angle is defined as the sensor azimuth angle relative to the facet azimuth orientation given by $\alpha = \phi - \phi_s$. Figure 5.5 shows the ϕ -response of simulation results at a sensor incidence angle of 53° (corresponding to the incidence angle of SSM/I and TMI). The magnitude of H- and V-pol T_b ϕ -modulation increases with the slope of the facet and minimum T_b occurs when $\alpha=180^\circ$. T_{bv} is higher than T_{bh} , and the difference ΔT_b is minimum at $\alpha=0^\circ$ [Fig. 5.5(b)] since θ' is

minimum at this α -angle [Fig. 5.5(c)]. The maximum of ΔT_b and θ' occur at $\alpha=180^\circ$. For steeper facets, θ' approaches grazing angles at $\alpha=180^\circ$, resulting in a drop of ΔT_b at the facet grazing angle [Fig. 5.3(a)].

The T_b ϕ -response of a tilted facet depends upon the slope and azimuth orientation of the facet: T_b is inversely proportional to the local incidence angle, T_{bv} and T_{bh} have distinct ϕ -responses, and T_{bv} is higher in magnitude than T_{bh} . ΔT_b is directly proportional to θ' . The minima and maxima of ΔT_b ϕ -modulation over tilted facets correspond to α -angles of 0° and 180° , respectively. In the next two subsections, the results of the simulation over model longitudinal and transverse dunes are presented.

Longitudinal Dunes

A longitudinal dune is characterized by two slip sides and a flat inter-dune area as shown in Fig. 5.6. The slope of both slip-sides is 30° - 35° (the angle of repose of sand) and their azimuth orientations differ by 180° . The long axis of the dune is 90° relative to the azimuth directions of the slip-sides and is along the mean wind direction that formed the dune. The longitudinal dune is modeled as a composite of three rough facets that correspond to two slip-sides and an inter-dune flat surface. The cross section of a longitudinal dune shown in Fig. 5.6(c) indicates the minimum and maximum local incidence angles resulting from the slopes of the facets as viewed by a sensor at an incidence angle of 53° . As ϕ changes, θ' of the facet changes between the minimum and maximum values. In the model simulation, the two slip-sides have a Gaussian tilt distribution for (θ_s, ϕ_s) with means $(30^\circ, 170^\circ)$ and $(30^\circ, 350^\circ)$ and standard deviations of 5° each. The covariance between θ_s and ϕ_s is assumed to be zero in this research. The flat inter-dune facet has a mean tilt of $(0^\circ, 0^\circ)$ with a standard deviation of $(5^\circ, 10^\circ)$ and zero covariance. Figure 5.7 shows the model T_b and ΔT_b results. The two slip-sides of the longitudinal dune result in two maxima in T_{bh} , and two minima in T_{bv} ϕ -responses. The ϕ angle at which these maxima or minima occur correspond to the azimuth directions of the facets. This opposite behavior of T_{bv} and T_{bh} results in minimum ΔT_b when ϕ is along the azimuth

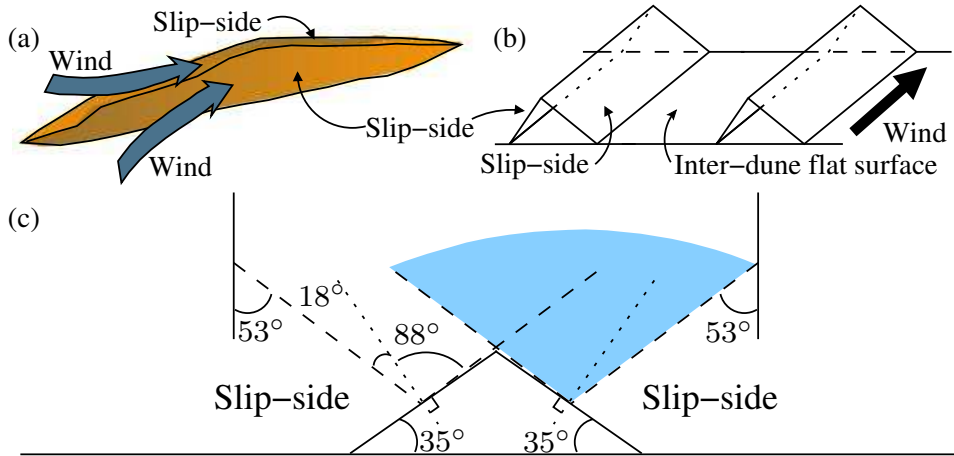


Figure 5.6: a) Longitudinal dune, b) its three-facet-model and c) cross section of a typical dune. The shaded portion is the projection of the cone of view formed by all view azimuth angles. The cone represents the range of local incidence angles for the given tilt.

directions of the slip-sides. ΔT_b is minimum when a slip-side has a near nadir view and increases when ϕ is changed from this direction. Simultaneously, the contribution from the other slip-side starts increasing and this results in an azimuth modulation signal in ΔT_b with peaks occurring when ϕ is along the axis of the dune. ΔT_b is maximum at ϕ directions along the axis of the dune.

Transverse Dunes

A transverse dune has a wind-side slope of 10° - 15° and a slip-side slope similar to a longitudinal dune. The azimuth directions of these two sides differ by 180° . The axis of the dune is defined similar to a longitudinal dune, but the wind direction that produces this dune corresponds to the azimuth direction of the slip-side, i.e., perpendicular to the long axis of the dune. The transverse dune is modeled as a composite of three rough facets that correspond to a slip-side, a wind-side and an inter-dune flat surface. Figure 5.8(b) illustrates the three-facet-model for a transverse dune. Figure 5.8(c) shows the cross section of a transverse dune where the shaded

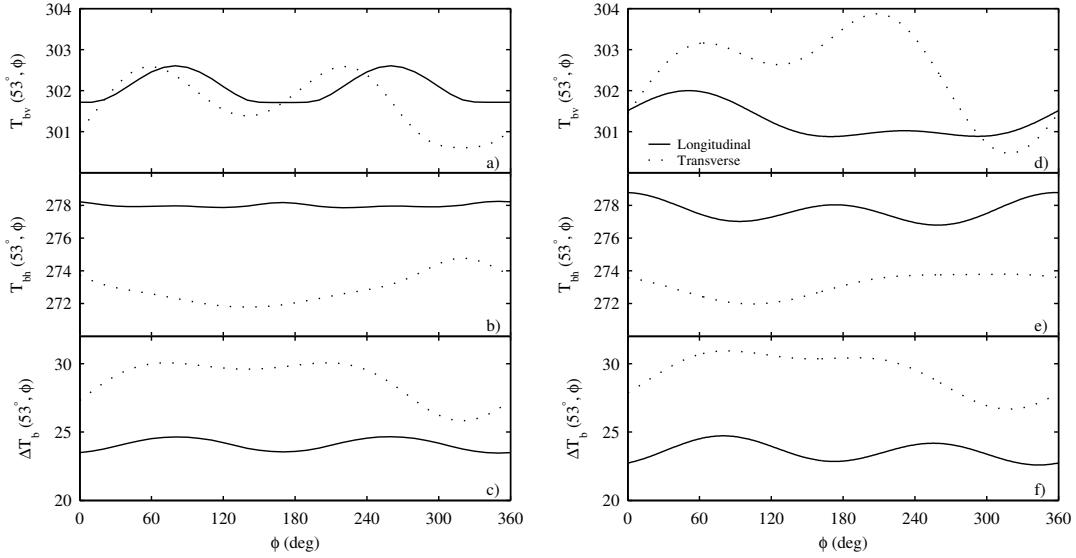


Figure 5.7: a)-c) simulated T_b and ΔT_b responses over triple facet transverse and longitudinal dune models. d)-f) T_b and ΔT_b responses derived from SSM/I and TMI observed data at 19 GHz (see text).

portion represents the range of possible local incidence angles for each facet viewed at $\theta = 53^\circ$.

Inter-dune flat facet, wind-side and slip-side are assumed to have Gaussian tilt distributions for (θ_s, ϕ_s) with means $(0^\circ, 0^\circ)$, $(12^\circ, 320^\circ)$ and $(30^\circ, 140^\circ)$, respectively, and standard deviations $(3^\circ, 5^\circ)$, $(3^\circ, 10^\circ)$ and $(3^\circ, 10^\circ)$, respectively. The covariance between θ_s and ϕ_s is zero. Figure 5.7 shows the model results for a transverse dune. The T_b ϕ -response is similar to longitudinal dunes, but has a higher magnitude of modulation. In ΔT_b response, the global minimum in the ϕ modulation occurs in the azimuth direction of the slip-side of the dune whereas a second minimum occurs at the wind-side azimuth direction. Figures 5.7(d)-(e) summarize the ϕ -modulation of the observed data described in Section 5.2.

The analysis of model simulations over individual facets and composite facet surfaces suggest that T_{bv} and T_{bh} have significant ϕ -modulation caused by the tilted rough surfaces. Since ΔT_b is independent of the thermal characteristics of the surface, its ϕ -modulation is only dependent upon the dielectric constant and surface

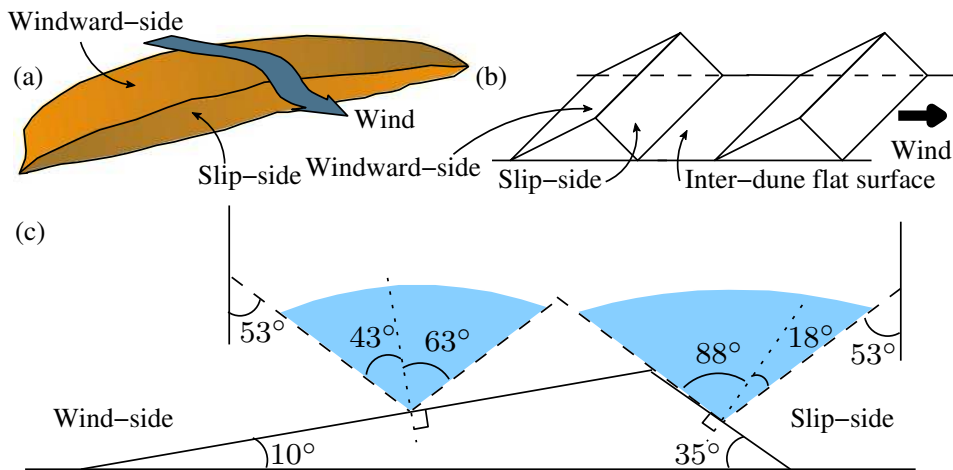


Figure 5.8: a) Transverse dune, b) its three-facet-model and c) cross section. The shaded portion is the projection of the cone of view formed by all view azimuth angles. The cone represents the range of local incidence angles for the given tilt.

geometrical characteristics. Model simulations at 37 GHz give similar ϕ -modulation with a lower mean value due to higher attenuation. The ΔT_b ϕ -modulation of model dune surfaces reflects the presence of tilted facets and helps identify the underlying dune types.

5.2 Spaceborne T_b Observations

In this section, dual polarization 19 GHz and 37 GHz T_b measurements from TMI and SSM/I over Saharan ergs are used to analyze the radiometric emission behavior of dunes in comparison with model prediction. TMI and SSM/I make T_b measurements at an incidence angle of 52.75° and 53.4° , respectively. The scan pattern of TMI and SSM/I sensors, in combination with the orbit geometry of the ascending and descending passes, provides T_b measurements sampled at many azimuth angles.

The orbit of the TRMM satellite is inclined at approximately 30° . The orbit longitude of the ascending node shifts every repeat cycle. This helps TMI acquire T_b measurements of the target sampled at various times-of-day. SSM/I acquisition of

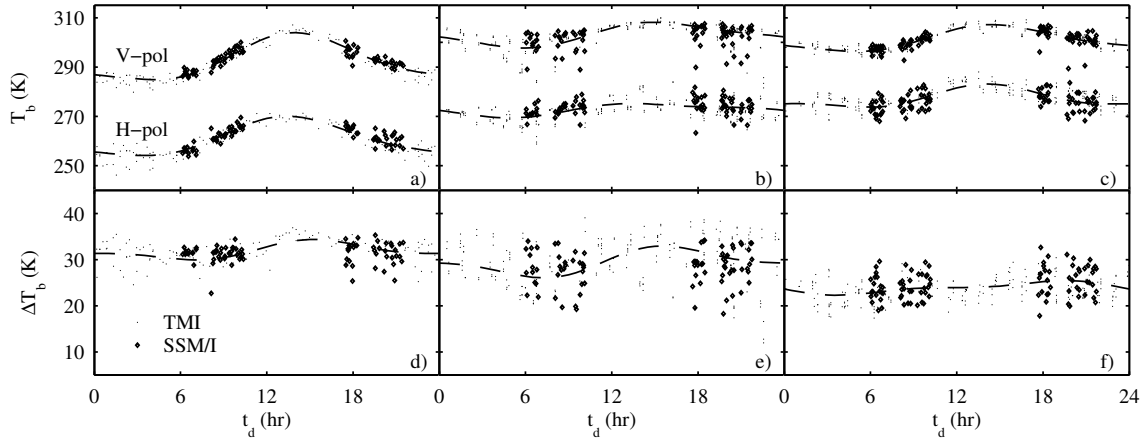


Figure 5.9: Dual polarization 19 GHz T_b diurnal modulation from TMI and SSM/I over a) a flat sand sheet, b) transverse dunes and c) longitudinal dunes. Corresponding polarization difference is plotted in d), e) and f), respectively. The dashed line represents a second order harmonic fit through the radiometric temperature measurements as a function of time-of-day t_d .

the target is made in a sun-synchronous orbit at two times-of-day. SSM/I data from three DMSP satellites (F13, F14 and F15) is combined to obtain 6 time-of-day (t_d) samples (see Fig. 5.11).

Sand in the tropics undergoes a diurnal cycle of temperature variation. The solar incident radiation intensity is a function of time-of-day and season (time-of-year). Illuminated by the sun during the day, sand absorbs the sun's radiation which increases its internal and surface temperature. Sand cools down during the night by dissipating thermal radiation. Figure 5.9 shows the resulting diurnal variation of T_{bv} and T_{bh} observed by TMI and SSM/I sensors. The data is acquired during JD 185-238, 2002 and is shown for three erg targets: flat sand sheet, transverse dunes and longitudinal dunes. The two sensors show good cross-calibration and similar diurnal modulation. ΔT_b is also plotted and reveals higher noise over the dunes (compared to sand sheet) due to the higher ϕ -modulation caused by dune surface geometry. The small variation of T_b over the sand sheet indicates insignificant ϕ -modulation.

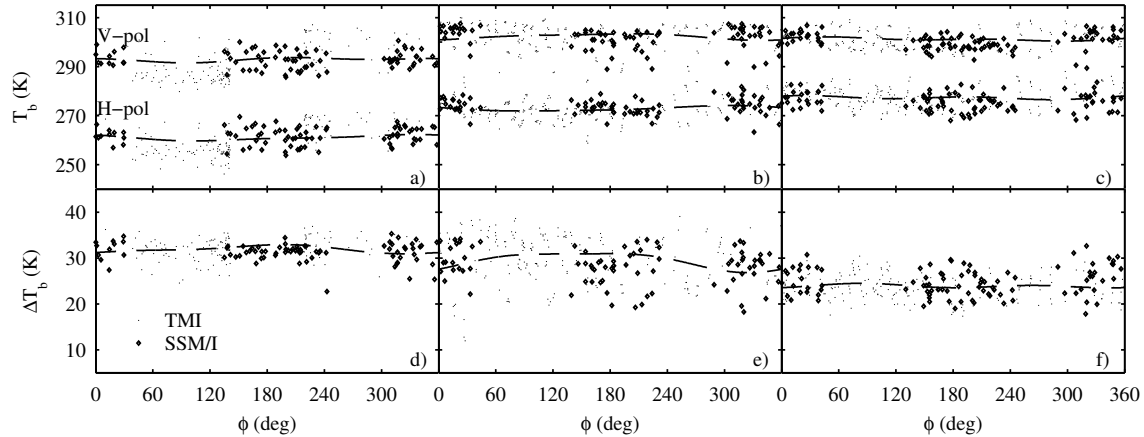


Figure 5.10: Dual polarization 19 GHz T_b azimuth angle modulation from TMI and SSM/I over a) a flat sand sheet, b) transverse dunes and c) longitudinal dunes. Corresponding polarization difference is plotted in d), e) and f), respectively. The dashed line represents a second order harmonic fit through the radiometric temperature measurements as a function of ϕ .

As previously noted, ΔT_b is dependent on the surface profile characteristics and dielectric constant. The local incidence angle over a flat sand sheet [Fig. 5.9(d)] is almost equal to the incidence angle of observation ($\theta' = 53^\circ$) and does not change with the azimuth angle resulting in a ΔT_b of about 30K (Fig. 5.3). Over transverse dunes [Fig. 5.9(e)] the tilt of wind- and slip-sides results in more contribution at relatively smaller local incidence angles, thus reducing ΔT_b . Over the slip-side, the minimum θ' is 18° (Fig. 5.6). This is also evident from the longitudinal dunes [Fig. 5.9(f)] where ΔT_b is further reduced due to the presence of two slip-sides. It should also be noticed that ΔT_b also has a minor diurnal variation. The azimuth angle sampling of the data contributes to ΔT_b diurnal variation. The diurnal variation of the surface emissivity, surface small scale features (ripples), and sun inclination also contribute to ΔT_b diurnal variation. This t_d -response is well modeled by a second order harmonic equation shown with dashed lines.

Figure 5.10 depicts the azimuth angle variation of observed T_b . The magnitude of the azimuth angle modulation is lower than the diurnal modulation but

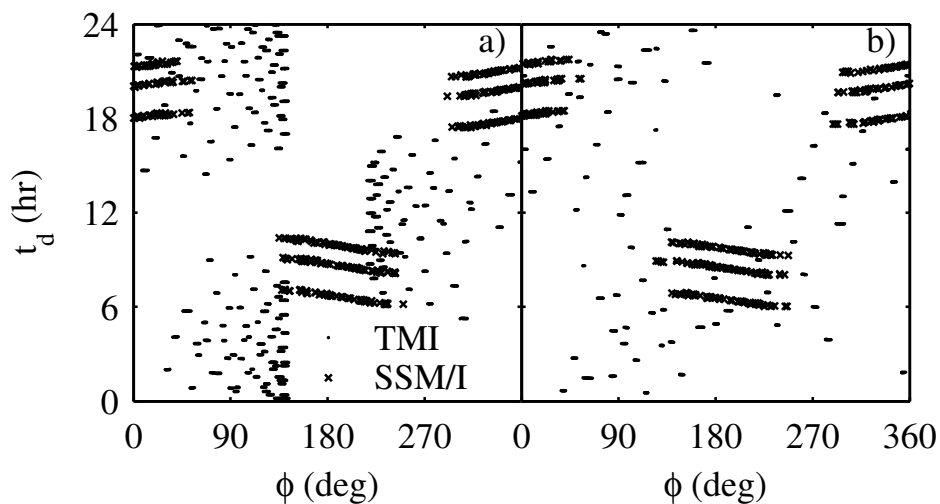


Figure 5.11: ϕ - t_d sampling of data from combined TMI and SSM/I data over a) location 1 and b) location 2 during JD 185-238, 2002.

reveals useful information about the surface bedform characteristics. Combining the data from two sensors results in a denser azimuth angle sampling. The high variance in the data is due to sampling of data at different times-of-day. The analysis of the T_b azimuth angle variation at a narrow range of t_d reveals that T_b ϕ -modulation also follows a second order harmonic relationship shown with dashed lines.

The T_b observations have coupled dependence on the t_d and ϕ . The magnitude of azimuth modulation is very low compared to the magnitude of the diurnal variation. Based on the observed ϕ - and t_d -modulation of both T_b and ΔT_b , a descriptive empirical observation model is used to remove the t_d dependence of the data. I use a simple additive model given by

$$\Delta T_b(t_d, \phi) = T_{bm} + \mathcal{I}_t(t_d) + \mathcal{I}_\phi(\phi) \quad (5.9)$$

$$\text{where } \mathcal{I}_t(t_d) = N_1 \cos\left(\frac{\pi}{12}(t_d - t_{d1})\right) + N_2 \cos\left(\frac{\pi}{12}(2t_d - t_{d2})\right)$$

$$\text{and } \mathcal{I}_\phi(\phi) = M_1 \cos(\phi - \phi_1) + M_2 \cos(2\phi - \phi_2).$$

Table 5.1: Table listing the parameters of model Eq. 5.9 fit to observed data over longitudinal dune at 19 and 37 GHz.

	A	N_1	t_{d1}	N_2	t_{d2}	M_1	ϕ_1	M_2	ϕ_2
T_{bv} 19 GHz	301.31	5.04	-2.29	1.15	0.77	0.37	0.70	0.28	1.31
T_{bh} 19 GHz	277.52	3.33	-2.55	2.46	0.81	0.31	-0.63	0.11	1.62
ΔT_b 19 GHz	23.88	1.22	-1.7	0.60	-1.73	0.23	1.51	0.37	2.90
T_{bv} 37 GHz	296.82	6.34	-2.42	1.61	0.71	0.53	0.49	0.18	1.02
T_{bh} 37 GHz	277.37	4.74	-2.61	2.24	0.68	0.29	-1.08	0.15	3.09
ΔT_b 37 GHz	19.35	1.55	-1.96	0.37	-1.96	0.75	0.81	0.45	2.21

T_{bm} is the mean polarization difference. $\mathcal{T}_t(t_d)$ and $\mathcal{T}_\phi(\phi)$ model the t_d and ϕ dependence of the polarization difference, respectively. In this model the nominal radiometric temperature T_{bm} is modulated by two second order harmonics caused by the time-of-day and the azimuth angle of observation. This empirical model is applied to the data and performs a surface fit to the data using a least square solution. The accuracy of the fit to this model depends upon the ϕ - t_d sampling of the data. ϕ -modulation after removal of t_d dependence from observations is consistent with the theoretical model used in section 5.1. Figure 5.11 shows the ϕ - t_d sampling of the combined TMI and SSM/I data over two target areas. Although the sampling is irregular, sparse and contains large gaps, the least squares fit provides a reasonable estimate of the model parameters. Using both TMI and SSM/I data improves the ϕ -sampling of observations. T_{bv} and T_{bh} dependence on t_d and ϕ is also modeled by a sum of two second order harmonics.

Figure 5.12 illustrates the surface fit to the 19 GHz observed data and slices at particular ϕ and t_d . The solid lines correspond to slices through the surface at different t_d and ϕ as shown on the right side of the surface fit plots. The slice plots also show actual observations selected within $t_d = \pm 2$ hrs and $\phi = \pm 15^\circ$ around the t_d and ϕ values of slice, respectively. Figures 5.12(j)-(l) show the ΔT_b surface fit and slices for 37 GHz. T_{bv} and T_{bh} surface fits for 37 GHz are similar to 19 GHz with different mean T_b . The model parameters of the surface fits are shown in Table 5.1.

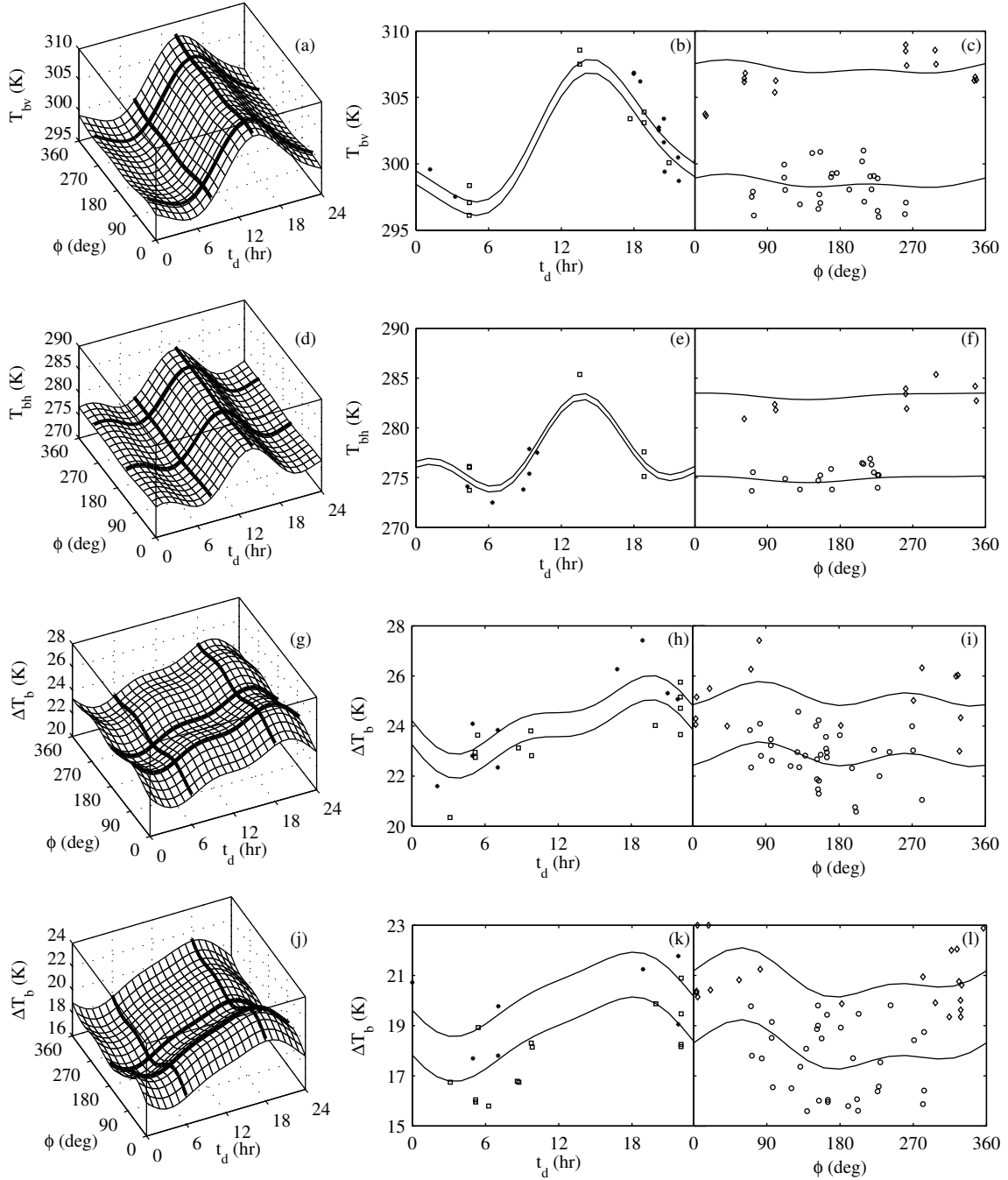


Figure 5.12: Surface of the model fit given in Eq. 5.9 for a longitudinal dune field. Slices through the model fit at fixed ϕ values (left) and fixed t_d values (right) are shown. a), b) and c) are 19 GHz T_{bv} surface model fit, slices through fixed ϕ values and slices through fixed t_d values, respectively. d), e) and f) are 19 GHz T_{bh} surface model fit, slices through fixed ϕ values and slices through fixed t_d values, respectively. g), h) and i) are 19 GHz ΔT_b surface model fit, slices through fixed ϕ values and slices through fixed t_d values, respectively. j), k) and l) are 37 GHz ΔT_b surface model fit, slices through fixed ϕ values and slices through fixed t_d values, respectively.

Table 5.2: Table listing RMS errors for different models and cases used in this research. The standard deviation of raw data (Std) is shown for comparison.

Cases and Frequencies	Std	Empirical Models			Facet model
		t_d	ϕ	t_d & ϕ	
Linear Dune T_{bv} 19 GHz	4.00	1.74	3.49	1.50	4.16
Linear Dune T_{bh} 19 GHz	4.18	2.96	3.83	2.74	4.22
Linear Dune ΔT_b 19 GHz	2.70	2.44	2.55	2.41	2.66
Transverse Dune T_{bv} 19 GHz	5.85	4.44	5.59	4.33	5.92
Transverse Dune T_{bh} 19 GHz	4.19	3.50	3.80	3.36	3.97
Transverse Dune ΔT_b 19 GHz	5.22	4.95	5.17	4.83	5.31
Linear Dune T_{bv} 37 GHz	4.95	2.01	4.38	1.64	12.01
Linear Dune T_{bh} 37 GHz	4.71	3.16	4.46	2.90	7.39
Linear Dune ΔT_b 37 GHz	3.13	2.70	2.83	2.63	6.07
Transverse Dune T_{bv} 37 GHz	6.17	4.48	5.86	4.30	11.20
Transverse Dune T_{bh} 37 GHz	4.66	4.07	4.29	3.96	6.74
Transverse Dune ΔT_b 37 GHz	6.92	6.51	6.82	6.32	8.16

The model fit parameters are used to remove the t_d dependence of T_b and ΔT_b to retrieve the ϕ -modulation of the data shown in Fig. 5.7(d)-(f). The plots from the model and observations show similar results for both types of dunes. The comparison confirms that the presence of tilted facets modulates the radiometric temperature of the sand surface. Although the mean values of T_{bv} and T_{bh} for the model simulation are slightly different from the observations, the modulation characteristics are similar. In the case of ΔT_b , both the mean and the magnitude of the ϕ -modulation are consistent between the model and the observations. Figure 5.13 shows similar ϕ -modulation from observations at 37 GHz. The mean T_b and ΔT_b are lower than 19 GHz due to higher attenuation. Table 5.2 lists the Root Mean Square (RMS) errors of different model fits used. RMS error is the square root of the mean of the squared differences between the model and the observations. The additive (t_d , ϕ) second order harmonic model reduces the RMS error of fit compared to the individual second order harmonic fits for t_d and ϕ . The facet model of layered sand has higher RMS error than the observation model; however, all the models fit better to the ΔT_b . Given the uncertainties in the assumptions used in the facet model, it is remarkably accurate. The fits have

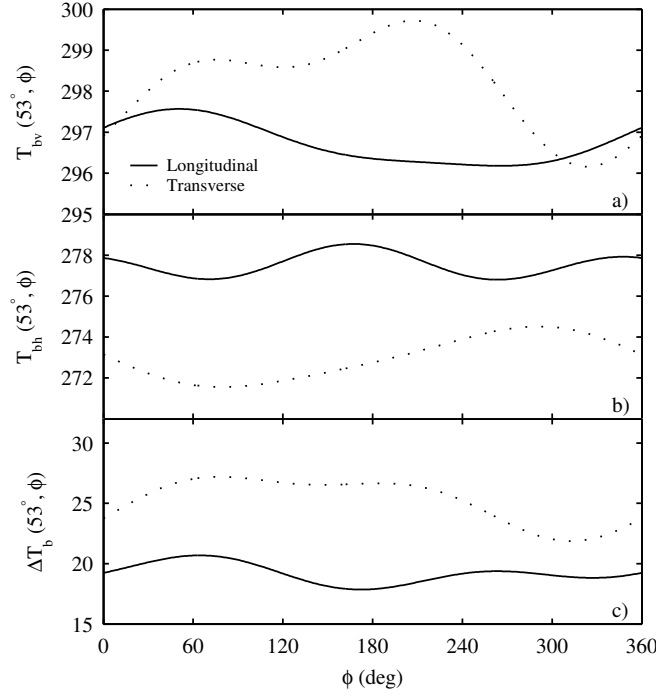


Figure 5.13: a)-c) simulated T_b and ΔT_b response over triple facet transverse and longitudinal dune models. d)-f) T_b and ΔT_b response derived from SSM/I and TMI observed data at 37 GHz.

higher error over transverse dune area due to higher surface profile variations than the longitudinal dune area. Moreover, the RMS error increases with frequency. The correlation coefficients between facet model and empirical observation model fit for T_{bv} , T_{bh} and ΔT_b of longitudinal dunes are 0.22, 0.79 and 0.95, respectively, and 0.60, 0.91 and 0.95, for transverse dunes.

The results reveal the dominant effect of surface geometry, and are similar to those found from model simulations. The simulated and observed ΔT_b reveal significant similarity in both magnitudes and phases. The difference in T_{bv} and T_{bh} between the model simulation and the observed data may be due to ignoring the sun inclination and because the subsurface temperature profile used does not represent the actual sand thermal conditions.

5.3 Summary

Radiometric emissions from erg surfaces are analyzed using SSM/I and TMI dual polarization T_b observations. Combining the data from the two sensors improves the azimuth angle sampling of the data and enable us to separate local time-of-day variation and ϕ -modulation. The observed T_b versus ϕ is modulated by the surface geometrical characteristics and reflects the presence of dominant dune facets. ΔT_b has negligible dependence on the thermal characteristics of the surface and its ϕ -modulation varies with changes in the surface geometrical characteristics.

A simple rough facet model is used to model the T_b response from the erg surface. Large scale dunes are treated as composed of dominant facets. An emission model based on fluctuating electromagnetic field theory for dissipative materials is used to estimate the T_b and ΔT_b incidence angle response for a flat sand surface. The total T_b from dunes is the weighted sum of T_b response from its dominant facets. When modeled as surfaces composed of multiple rough facets, longitudinal and transverse dunes exhibit significant differences in their T_b and ΔT_b ϕ -modulation: ΔT_b decreases whereas T_b increases due to a decrease in θ' . Thus, a tilted facet reveals its presence as a minimum in ΔT_b ϕ -response, where the magnitude of the ΔT_b reflects the tilt of the facet. The model simulation results are consistent with the satellite observations over areas of know dune types. Model simulation and satellite observations at 19 GHz and 37 GHz provide similar information about the dune shape and type.

TMI-acquired T_b observations at many times-of-day reveal the diurnal temperature cycle of the sand surface. The time-of-day dependence is removed by using a descriptive empirical observation model with two additive second order harmonics. Although there is significant T_b diurnal dependence, it is shown that T_b ϕ -modulation of 2-5K is observed as a result of surface geometrical characteristics. The ϕ -modulation of ΔT_b depends upon the tilts and orientation of the facets in the footprint of the sensor and can be used to distinguish between longitudinal and transverse dune surfaces. A logical extension of this result is to invert the proposed model to extract surface geometry from the T_b observations. The ϕ -modulation caused by

surface geometry is quite significant and needs to be taken into consideration when studying such surfaces or calibrating radiometers over such terrains.

The complementarity of passive and active remote sensing can be explored by combining microwave emission and scattering observations over sand surfaces. The analysis can be extended to other surfaces with periodic geometries such as snow for a better understanding of their radiometric emissions. The understanding of radiometric emissions over such surfaces can help in the design of future precision radiometers. It is noted that this research ignores the shadowing and sun illumination effects in explaining the radiometric behavior of sand.

Chapter 6

Microwave Study of Amazon Vegetation

In the previous three chapters, active and passive remote sensing of erg bedforms is addressed. Several empirical models are introduced to relate σ° and T_b to the surface geometrical characteristics in order to study spatial and temporal characteristics of Saharan ergs. This chapter extends some of these ideas to study of the σ° and T_b response over Amazon vegetation.

In Section 6.1, σ° incidence angle dependence over vegetation cover is discussed. The multi-frequency signatures of both σ° and T_b are studied in Section 6.2. Section 6.3 provides results of spatial inhomogeneity model applied to σ° and T_b data. C-band and Ku-band σ° from various scatterometers over the Amazon basin for selected study regions are presented in Section 6.4. Multi-annual temporal variability of the Amazon basin is studied using C-band ERS data and a Ku-band time series formed by SASS, NSCAT and QSCAT data. A summary is presented in Section 6.5. Some of this work has been published in [7, 8]. This material is in preparation for submission to *IEEE Transactions on Geoscience and Remote Sensing*.

6.1 σ° Incidence Angle Dependence of Vegetation

Backscattering from vegetation depends on vegetation density, which is a function of leaf size and density, moisture content, trunk and branch density, and vegetation thickness. σ° of the Amazon rain forest includes contributions from vegetation (primarily volume scattering) and the surface beneath vegetation (surface scattering). The surface scattering contribution decreases with increasing vegetation density.

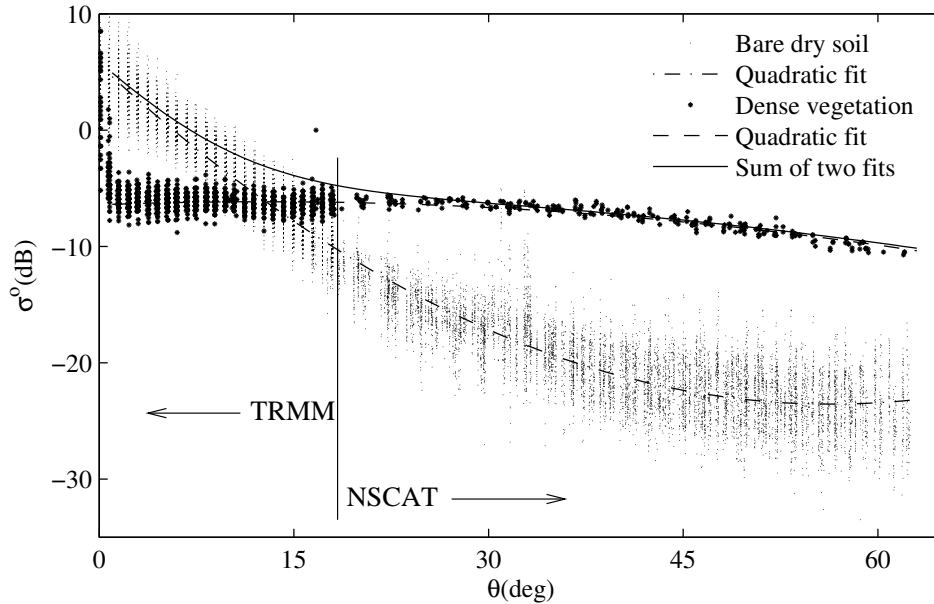


Figure 6.1: σ° θ response from bare dry soil and dense vegetation.

For tropical vegetation, σ° versus θ relationship is significantly dependent on the vegetation density. Fig. 6.1 compares the Ku-band σ° versus θ variation (using TRMM-PR and NSCAT V-pol data) over bare dry soil and dense vegetation. Bare soil σ° is due to surface scattering. The high near-nadir σ° for bare soil is mainly due to specular reflection from the surface. σ° decreases quadratically at increased θ . This surface scattering response increases with moisture content. In the case of flooding, the response at nadir increases but reduces at off-nadir angles due to specular reflections away from the backscattering direction. The dense vegetation curve is much flatter since the dominant scattering mechanism at off-nadir angles is volume scattering. The near-nadir response has a narrow specular reflection component but nearly constant at off-nadir angles. The σ° versus θ response of dense vegetation for off-nadir angles can also be modeled with a quadratic fit.

The solid line in Fig. 6.1 is the sum of σ° versus θ quadratic fits of bare soil and dense vegetation and is a representative of an area with both large surface

and large volume scattering components. It should be noted that at low θ the surface scattering has more contribution, whereas at high θ the volume scattering dominates.

Figure 6.2 shows the σ° variation with θ from all the active instruments for three different land cover types. The data covers October of the year 1978, 1996 and 1999 for SASS, NSCAT, and the remaining sensors, respectively. The three plots differ due to the different contributions from surface and volume scattering over the three land cover types as previously noted. The two contributions are related to the density of the vegetation cover. In the dense forest, most of the incident wave energy is scattered by the leaves of the forest canopy and very little energy reaches the underlying soil; thus, the scattering is dominated by volume scattering from the canopy. This is clear in Fig. 6.2(a) where there is negligible evidence of surface scattering at low incidence angles. The grasslands vegetation stand has the lowest vegetation density. In this region, the incident wave penetrates to the underlying surface. The greater surface scattering from grasslands results in steeper σ° versus θ at low incidence angles compared to the dense forest evident from Fig. 6.2(c). It should be noted that the ESCAT C-band σ° is lower than that from Ku-band. This is due to the larger wavelength of the C-band which results in greater penetration and attenuation. Moreover, the Ku-band wavelength is of the order of most plant-leaf-sizes resulting in greater volume scattering from the rain forest. The difference is more evident at low incidence angles and higher vegetation densities. Figure 6.2 also reveals that C-band σ° versus θ has shallower slope than Ku-band and the offset between the two slopes reduces with the vegetation density.

The three Ku-band sensors, although separated in time, provide consistent behavior. H-pol σ° is generally higher than V-pol. The high variability of QSCAT data is predominantly due to noise. TRMM-PR σ° measurements also have high noise and small footprint. It should be noted that diurnal variation of the Amazon vegetation increases the variability in the σ° measurements which may be taken at different local times-of-day.

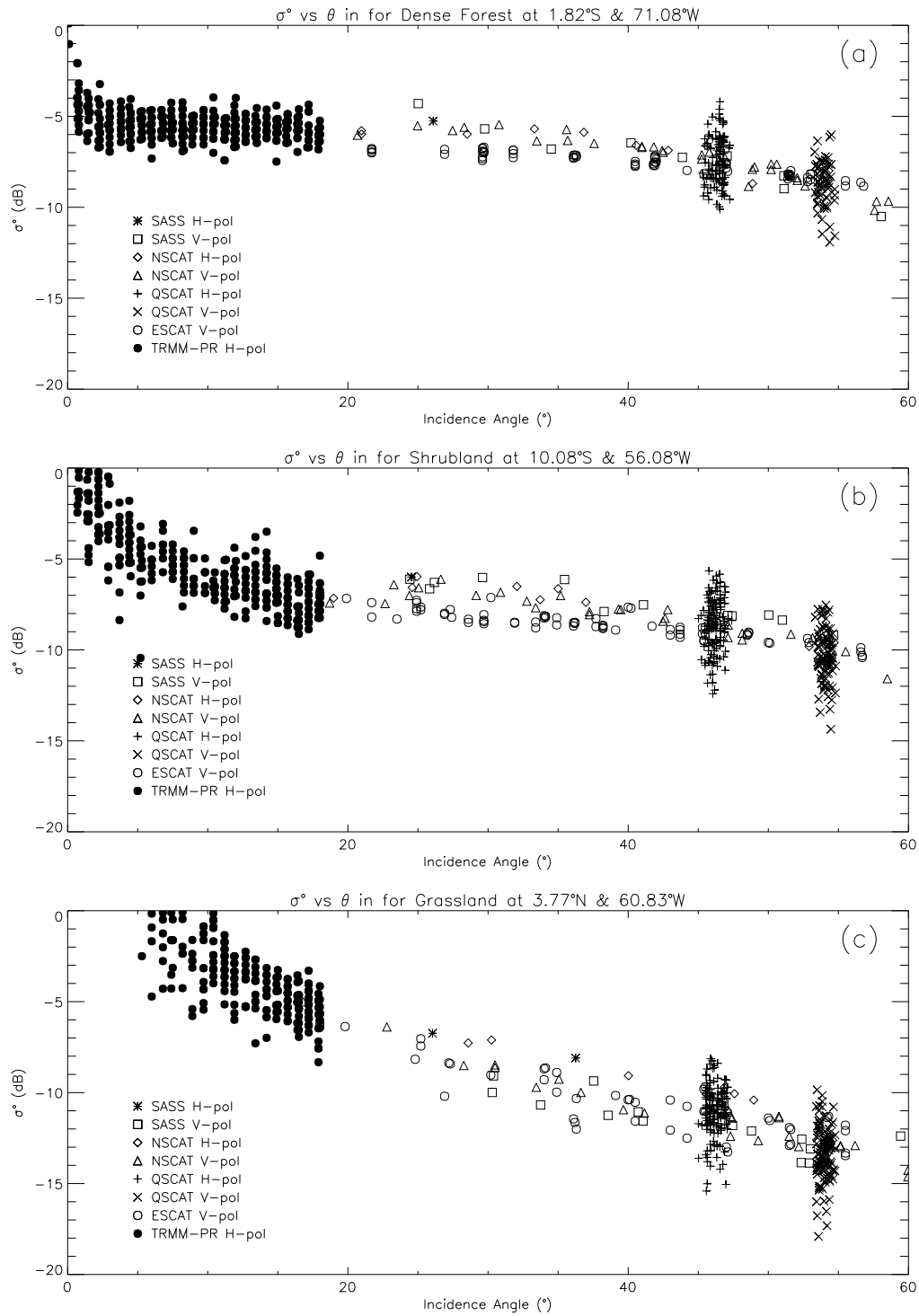


Figure 6.2: Plots showing multi-spectral σ^0 variation with incidence angle using SASS, ESCAT, NSCAT, QSCAT and TRMM-PR data over selected (a) dense forest, (b) shrub land and (c) grassland. Due to the selected σ^0 axis range, the positive TRMM σ^0 values at low incidence angles are clipped.

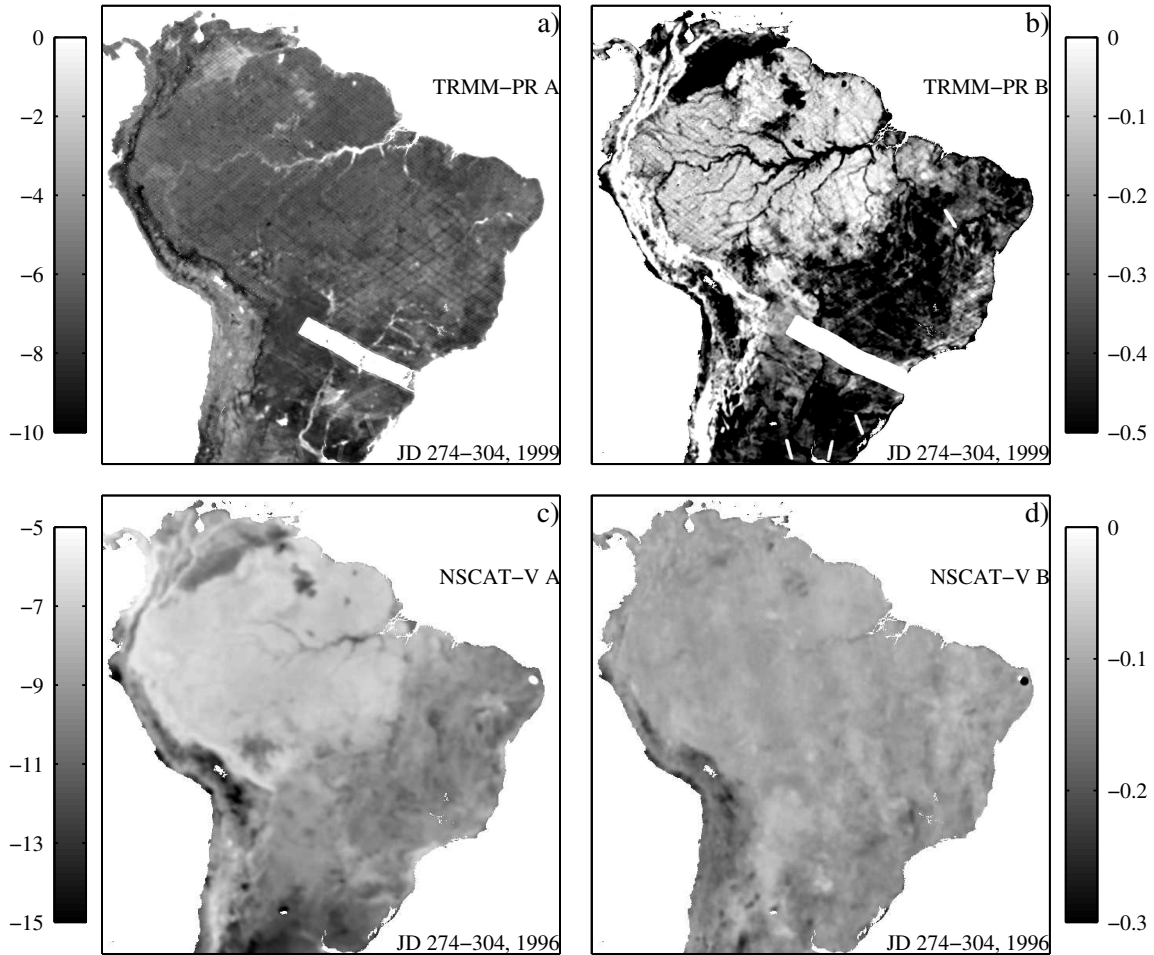


Figure 6.3: A and B images of Amazon computed from TRMM-PR and NSCAT σ° measurements. The strip in TRMM-PR images is caused by bad data measurements.

The linear σ° versus θ model given in Eq. 2.6 [repeated here for convenience $\sigma^\circ(\theta) = A + B(\theta - \theta_{ref})$] has been used extensively to distinguish different land cover types. This model is often used over a narrow range of incidence angles since the overall relation is nonlinear. Even with this restriction, the model is useful in vegetation studies. For example, Fig. 6.3 shows images of the model parameters over Amazon basin computed from TRMM-PR and NSCAT with θ_{ref} of 3° and 40° , respectively. TRMM-PR B provides a better discrimination of vegetation density than NSCAT B due to greater contribution of surface scattering. The grasslands appear as dark pixels in the TRMM-PR B image, whereas dense vegetation pixels

are brighter. The Amazon basin river network appears as dark pixels in TRMM-PR B image whereas the NSCAT B image does not provide much information about this feature. It is noted at this point that TRMM-PR σ° measurements are acquired at a higher spatial resolution than NSCAT, which also plays a significant role in better discrimination of river network. NSCAT A value reduces with vegetation density. σ° versus θ response as a function of vegetation density and surface flooding can be exploited to support vegetation classification and temporal change studies of Amazon basin.

6.2 Multi-Spectral σ° and T_b Signatures

The radiometric emission from vegetation depends upon emissivity and physical temperature. Analogous to σ° , T_b measurements include contributions from both surface and volume emissions. Surface emission is attenuated and scattered by vegetation canopy and so its contribution reduces with increasing vegetation density.

σ° and T_b measurements depend upon the frequency of measurement. Multi-spectral σ° and T_b measurements can be fused to improve vegetation classification of vegetation. The V-pol C-band (ESCAT) and Ku-band (NSCAT) σ° , and V-pol T_b (SSM/I) are used to plot the frequency response of different land cover types in Fig. 6.4. Fig. 6.4(a) plots the σ° and T_b over the dense vegetation, showing the data points and a line through the mean value at each frequency. The C-band and Ku-band data are normalized to 53° to make the incidence angle comparable to the SSM/I data. The active and passive channel regions are indicated.

σ° increases with frequency due to greater scattering at reduced wavelengths. The difference in σ° between two frequencies is almost equal for all vegetation types at high incidence angles. The difference varies with vegetation types for midrange incidence angles as seen in Fig. 6.2.

The atmosphere has negligible effect on σ° measurements except under heavy rain conditions. SSM/I was initially designed to study the atmosphere; thus, its measurements have significant atmospheric dependence, introducing noise to land

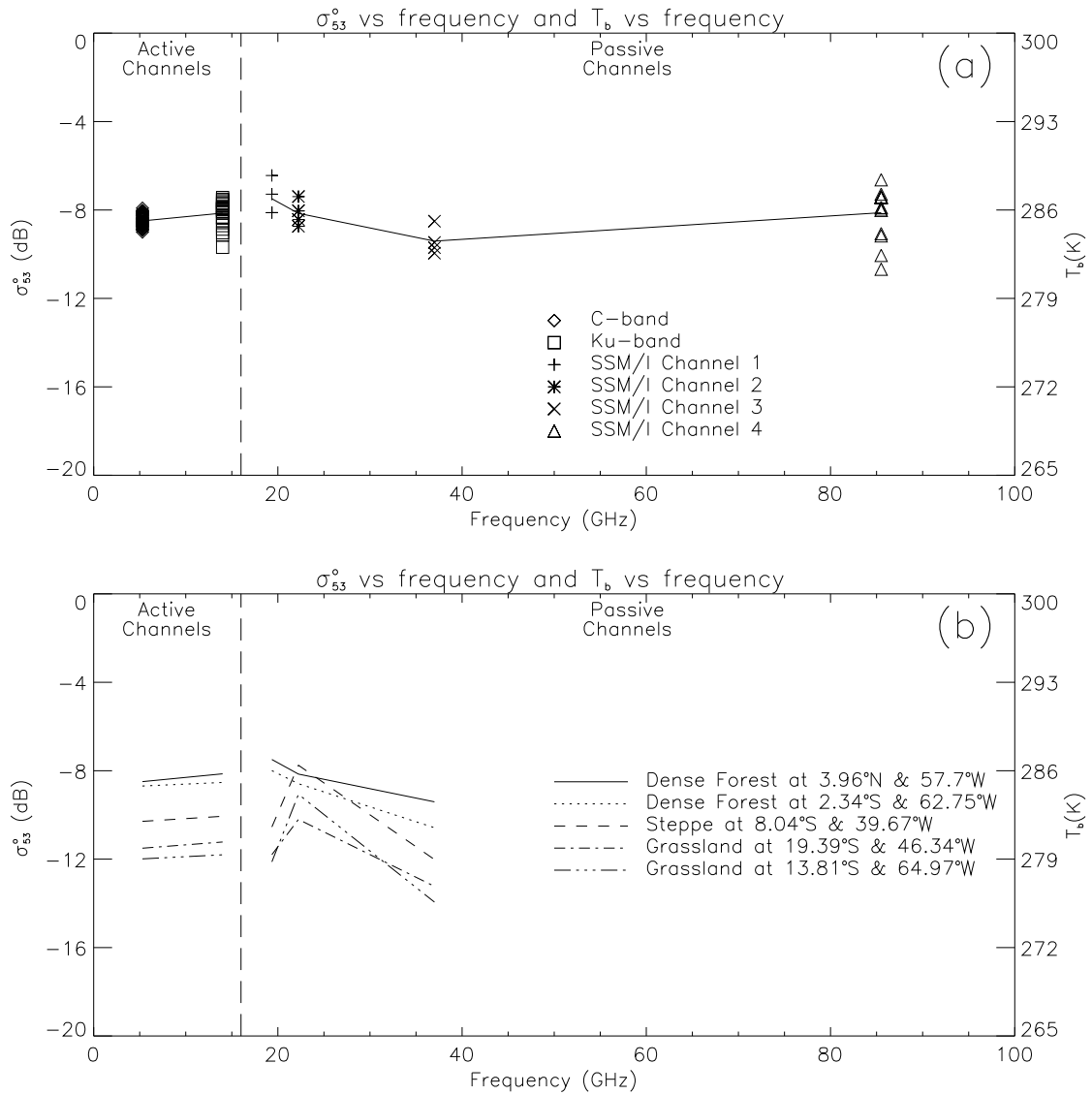


Figure 6.4: Multi-spectral V-pol σ^0 and T_b variation from scatterometers and radiometer, respectively over (a) dense forest and (b) different land cover types.

T_b data. Nevertheless, observations indicate that T_b measurements provide discrimination between various land targets.

In Fig. 6.4(a), T_b decreases with increasing frequency with an exception at 85 GHz. The deviation results from increased atmospheric emissions at 85 GHz. These emissions contaminate the vegetation signal. Fig. 6.4(b) shows similar plots for different vegetation types, with only the line fit shown for clarity. The T_b values at 85 GHz are discarded due to their atmospheric contamination. T_b depends upon the emissivities and thermal characteristics of vegetation and underlying soil. Over dense vegetation most of the emission contribution is from the canopy and T_b is seen to decrease with frequency. With reduction in vegetation density, the contribution from the underlying soil increases. The soil is typically at a lower physical temperature. Thus, T_b reduces with a reduction in vegetation density. Different land cover types exhibit unique frequency responses. Both the σ° and T_b lines lower with reduction in the vegetation density and a distinct inversion of slope for the first two SSM/I channels can be observed. This inversion from negative to positive slope occurs as the vegetation density reduces.

The dense forest T_b value is predominantly due to the emissions from forest canopy whereas over grassland, the soil emissions also contribute. The plot reveals that the soil contribution increases with a decrease in vegetation density.

6.3 Spatial Inhomogeneity Model

The spatial variability in σ° and T_b measurements of the Amazon results from spatially varying vegetation density and moisture content. In this section, the spatial inhomogeneity model from Chapter 4 is applied to σ° and T_b measurements over Amazon basin. In this application the model for σ° versus θ is modified to

$$\sigma^\circ(\theta, r, \beta) = A + B(\theta - \theta_{ref}) + h(r, \beta) \quad (6.1)$$

while T_b measurements from SSM/I are modeled as

$$T_b(r, \beta) = T_{bm} + h(r, \beta) \quad (6.2)$$

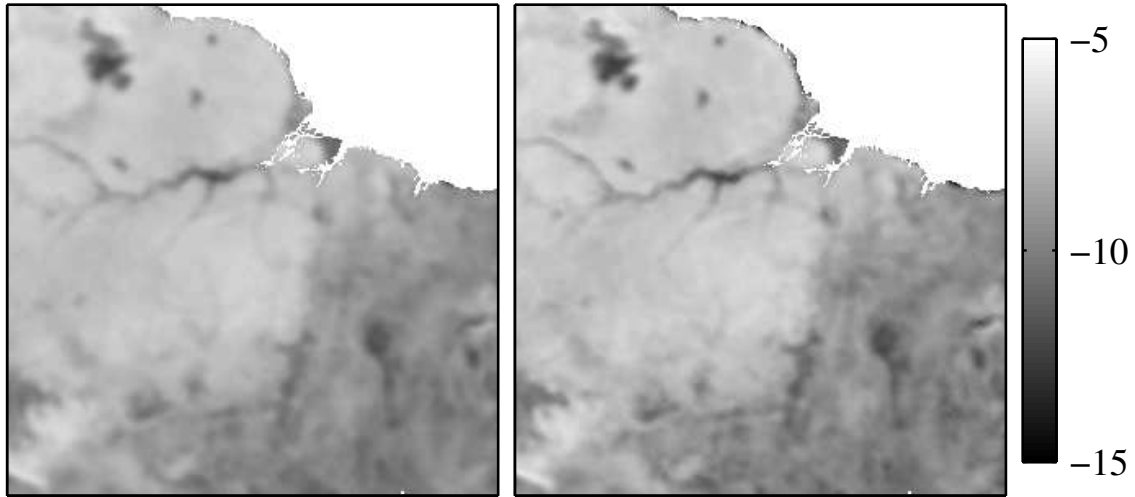


Figure 6.5: A sub-region of Amazon basin comparing A values a) without and b) with spatial inhomogeneity model.

where $h(r, \beta)$ is defined in Eq. 4.4. σ° and T_b measurements within 30 km of the point of interest are used to evaluate the model parameters. Moreover, since σ° and T_b are dependent on the time-of-day of measurement, model is applied separately to ascending and descending pass data.

Fig. 6.5 compares the estimated model A values over a small sub-region on Amazon basin, before and after incorporation of spatial inhomogeneity model. In general, the A values from two models look similar but there exist subtle areas with improved contrast when the spatial inhomogeneity model is included. This improvement in contrast of Fig. 6.5(b) reflects the variations in vegetation density not depicted in Fig. 6.5(a). Thus, incorporating the spatial model improves the utility of the data.

The new model also provides parameters that measure the spatial inhomogeneity of σ° and T_b measurements. Fig. 6.6 shows the magnitudes and phases of first order (plane) and second order (hyperbolic paraboloid) inhomogeneities over all of Amazon region. Model parameters from NSCAT σ° and SSM/I T_b model fit

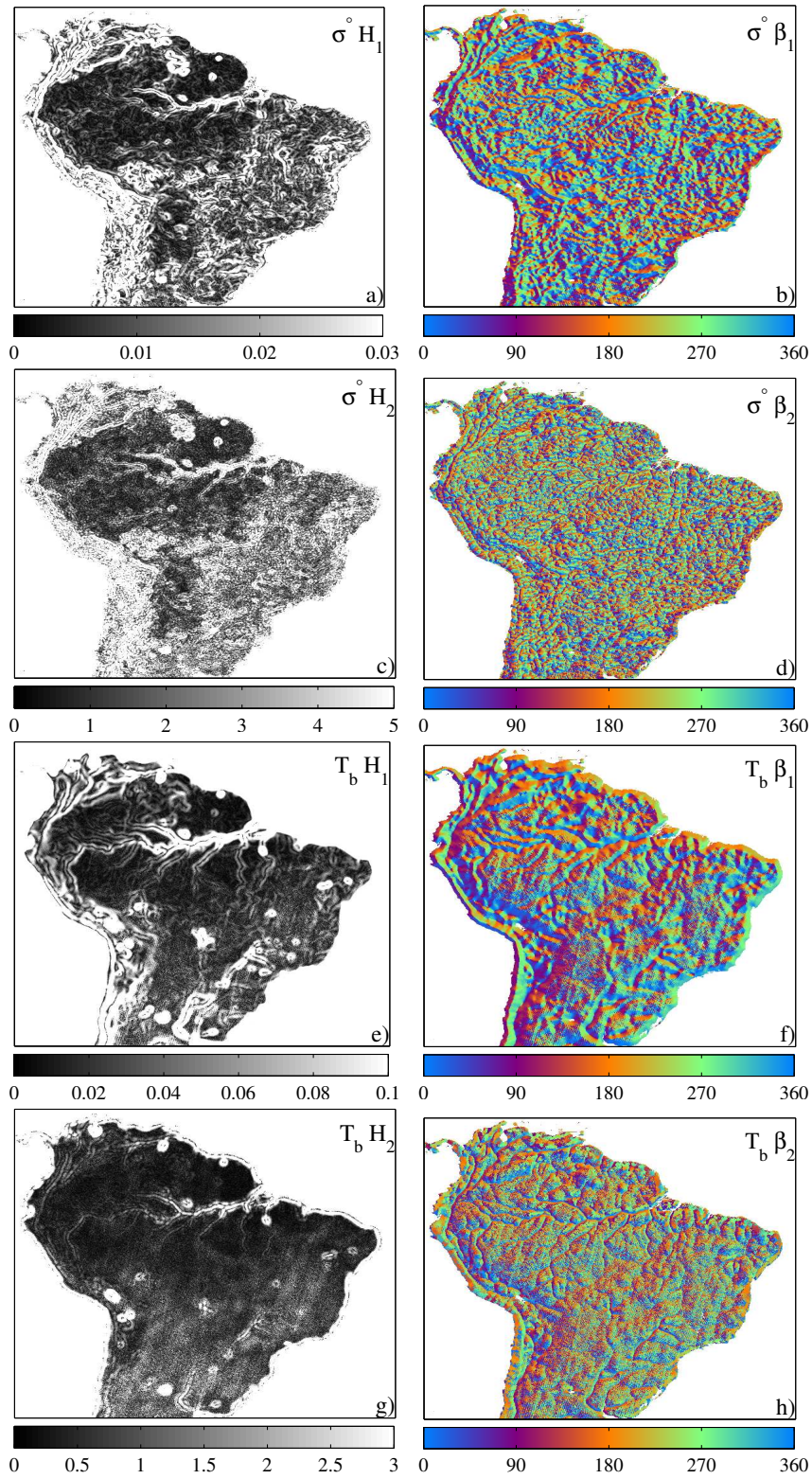


Figure 6.6: Images of spatial inhomogeneity parameters computed from V-pol NSCAT σ° measurements during JD 274-305, 1996 and SSM/I 19 GHz V-pol T_b measurements during JD 274-305, 1999

are shown. The H_1 images of σ° and T_b model reveal strong signatures of river network and Andes mountain range in the west of the Amazon basin. The boundaries of lakes in the south of the Amazon basin are also evident.

The H_1 and H_2 values in dense forest are low, confirming the spatial homogeneity. However, the boundaries appear as bright lines due to transitions between different vegetation types. The direction β_1 is consistent with the geographical variations. The river network, mountain range and transition from dense forest to Savannah grasslands are all evident. β_2 is similar to β_1 but noisier. It should be noted, that despite low values of magnitudes H_1 in the dense forest, β_1 provides small iso-phase patches which could represent different subclasses of dense vegetation. Alternately, this could be due to spatial variations of moisture content within the dense forest. Although the spatial inhomogeneity signal is low, its spatial consistency to geographical features suggests that these low spatial variations in σ° and T_b measurements can provide useful information about vegetation spatial characteristics.

Fig. 6.7 presents A and T_{bm} images of the Amazon area at various frequencies and polarizations. Generally, Ku-band has higher backscatter than C-band as observed in σ° versus θ response over selected vegetation types. The Ku-band image has more detail resulting from the higher resolution of NSCAT. Moreover, it provides more detail about the spatial variation of dense forest not seen in C-band image. In dense forest, Ku-band has greater volume scattering component than C-band. On the contrary, C-band has a greater surface scattering component than Ku-band in the Savannah grasslands. This is evident from more spatial details of grasslands in C-band image. These differences between A of dense vegetation and grasslands are caused by higher attenuation of Ku-band and higher penetration depth of C-band as a function of vegetation density. This is evident in the difference images shown in Fig. 6.8. The difference is also a function of time-of-day due to diurnal variations of the moisture content. In the morning, dew on the plant leaves increases the moisture, thus increasing the A values. As the day progresses, evaporation results in reduction of backscatter. This effect is believed to be the strongest in the rain forest.

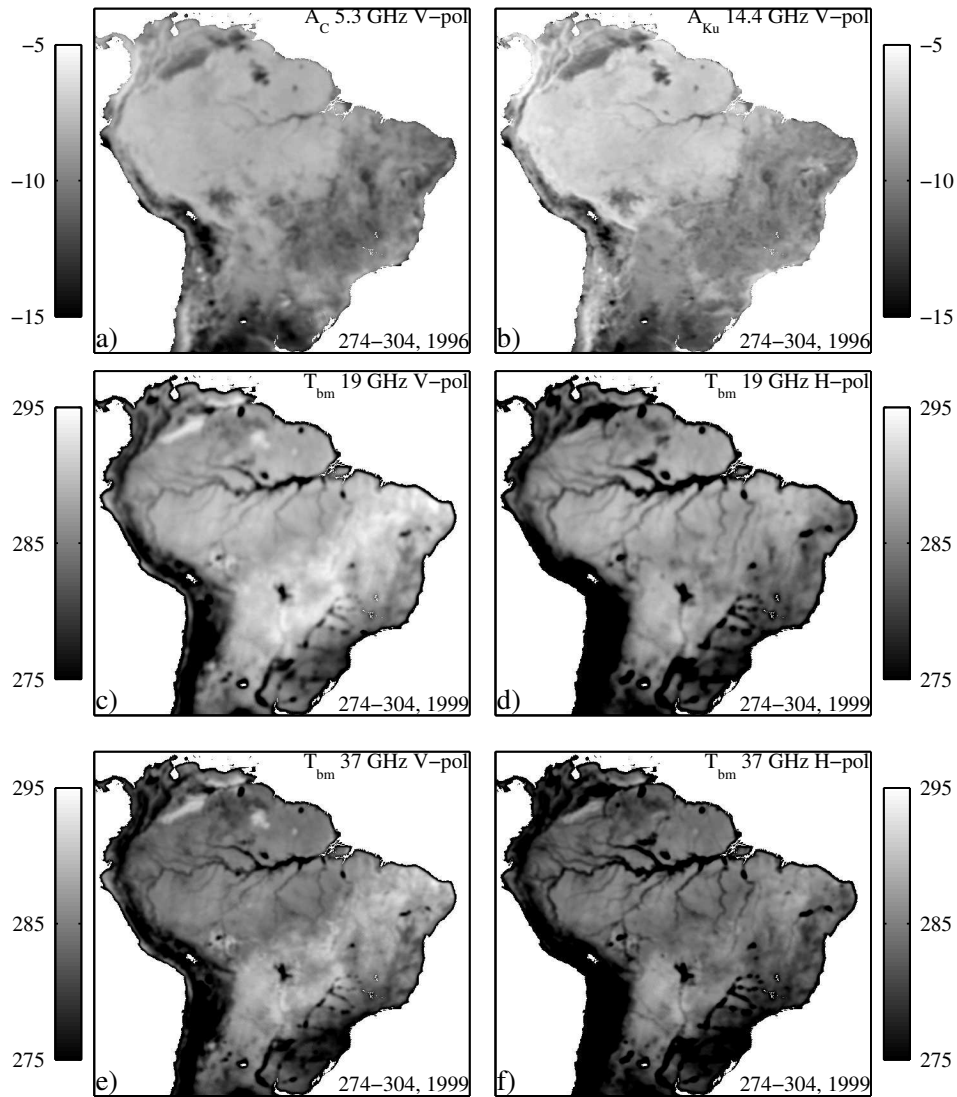


Figure 6.7: Multi-spectral ascending pass σ° and T_b images of Amazon basin. a) C-band A image computed from ESCAT. b) Ku-band A image computed from NSCAT. c) and d) V-pol and H-pol T_{bm} at 19 GHz, respectively. e) and f) V-pol and H-pol T_{bm} at 37 GHz, respectively.

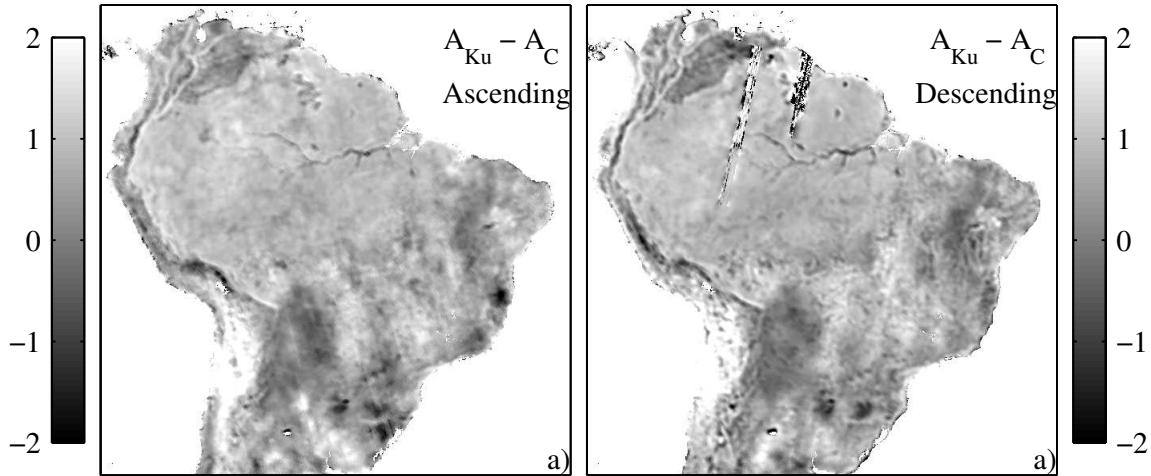


Figure 6.8: Difference of Ku- and C-band A values from a) ascending pass and b) descending pass. Noise in the north of the Amazon is due to insufficient C-band σ° measurement.

Fig. 6.7 also provides dual polarization T_{bm} images at 19 and 37 GHz. In general, H-pol T_b is lower than V-pol. The V-pol T_b of grasslands is higher than dense forest whereas H-pol T_b of some grasslands is lower dense vegetation. These differences result from relative contributions of volume and surface emission as a function of vegetation density. Moreover, the different transmission characteristics of H- and V-pol emissions also contribute to these differences. Unlike dense vegetation, grass stand is mostly vertical which also results in different H- and V-pol contributions in the two vegetation types. These differences are consistent for both 19 and 37 GHz: the 19 GHz T_b is higher than 37 GHz. H-pol provides more information about the river network.

This leads to the conclusion that the multi-spectral analysis of Amazon basin using the model of spatial inhomogeneity provide new parameters to analyze vegetation characteristics. These parameters can be exploited to support vegetation classification and global change studies.

6.4 Time Series Analysis

ESCAT aboard ERS 1/2 has been acquiring C-band radar backscatter measurements over land since 1992. SASS, NSCAT and QSCAT in combination also provide sparse but long time series of Ku-band σ° data. These data sets are used to study multi-annual temporal characteristics of Amazon vegetation. Figure 6.9(a) shows the backscatter time series of three sites at 71°W 1°S, 62°W 8°S and 59°W 14°S in the Amazon basin. The three sites are representatives of dense vegetation from central Amazon rain forest, brush land, and Savannah, respectively. The backscatter measurements from vegetation depend upon both surface and volume scattering phenomenon. An increase in the vegetation density results in increased contribution from volume scattering. The σ° measurements from dense forest are found to be as high as -7.5 dB, with negligible seasonal variations.

The brush land response shows a backscatter of -8 dB with increased seasonal variations. Savannah grasslands present lowest backscatter of all the vegetated areas. The σ° is -11 to -9 dB and is highly dependent upon the time of the year. This increased dependence upon the seasonal changes results from the high contribution from the surface scattering, which is predominantly governed by soil moisture conditions. The dependence on annual rains is evident which occur in the winter.

The σ° temporal behavior of the dense forest and brush land shows a general decrease between 1992 and 1999. A similar trend is observed for various other sites. Though this potentially indicates a reduction in the vegetation density, it could be due to long-term instrument drift.

Surface and volume scattering from different vegetation types is also dependent upon the incident frequency. Variable sensitivity of C-band and Ku-band microwaves to different vegetation type enables us to explore the multi-spectral signatures of Amazon rain forest. Figure 6.9(b)-(c) plot the σ° measurements from the overlap time period of ESCAT and NSCAT over the dense vegetation and Savannah grasslands, respectively. C-band radar backscatter measurements are lower than the Ku-band H- and V-pol measurements. Despite the general consistency between the two data types, subtle difference are seen that are dependent upon season.

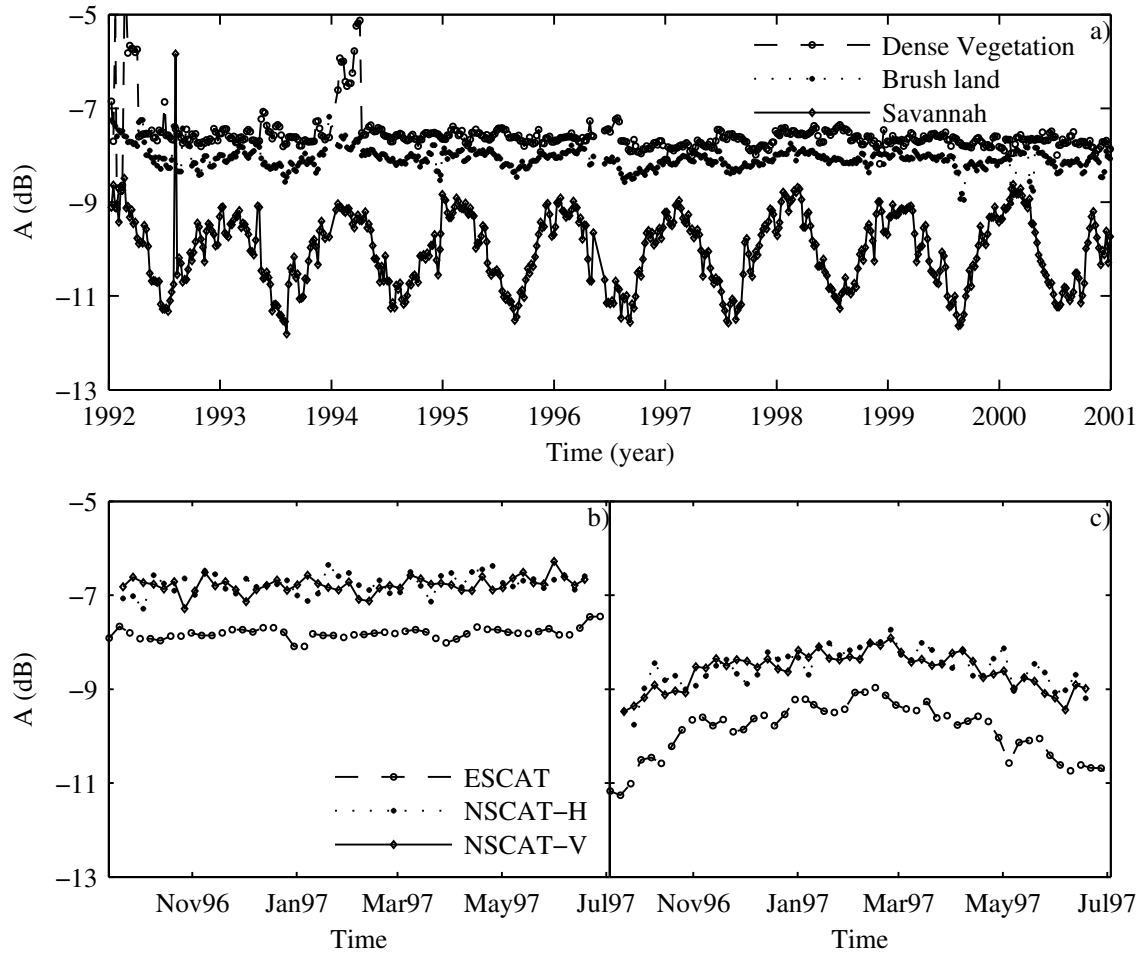


Figure 6.9: a) ESCAT σ° time series for three vegetation types. b) ESCAT and NSCAT dual-pol σ° time series at 71°W 1°S . c) ESCAT and NSCAT dual-pol σ° time series at 59°W 14°S

Data from QSCAT is compared with data from the previous Ku-band scatterometer missions. Figure 6.10 shows images of A from three sensors. These images are from SASS (JD 258-281, 1978), NSCAT (JD 259-270, 1996) and QSCAT (JD 269-272, 1999 and JD 257-260, 2000). The QSCAT images are at an incidence angle of 54° rather than 40° as for SASS and NSCAT. Beside the general similarity in the four images, some subtle differences are evident. NSCAT and QSCAT images show a small low backscatter patch at 60°W 2°S that is not present in the SASS image. Moreover, QSCAT image presents some additional distributed low backscatter

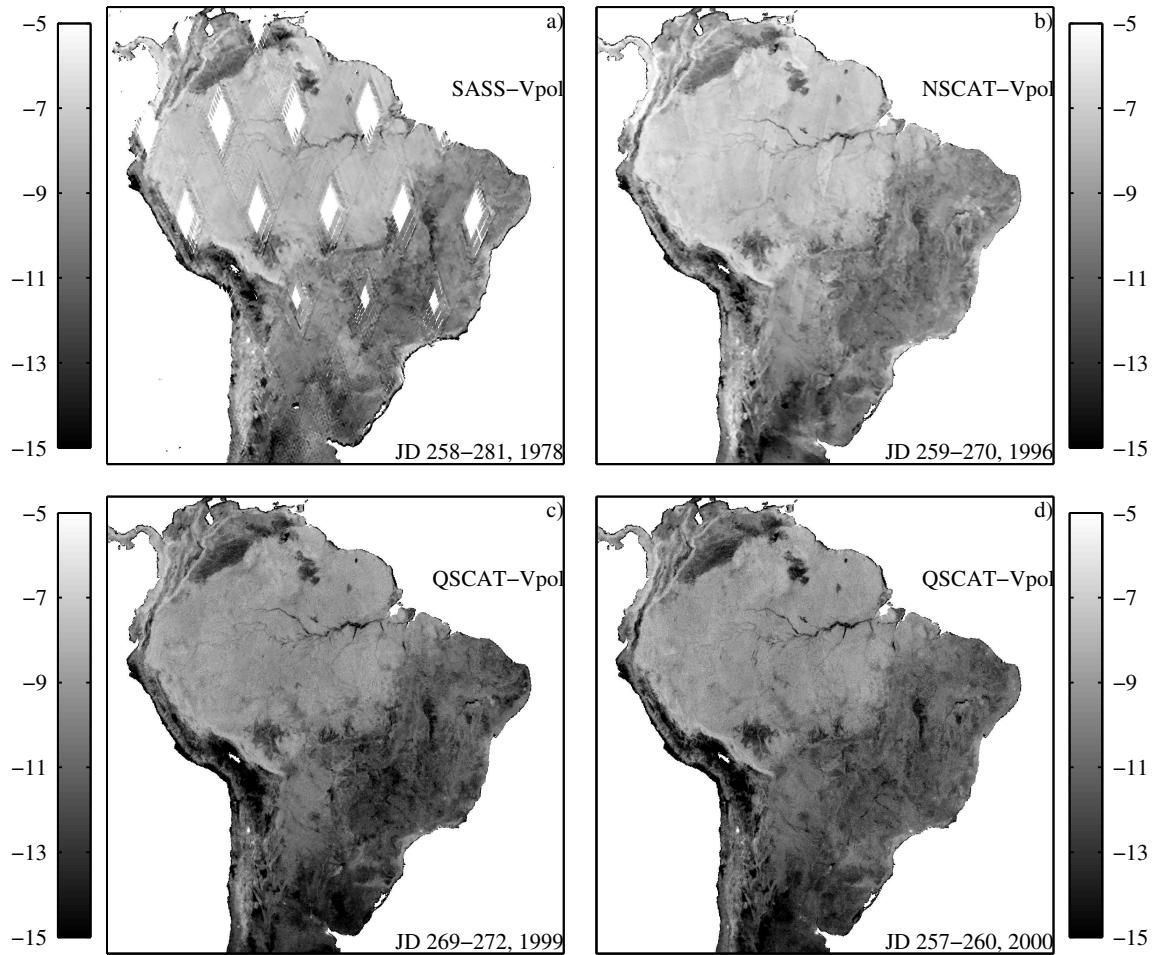


Figure 6.10: Comparison of σ° measurements from SASS (JD 258-281, 1978), NSCAT (JD 259-270, 1996) and QSCAT (JD 269-272, 1999 and JD 257-260, 2000). The SASS and NSCAT images are of σ° at 40° while QSCAT images are σ° at 54° .

patches, which are not seen in either NSCAT or SASS images. Most of these areas are surrounded by dense vegetation areas. The change is identified by analyzing the time series σ° from C- and Ku-band instruments. ESCAT and combined SASS, NSCAT and QSCAT data provide a long C- and Ku-band σ° time series. Figure 6.11 (a) and (b) show time series plots of A and B from dense forest and its boundary, respectively. The A and B values are calculated using Eq. 2.6 where the normalization is made to 54° incidence angle to match with QSCAT data. The normalized A values do not exactly match the QSCAT A measurements, due to a bias from approximating

σ° versus θ by a straight line. The bias is minimum at mid-incidence angles and increases at near and far ranges.

The A time series from the dense forest [Fig. 6.11(a)] has a very stable backscatter for both the frequencies during the last two decades. The B plot is noisier and has a positive step in the C-band during 1996. The ESCAT was switched from ERS-1 to ERS-2 in this year. Since Ku-band does not show any significant change in the mean B value between 1978 and 1996, the step in the ESCAT data is probably attributed to calibration differences of the two ERS scatterometers. The B plot from forest boundary [Fig. 6.11(b)] also shows a similar step but is less evident due to seasonal variations. This latter plot corresponds to an area suspected to have undergone deforestation. The C-band A plot reveals a gradual increase in the amplitude of the seasonal fluctuation over the decade whereas the yearly mean of A is found to decay with time. This effect is more significant after 1996 and can also be seen in the Ku-band data. Although this could be due to the ESCAT data quality, a similar trend at Ku-band suggests that the primary cause is geophysical variation, possibly a reduction in canopy density. The solid line is a fit to the ESCAT time series and its equation is also shown. The line has a slope of -0.0005 dB/day with a decrease of about 1.8 dB in the mean A over eight years. A similar trend is observed at many other locations on forest boundary.

The time series of ESCAT A over the whole Amazon basin is fit with a straight line. Figure 6.12(a) is the map of the slope of the line fit at each pixel. The diamond shaped artifacts are the noise from using multiple swaths at different local times-of-day. The slope value in the dense forest area is close to zero, confirming its temporal stability. In the southern region, dark patches have low slope values and indicate areas where the decrease in A is significant. This must be related to geophysical changes in the area such as reduced moisture and/or vegetation density. The location of these areas at the fringes of the forest suggests that they are possibly the areas of reduced canopy cover. Most of these areas are found to have slope smaller than -0.0015 dB/day. The slope map is thresholded at this value and overlaid onto the QSCAT V-pol A image shown in 6.12(b). The overlaid patches are the areas

of possible deforestation. There are a few areas of positive slope, possibly due to increasing vegetation density.

6.5 Summary

A simple multi-spectral analysis of the Amazon basin is conducted. Scatterometers and TRMM-PR σ° variations with incidence angle show distinctive behavior for different vegetation densities. The different sensors are generally well inter-calibrated.

Different land cover types exhibit unique frequency responses of σ° and T_b . The incorporation of the spatial inhomogeneity model into the σ° and T_b imaging models improves the parameter image quality. The new model parameters provide additional information about spatial geophysical characteristics of Amazon basin.

Ku- and C-band σ° depend upon the vegetation density and observation time-of-day. The σ° difference of the two frequencies is a function of vegetation density and provides a new discrimination based on of dual frequency comparative surface and volume scattering contributions.

Results from the temporal analysis of Amazon basin are presented. C-band and Ku-band σ° measurements are found to be generally consistent. The long-term time series of ESCAT σ° indicates a general decrease in backscatter for all areas studied. This may be due to a long term instrument drift or it could represent a long term change in the study areas. Data from all Ku-band sensors (SASS, NSCAT and QSCAT) is compared and found to exhibit small differences at various sites distributed in the Amazon rain forest due to long-term change and resolution difference.

The C- and Ku-band time series reveal a small calibration mismatch between ESCATs aboard ERS-1 and ERS-2 satellites. A gradual decrease in ESCAT A is fit with a straight line and its slope is used to identify areas of significant A reduction possibly caused by geophysical changes. Low-slope regions are found, mostly at the southern boundary of the Amazon forest, which could be due to deforestation.

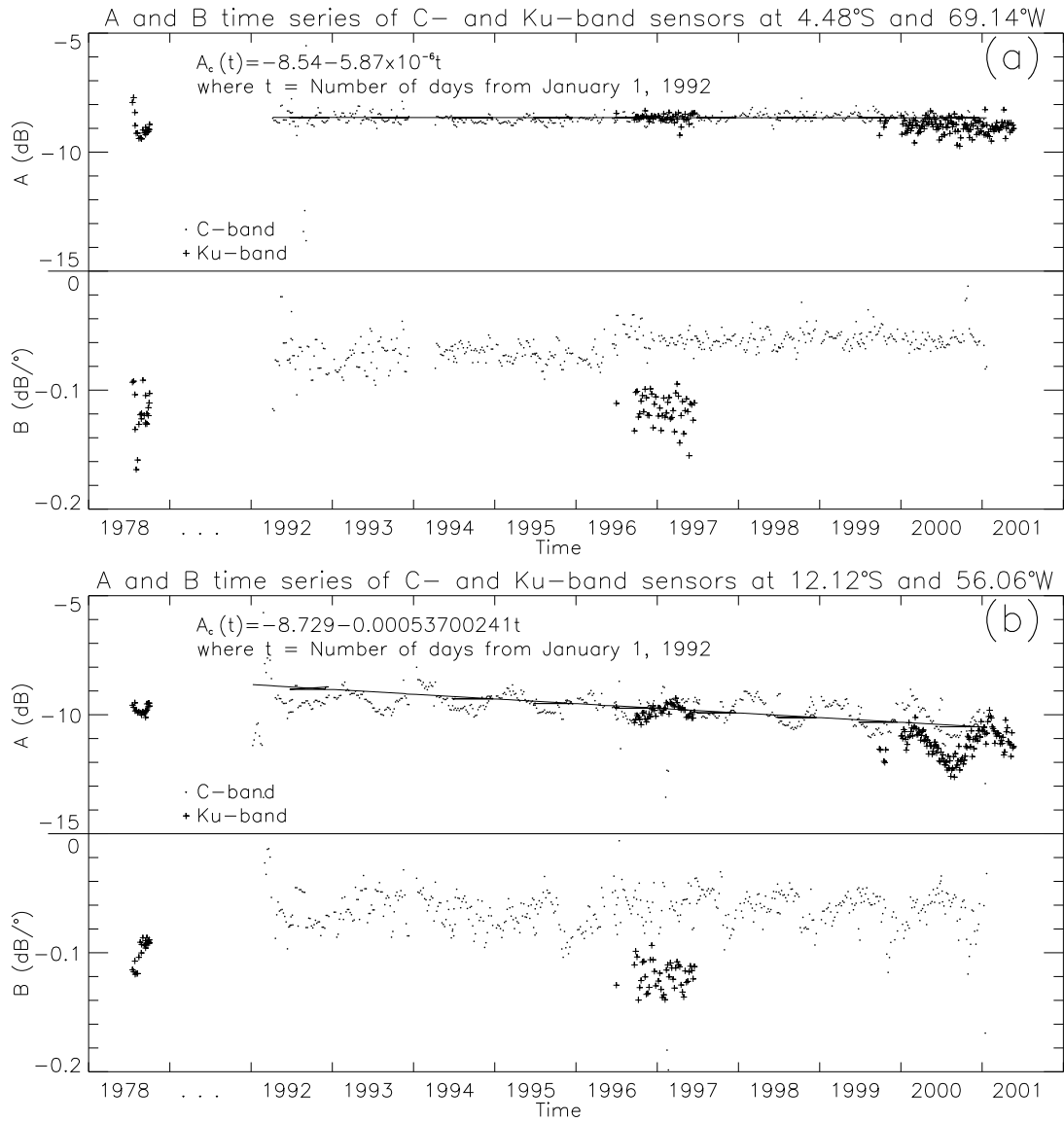
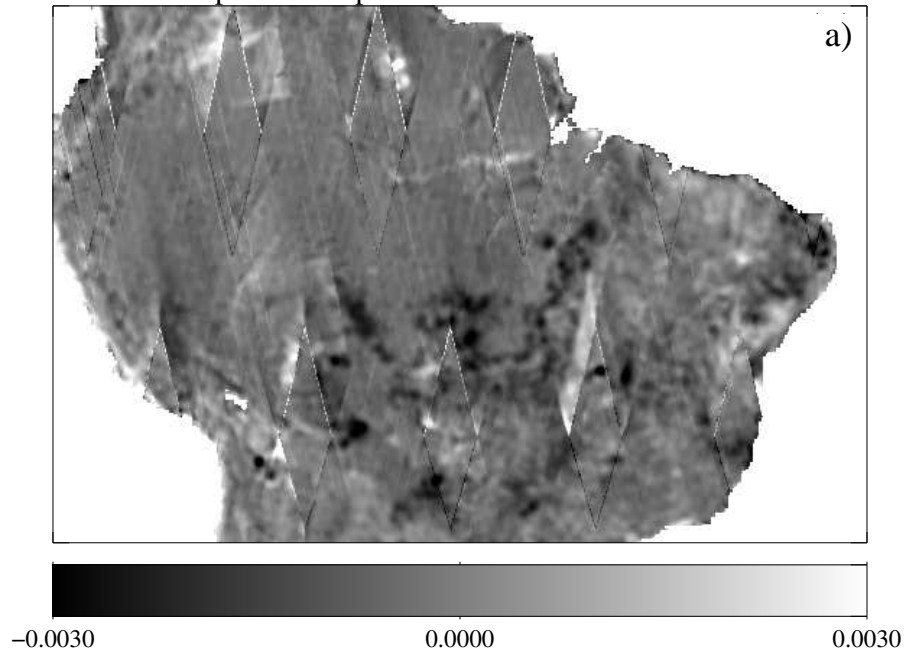


Figure 6.11: Time Series of A and B values from C- and Ku-band data over the (a) dense forest and (b) fringes of the dense forest.

Map of the slope of the ESCAT A time series



QSCAT V-pol A Image overlaid with areas where slope < -0.0015

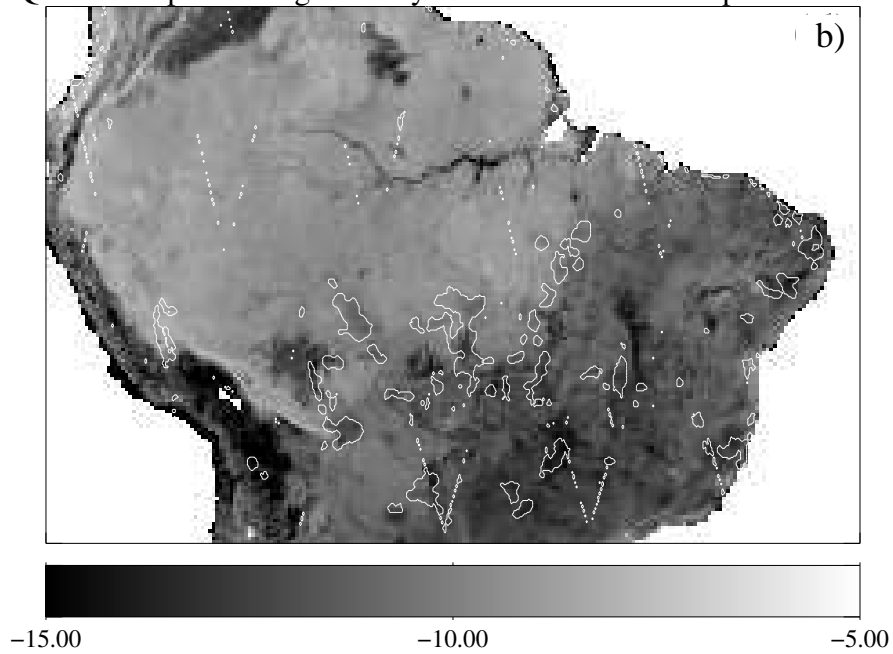


Figure 6.12: (a) shows the slope the ESCAT A decade long time series over Amazon basin and (b) is QSCAT V-pol image. The overlaid contours correspond to the areas where ESCAT time series slope is less than -0.0015

Chapter 7

Conclusions and Recommendations

In this dissertation, sand bedforms and vegetation are studied using space-borne microwave remote sensing. Active and passive microwave remote sensing data are modeled to extract useful surface characteristics that provide insight into geophysical processes of Saharan ergs and Amazon vegetation. Section 7.1 summarizes key results achieved from this research. The conclusions of this dissertation identify new areas of research for continuation and advancement of this study. Section 7.2 provides a list of recommendations that may help in extensions and applications of this research.

7.1 Results

My research into microwave scattering and emission from ergs and vegetation has resulted in several key observations related to σ° and T_b behavior of such land surfaces. These key observations include the effects of spatial and temporal variations of surface geophysical characteristics on σ° and T_b variations with measurement observation geometry; the inference of the factors governing variations of geophysical characteristics; and an analysis of the consistency, quality, and fusibility of data from multiple microwave instruments.

7.1.1 Radar Backscatter Directional Modulation from Erg Surfaces

σ° directional modulation is studied and related to the surface geometrical characteristics. The electromagnetic scattering from erg surfaces is modeled as composed of scattering from large- and small-scale sand bedform features.

Large-scale dunes are modeled as composed of tilted rough facets. The total scattering from dunes is the sum of scattering from all of the rough facets in the footprint weighted by the fraction of their area in the footprint. Longitudinal and transverse dune fields are modeled as composed of rough facets. The proposed rough facet model is applied to the modeled dune fields. The results indicate a strong signature of the rough facets in the backscatter response. The look directions at which the peak value occurs give the mean tilt of the facet.

Small-scale ripples are modeled as cosinusoidal ripples that scatter the incident electromagnetic waves in discrete directions called Floquet modes. The backscattering from the cosinusoidal ripples occurs in the directions that have Floquet modes directed towards the sensor. The total backscattering response of surface ripples is the sum of scattering from all of the surface components.

The model simulation results are similar to NSCAT and ESCAT observations over the Saharan longitudinal and transverse dune fields. Erg surface modulates the Ku- and C-band σ° measurements with the look direction. The incidence angle modulation reflects the presence of slip-sides on the surface in the form of a slight rise in backscatter at the incidence angles equal to the angle of repose of sand. At these incidence angles, the azimuth modulation indicates the number of slip-sides present that can be used to identify the transverse and longitudinal dunes.

7.1.2 Radar Backscatter Spatial Inhomogeneity of Erg Surfaces

σ° measurements over ergs are influenced by the ergs' general topography and dune geometry, and are a function of sensor view angles and footprint centroid location.

A new model is proposed that includes coupled dependence on ϕ -modulation and spatial inhomogeneity. It is shown that over ergs, θ plays a key role in varying the coupled ϕ -modulation and σ° centroid displacement variability. The σ° centroid displacement variability depends upon the general slope and sand bedform complexity. It has highest magnitudes at the erg boundaries consistent with a change of terrain from sandy surface to Hamadas. The high inhomogeneity magnitudes mark the

boundaries of major bowl-like erg basins. The new model improves the estimation of θ dependent σ° ϕ -modulation, which carries useful information about dominant facets' slopes and orientations in the antenna footprint.

7.1.3 Average Wind Behavior over Ergs from $\sigma^\circ(\theta, \phi)$ Response

The ϕ -modulation of σ° measurements at $\theta = 33^\circ$ is used to compute the dune slip-side orientations, which are almost equal to the dominant average wind directions over erg bedforms. Over the areas with simple dunes and less variable wind, the $\sigma^\circ(\theta, \phi)$ -inferred wind is spatially and temporally similar to the ECMWF wind. The model accuracy reduces over the areas with complex bedforms and high wind variability. NSCAT, ESCAT and QSCAT show similar results. The erg surface geometry response to the near-surface prevailing wind is very complicated.

7.1.4 Microwave Emission Azimuth Modulation from Erg Surfaces

Dual polarization 19 and 37 GHz T_b observations of SSM/I and TMI radiometers are used to analyze emission from erg surfaces. Combining the data from the two sensors improves the ϕ sampling of the data. The observed T_b versus ϕ is modulated by the surface geometrical characteristics and reflects the presence of dominant dune facets. ΔT_b has negligible dependence on the thermal characteristics of the surface and its ϕ -modulation varies with changes in the surface geometrical characteristics. TMI T_b observations, acquired at many times-of-day, reveal the diurnal temperature cycle of the sand surface. The time-of-day dependence is removed by using a descriptive empirical observation model with two additive second order harmonics. Although there is significant T_b diurnal dependence, it is shown that a T_b ϕ -modulation of 2-5K is observed as a result of surface geometrical characteristics. The ϕ -modulation of ΔT_b depends upon the tilts and orientation of the facets in the footprint of the sensor.

The tilted rough facet model is used to model the T_b response from the erg surface. The total T_b from dunes is the weighted sum of T_b response from its dominant facets. When modeled as surfaces composed of multiple rough facets, longitudinal and

transverse dunes exhibit significant differences in their T_b and ΔT_b ϕ -modulation: ΔT_b decreases whereas T_b increases due to a decrease in θ' . Thus, a tilted facet reveals its presence as a minimum in ΔT_b ϕ -response, where the magnitude of the ΔT_b reflects the tilt of the facet. The model simulation results are consistent with the satellite observations over areas of known dune types. Model simulation and satellite observations at 19 GHz and 37 GHz provide similar information about the dune shape and type.

7.1.5 Signatures of Amazon Vegetation

The σ° versus θ response shows distinctive behavior for different vegetation densities. The different sensors provide similar σ° incidence angle response. Different land cover types exhibit unique frequency responses of σ° and T_b . The spatial inhomogeneity model parameters provide additional information about spatial geophysical characteristics of Amazon basin.

C-band and Ku-band σ° measurements are found to be in general consistency. ESCAT σ° time series indicates a general decrease in backscatter with time. ESCAT A time series is modeled with a linear equation and its slope is used to identify areas of significant A reduction possibly caused by geophysical changes. Such areas are found mostly at the southern boundary of the Amazon forest that could be a result of deforestation.

7.1.6 Consistency of Different Spaceborne Microwave Instruments

The different sensors are generally well inter-calibrated and their data is used in combination. NSCAT and ESCAT σ° have similar directional modulation over sand and temporal behavior over vegetation. SSM/I and TMI data provide similar T_b measurements and are used in combination for better understanding of T_b ϕ -modulation. The C-band time series reveals a small calibration mismatch between ESCATs aboard ERS-1 and ERS-2 satellites.

7.2 Recommendations for Future Research

This dissertation provides new ideas, concepts, and techniques to understand microwave scattering and emission from sand bedforms and vegetation. It provides a groundwork for future research. Suggestions to extend this research include the following.

1. The T_b azimuth modulation provides information about the dominant dune facets. The analysis of T_b spatial inhomogeneity and, spatial and temporal T_b azimuth modulation can be analyzed to infer sand surface inhomogeneity and wind direction.
2. The results of σ° and T_b directional modulation can be validated using *in-situ* surface geometry data and topography maps from the spaceborne optical instruments.
3. In this research, the inferred wind is validated by comparison to ECMWF wind directions. Similar comparison can be conducted with actual wind observations from meteorological data for further validation.
4. New methods to fuse σ° and T_b data from multiple instruments to study sand and vegetation can be explored. This can help utilize the complementarity of active and passive instruments to get better insight into the surface characteristics and geophysical processes.

Suggestions to apply the ideas, methods, and results of this research to new studies include the following.

1. Snow surface geometry has some similarities to sand surface such as wind induced dunes and surface ripples. The models of this dissertation can be adopted to study snow surface geometry and aeolian processes.
2. Surface of Mars has large regions covered with sand dunes. The work presented in this research can be applied to Mars sand surfaces with appropriate parameters.

3. Previous studies have indicated the potential of some areas in Sahara for calibration of spaceborne instruments. This research provides directional modulation information of sand that can be incorporated in the calibration process.
4. This dissertation provides a methodology to infer average wind information over sand surfaces with almost no meteorological stations. This wind information can help validate results of global weather models. New ways can be developed to incorporate this information into global climate models.
5. The sensitivity of σ° and T_b to sand surface geometry provides a new insight into the scattering and emission of surfaces, which can help in the design of future precision radiometers and scatterometers.

Arid regions and tropical vegetation act as indicators of global climate change. The changes in these regions are linked to dynamics of the global climate. With a better insight into such links and relationships, remote sensing technology can help better understand global climate.

Bibliography

- [1] R. A. Bagnold, *The Physics of Blown Sand and Desert Dunes*. London: Methuen, 1941.
- [2] H. Stephen and D. G. Long, "Microwave Backscatter Modeling of Erg Surfaces in the Sahara Desert," *IEEE Transactions on Geoscience and Remote Sensing*, vol. 43, no. 2, pp. 238–247, February 2005.
- [3] H. Stephen and D. G. Long, "Azimuth Modulation of Backscatter from SeaWinds and ERS Scatterometer over the Saharo-Arabian Deserts," in *Proceedings of Intl. Geosc. and Rem. Sens. Symp., Toronto, Canada*, vol. 5, 24-28 July 2002, pp. 1780–1782.
- [4] H. Stephen and D. G. Long, "Surface Statistics of the Saharan Ergs Observed in the σ_0 Azimuth Modulation," in *Proceedings of Intl. Geosc. and Rem. Sens. Symp., Toulouse, France*, vol. 3, 21-25 July 2003, pp. 1549–1551.
- [5] H. Stephen and D. G. Long, "Analysis of Scatterometer Observations of Saharan Ergs using a Simple Rough Facet Model," in *Proceedings of Intl. Geosc. and Rem. Sens. Symp., Anchorage, Alaska*, vol. 3, 20-24 September 2004, pp. 1534–1537.
- [6] H. Stephen and D. G. Long, "Modeling Microwave Emission of Erg Surfaces in the Sahara Desert," *IEEE Transactions on Geoscience and Remote Sensing*, vol. 43, no. 12, pp. 2822–2830, December 2005.
- [7] H. Stephen, D. G. Long, and P. J. Hardin, "Vegetation Study of Amazon Basin using QSCAT in comparison with SASS, ESCAT and NSCAT," in *Proceedings of Intl. Geosc. and Rem. Sens. Symp., Honolulu, Hawaii*, vol. 1, 24-28 June 2000, pp. 429–431.
- [8] H. Stephen and D. G. Long, "Multi-Spectral Analysis of the Amazon Basin using Seawinds, ERS, NASA, Seasat Scatterometer, TRMM-PR and SSM/I," in *Proceedings of Intl. Geosc. and Rem. Sens. Symp., Toronto, Canada*, vol. 5, 24-28 July 2002, pp. 2808–2810.
- [9] R. U. Cooke and A. Warren, *Geomorphology of Deserts*. B. T. Batsford Ltd, 4 Fitzhardings Street, London W.1, UK: Anchor Press, 1973.
- [10] A. S. Goudie, I. Livingstone, and S. Stokes, *Aeolian Environments, Sediments & Landforms*. Baffins Lane, Chichester, West Sussex, PO19 1UD, England: John Wiley & Sons, Ltd, 1999.

- [11] E. D. McKee, *A Study of Global Sand Seas: Geological Survey Professional Paper 1052*. Washington: United States Government Printing Office, 1979.
- [12] K. Pye and H. Tsoar, *Aeolian Sand and Sand Dunes*. 15/17 Boardwick Street, London W1V 1FP, UK: Unwin Hyman, Ltd, 1990.
- [13] A. Sobti, R. K. Moore, and S. T. Ulaby, "Backscatter Response at 13.9 GHz for Major Terrain Types seen from Orbit," University of Kansas Space Technology Center, Remote Sensing Laboratory Technical Report 243-4, August 1975.
- [14] R. G. Kennett and F. K. Li, "Seasat Over-Land Scatterometer Data, Part I: Global overview of the Ku-Band Backscatter Coefficients," *IEEE Transactions on Geoscience and Remote Sensing*, vol. 27, no. 5, pp. 592–605, September 1989.
- [15] E. M. Bracalente, D. H. Boggs, W. L. Grantham, and J. L. Sweet, "The SASS Scattering Coefficient σ^o Algorithm," *IEEE Journal of Oceanic Engineering*, vol. OE-5, no. 2, pp. 145–154, April 1980.
- [16] R. G. Kennett and F. K. Li, "Seasat Over-Land Scatterometer Data, Part II: Selection of Extended Area Land-Target Sites for the Calibration of Spaceborne Scatterometer," *IEEE Transactions on Geoscience and Remote Sensing*, vol. 27, no. 6, pp. 779–788, November 1989.
- [17] M. Ledroit, F. Remy, and J. F. Minster, "Observations of the Antarctic Ice Sheet with the Seasat Scatterometer: Relation to Katabatic-wind Intensity and Direction," *Journal of Glaciology*, vol. 39, no. 132, pp. 385–396, 1993.
- [18] E. P. W. Attema, "The Active Microwave Instrument On-board the ERS-1 Satellite," *Proceedings of the IEEE*, vol. 79, no. 6, pp. 791–799, June 1991.
- [19] F. M. Naderi, M. H. Freilich, and D. G. Long, "Spaceborne Radar Measurement of Wind Velocity over the Ocean-An Overview of the NSCAT Scatterometer System," *Proceedings of the IEEE*, vol. 79, no. 6, pp. 850–866, 1992.
- [20] M. Spencer, C. Wu, and D. G. Long, "Tradeoffs in the Design of a Spaceborne Scanning Pencil Beam Scatterometer: Application to SeaWinds," *IEEE Transactions on Geoscience and Remote Sensing*, vol. 35, no. 1, pp. 115–126, January 1997.
- [21] T. Koizu, T. Kawanishi, H. Kuroiwa, M. Kojima, K. Oikawa, H. Kumagai, K. Okamoto, M. Okumura, H. Nakatsuka, and K. Nishikawa, "Development of Precipitation Radar Onboard the Tropical Rainfall Measuring Mission (TRMM) Satellite," *IEEE Transactions on Geoscience and Remote Sensing*, vol. 39, no. 1, pp. 102–116, Jan 2001.
- [22] C. Elachi, L. E. Roth, and G. G. Schaber, "Radar Subsurface Imaging in Hyper-arid Regions," *IEEE Transactions on Geoscience and Remote Sensing*, vol. 22, no. 4, pp. 383–388, 1984.

- [23] N. Lancaster, L. Gaddis, and R. Greeley, “New Airborne Imaging Radar Observation of Sand Dunes,” *Remote Sensing of Environment*, vol. 39, pp. 233–238, 1992.
- [24] R. G. Blom and C. Elachi, “Multifrequency and Multitemporal Radar Scatterometry of Sand Dunes and Comparison with Spaceborne and Airborne Radar Images,” *Journal of Geophysical Research*, vol. 92, pp. 7877–7889, 1987.
- [25] C. T. Swift, “Seasat Scatterometer Observations of Sea Ice,” *IEEE Transactions on Geoscience and Remote Sensing*, vol. 37, no. 2, pp. 716–723, March 1999.
- [26] A. I. Kozlov, L. P. Ligthart, and A. I. Logvin, *Mathematical and Physical Modelling of Microwave Scattering and Polarimetric Remote Sensing*. Dordrecht, The Netherlands: Kluwer Academic Publishers, 2001.
- [27] F. Ulaby, R. Moore, and A. Fung, *Microwave Remote Sensing: Active and Passive*. Norwood, Massachusetts: Artech House, Inc., 1982, vol. 2.
- [28] H. L. Chan and A. K. Fung, “A Theory of Sea Scatter at Large Incident Angles,” *Journal of Geophysical Research*, vol. 82, no. 24, pp. 3439–3444, 1977.
- [29] D. R. Lyzenga and J. F. Vesecky, “Two-Scale Polarimetric Emissivity Model: Efficiency Improvements and Comparisons with Data,” in *Progress in Electromagnetics, PIER*, no. 37, 2002, pp. 205–219.
- [30] L. Tsang, J. A. Kong, K.-H. Ding, and C. O. Ao, *Scattering of Electromagnetic Waves: Numerical Simulations*. New York, USA: A Wiley-Interscience Publication, John Wiley and Sons, Inc., 2001.
- [31] I. S. Ashcraft and D. G. Long, “Observation and Characterization of Radar Backscatter over Greenland,” *IEEE Transactions on Geoscience and Remote Sensing*, vol. 43, no. 2, pp. 225–237, February 2005.
- [32] I. J. Birrer, E. M. Bracalente, G. J. Dome, J. Sweet, and G. Berthold, “ σ^0 Signature of the Amazon Rain Forest obtained from the Seasat Scatterometer,” *IEEE Transactions on Geoscience and Remote Sensing*, vol. GE-20, no. 1, pp. 11–17, January 1982.
- [33] P. Lecomte and E. P. W. Attema, “Calibration and Validation of the ERS-1 Wind Scatterometer,” in *ESA SP-359*, November 1992, pp. 19–29.
- [34] P. Lecomte and W. Wagner, “ERS Wind Scatterometer Commissioning and In-flight Calibration,” in *ESA WWP-147*, July 1997, pp. 261–270.
- [35] D. G. Long and G. B. Skouson, “Calibration of Spaceborne Scatterometers using Tropical Rain Forests,” *IEEE Transactions on Geoscience and Remote Sensing*, vol. 34, no. 2, pp. 413–424, March 1996.

- [36] J. Zec, D. G. Long, and W. L. Jones, "NSCAT Normalized Radar Backscattering Coefficient Biases using Homogeneous Land Targets," *Journal of Geophysical Research*, vol. 104, no. C5, pp. 11 557–11 568, May 1999.
- [37] R. D. Magagi and Y. H. Kerr, "Retrieval of Soil Moisture and Vegetation Characteristics by use of ERS-1 Scatterometer over Arid and Semi-Arid Areas," *Journal of Hydrology*, vol. 188-189, pp. 361–384, 1997.
- [38] J. T. Pulliainen, T. Manninen, and M. Hallikainen, "Application of ERS-1 Wind Scatterometer Data to Soil Frost and Soil Moisture Monitoring in Boreal Forest Zone," *IEEE Transactions on Geoscience and Remote Sensing*, vol. 36, no. 3, pp. 849–863, May 1998.
- [39] W. Wagner, G. Limoine, and H. Rott, "A Method for Estimating Soil Moisture from ERS Scatterometer and Soil Data," vol. 70, 1999, pp. 191–207.
- [40] D. G. Long and P. J. Hardin, "Vegetation Studies of the Amazon Basin using Enhanced Resolution Seasat Scatterometer Data," *IEEE Transactions on Geoscience and Remote Sensing*, vol. 32, no. 2, pp. 449–460, March 1994.
- [41] P. J. Hardin and D. G. Long, "Discrimination Between Tropical Vegetation Formations using Reconstructed Seasat-A Scatterometer Data," *Photogrammetric Engineering and Remote Sensing*, vol. 60, no. 12, pp. 1453–1462, December 1994.
- [42] E. Mougin, A. Lopes, P. L. Frison, and C. Proisy, "Preliminary Analysis of ERS-1 Wind Scatterometer Data over Land Surfaces," *International Journal of Remote Sensing*, vol. 16, no. 2, pp. 391–398, 1995.
- [43] P. L. Frison and E. Mougin, "Use of ERS-1 Wind Scatterometer Data over Land Surfaces," *IEEE Transactions on Geoscience and Remote Sensing*, vol. 34, no. 2, pp. 550–560, March 1996.
- [44] P. L. Frison and E. Mougin, "Monitoring Global Vegetation Dynamics with ERS-1 Wind Scatterometer Data," *International Journal of Remote Sensing*, vol. 17, no. 16, pp. 3201–3218, 1996.
- [45] P. L. Frison, E. Mougin, and P. Hiernaux, "Observations and Interpretation of Seasonal ERS-1 Wind Scatterometer Data over Northern Sahel (Mali)," *Remote Sensing of Environment*, vol. 63, pp. 233–242, 1998.
- [46] I. H. Woodhouse and D. H. Hoekman, "Determining Land-Surface Parameters from the ERS Wind Scatterometer," *IEEE Transactions on Geoscience and Remote Sensing*, vol. 38, no. 1, pp. 126–140, January 2000.
- [47] T. Manninen, P. Stenberg, M. Rautiainen, P. Voipio, and H. Smolander, "Leaf Area Index Estimation of Boreal Forest using ENVISAT ASAR," *IEEE Transactions on Geoscience and Remote Sensing*, vol. 43, no. 11, pp. 2627–2635, 2005.

- [48] J. E. H. Dyal, “TRMM Sigma-0 Vegetation Signatures and Other Studies,” Master’s thesis, Brigham Young University, Provo, Utah, August 1999.
- [49] D. G. Long, “Comparison of TRMM and NSCAT Observations of Surface Backscatter over the Amazon Rain Forest,” in *Proceedings of Intl. Geosc. and Rem. Sens. Symp.*, vol. 4, 6-10 July 1998, pp. 1879–1881.
- [50] M. Satake and H. Hanado, “Diurnal Change of Amazon Rain Forest σ° Observed by Ku-Band Spaceborne Radar,” *IEEE Transactions on Geoscience and Remote Sensing*, vol. 42, no. 6, pp. 1127–1134, June 2004.
- [51] G. Watt, “Vegetation Classification using Seasonal Variations of Scatterometer Data at C-band and Ku-band,” Master’s thesis, Brigham Young University, Provo, Utah, August 1999.
- [52] P. J. Hardin, D. G. Long, and Q. P. Remund, “Discrimination of Africa’s Vegetation using Reconstructed ERS-1 Imagery,” in *Proceedings of Intl. Geosc. and Rem. Sens. Symp.*, vol. 2, 27-31 May 1996, pp. 827–829.
- [53] J. P. Hollinger, R. Lo, G. A. Poe, R. Savage, and J. L. Peirce, *Special Sensor Microwave/Imager User’s Guide*, Naval Research Laboratory, Washington DC, 1987.
- [54] J. P. Hollinger, J. L. Peirce, and G. A. Poe, “SSM/I Instrument Evaluation,” *IEEE Transactions on Geoscience and Remote Sensing*, vol. 28, no. 5, pp. 781–790, September 1990.
- [55] D. G. Long, Q. P. Remund, and D. L. Daum, “A Cloud-Removal Algorithm for SSM/I Data,” *IEEE Transactions on Geoscience and Remote Sensing*, vol. 37, no. 1, pp. 54–62, January 1999.
- [56] C. Kummerow, W. Barnes, T. Kozu, J. Shiue, and J. Simpson, “The Tropical Rainfall Measuring Mission (TRMM) Sensor Package,” *Journal of Atmospheric and Ocean Technology*, vol. 15, pp. 808–816, June 1998.
- [57] K. F. Kunzi, S. Patil, and H. Rott, “Snow-Cover Parameters Retrieved from Nimbus-7 Scanning Multichannel Microwave Radiometer (SMMR) Data,” *IEEE Transactions on Geoscience and Remote Sensing*, vol. GE-20, pp. 452–467, 1982.
- [58] R. R. Ferrero, N. C. Grody, and J. A. Kogut, “Classification of Geophysical Parameters using Passive Microwave Satellite Measurements,” *IEEE Transactions on Geoscience and Remote Sensing*, vol. GE-24, pp. 1008–1013, November 1986.
- [59] M. J. McFarland, R. L. Miller, and C. M. Neale, “Land-Surface Temperature Derived from SSM/I Passive Microwave Brightness Temperatures,” *IEEE Transactions on Geoscience and Remote Sensing*, no. 28, pp. 839–845, 1990.

- [60] C. M. U. Neale, M. J. McFarland, and K. Chang, "Land-Surface-Type Classification using Microwave Brightness Temperatures from the Special Sensor Microwave/Imager," *IEEE Transactions on Signal Processing*, vol. 28, no. 5, pp. 829–838, September 1990.
- [61] J. V. Fiore and N. C. Grody, "Classification of Snow Cover and Precipitation using SSM/I Measurements: Case Studies," *International Journal of Remote Sensing*, no. 13, pp. 3349–3361, 1992.
- [62] T. Yu, X. Gu, G. Tian, M. Legrand, F. Baret, J.-F. Hanocq, R. Bosseno, and Y. Zhang, "Modeling Directional Brightness Temperature over a Maize Canopy in Row Structure," *IEEE Transactions on Geoscience and Remote Sensing*, vol. 42, no. 10, pp. 2290–2304, October 2004.
- [63] C. Prigent, W. B. Rossow, E. Matthews, and B. Marticorena, "Microwave Radiometer Signatures of Different Surface Types in Deserts," *Journal of Geophysical Research*, vol. 104, no. D10, pp. 12 147–12 158, 1999.
- [64] G. Macelloni, S. Paloscia, P. Pampaloni, and E. Santi, "Global Scale Monitoring of Soil and Vegetation using SSM/I and ERS Wind Scatterometer," *International Journal of Remote Sensing*, vol. 24, no. 12, pp. 2409–2425, 2003.
- [65] D. G. Long and M. R. Drinkwater, "Azimuth Variation in Microwave Scatterometer and Radiometer Data over Antarctic," *IEEE Transactions on Geoscience and Remote Sensing*, vol. 38, no. 4, pp. 1857–1870, July 2000.
- [66] L. Tsang, J. A. Kong, and K.-H. Ding, *Scattering of Electromagnetic Waves: Theories and Applications*. New York, USA: A Willey-Interscience Publication, John Wiley and Sons, Inc., 2000.
- [67] F. Ulaby, R. Moore, and A. Fung, *Microwave Remote Sensing: Active and Passive*. Norwood, Massachusetts: Artech House, Inc., 1982, vol. 3.
- [68] T. J. Schmugge, "Remote sensing of soil moisture: Recent advances," *IEEE Transactions on Geoscience and Remote Sensing*, vol. GE-21, no. 3, pp. 336–344, July 1983.
- [69] P. J. Hardin, D. G. Long, Q. P. Remund, and D. R. Daum, "A Comparison of Reconstructed Ku-band Scatterometry, C-band Scatterometry and SSM/I Imagery for Tropical Vegetation Classification," in *Proceedings of Intl. Geosc. and Rem. Sens. Symp.*, vol. 2, 27-31 May 1996, pp. 848–850.
- [70] G. Macelloni, S. Paloscia, P. Pampaloni, and R. Ruisi, "Airborne Multifrequency L- Ka- Band Radiometric Measurements over Forests," *IEEE Transactions on Geoscience and Remote Sensing*, vol. 39, no. 11, pp. 2507–2513, November 2001.
- [71] H. Hersbach and S. Abdalla, "The Global Validation of ERS Wind and Wave Product at ECMWF," in *Proceedings of 2004 Envisat and ERS Symposium*, vol. ESA SP-572, April 2005.

- [72] T. T. Warner, *Desert Meteorology*. The Edinburgh Building, Cambridge, CR2 2RU, UK: Cambridge University Press, 2004.
- [73] M. Mainguet, *Space Observation of Saharan Aeolian Dynamics*. Dordrecht, The Netherlands: Martinus Nijhoff, 1984.
- [74] C. A. Balanis, *Advanced Engineering Electromagnetics*. USA: John Wiley & Sons, Inc, 1998.
- [75] J. A. Kong, *Electromagnetic Wave Theory*. Cambridge, Massachusetts, USA: EMW Publishing, 1999.

Appendix A

Derivation of View Geometry Relationships

This appendix summarizes the derivation of geometric relations between the local incidence, azimuth and grazing angles of a tilted rough facet. The view directions of a cosinusoidal wave on the rough facet that result in Bragg backscattering are also derived.

Consider a rough facet that has a unit surface normal vector $\hat{\mathbf{n}}$ and cosinusoidal surface wave with period λ_s represented by $\mathbf{K} = K\hat{\mathbf{K}}$ where $K = 2\pi/\lambda_s$ (see Fig. 3.4). Let the electromagnetic wave with a wave vector $\mathbf{k} = k\hat{\mathbf{k}}$ be incident on the surface. Here, $k = 2\pi/\lambda$ with λ being the wavelength of the incident wave. Figure 3.4 also depicts spherical angles of these vectors relative to the principal coordinate system $(\hat{\mathbf{x}}, \hat{\mathbf{y}}, \hat{\mathbf{z}})$.

A.1 Local Incidence and Azimuth Angles

The local normal vector $\hat{\mathbf{n}}$ and incidence wave vector $\hat{\mathbf{k}}$ are

$$\hat{\mathbf{n}} = \sin \theta_s \cos \phi_s \hat{\mathbf{x}} + \sin \theta_s \sin \phi_s \hat{\mathbf{y}} + \cos \theta_s \hat{\mathbf{z}} \quad (\text{A.1})$$

$$\text{and } \hat{\mathbf{k}} = \sin \theta \cos \phi \hat{\mathbf{x}} + \sin \theta \sin \phi \hat{\mathbf{y}} + \cos \theta \hat{\mathbf{z}}. \quad (\text{A.2})$$

The slopes of the surface in x and y directions are given by

$$Z_x = -\frac{\sin \theta_s}{\cos \theta_s} \cos \phi_s \quad (\text{A.3})$$

$$\text{and } Z_y = -\frac{\sin \theta_s}{\cos \theta_s} \sin \phi_s, \quad (\text{A.4})$$

where the inverse relationship is given by

$$\theta_s = \tan^{-1}\left(\sqrt{Z_x^2 + Z_y^2}\right) \quad (\text{A.5})$$

$$\text{and } \phi_s = \tan^{-1}\left(\frac{Z_y}{Z_x}\right). \quad (\text{A.6})$$

The local coordinate system $(\hat{\mathbf{x}}', \hat{\mathbf{y}}', \hat{\mathbf{z}}')$ is defined as

$$\hat{\mathbf{z}}' = \hat{\mathbf{k}}, \quad (\text{A.7})$$

$$\hat{\mathbf{x}}' = \cos\theta \cos\phi \hat{\mathbf{x}} + \cos\theta \sin\phi \hat{\mathbf{y}} - \sin\theta \hat{\mathbf{z}} \quad (\text{A.8})$$

$$\text{and } \hat{\mathbf{y}}' = \hat{\mathbf{z}}' \times \hat{\mathbf{x}}' = -\sin\phi \hat{\mathbf{x}} + \cos\phi \hat{\mathbf{y}}. \quad (\text{A.9})$$

In the $(\hat{\mathbf{x}}', \hat{\mathbf{y}}', \hat{\mathbf{z}}')$ coordinates $\hat{\mathbf{n}}$ is

$$\hat{\mathbf{n}}' = (\hat{\mathbf{n}} \cdot \hat{\mathbf{x}}')\hat{\mathbf{x}}' + (\hat{\mathbf{n}} \cdot \hat{\mathbf{y}}')\hat{\mathbf{y}}' + (\hat{\mathbf{n}} \cdot \hat{\mathbf{z}}')\hat{\mathbf{z}}'. \quad (\text{A.10})$$

The surface slopes expressed in the local coordinate system are

$$Z'_x = -\frac{\hat{\mathbf{n}} \cdot \hat{\mathbf{x}}'}{\hat{\mathbf{n}} \cdot \hat{\mathbf{z}}'} \quad (\text{A.11})$$

$$\text{and } Z'_y = -\frac{\hat{\mathbf{n}} \cdot \hat{\mathbf{y}}'}{\hat{\mathbf{n}} \cdot \hat{\mathbf{z}}'}. \quad (\text{A.12})$$

Hence, the spherical angles of $\hat{\mathbf{n}}$ in the local coordinates are given as

$$\theta' = \tan^{-1}\left(\frac{\sqrt{(\hat{\mathbf{n}} \cdot \hat{\mathbf{x}}')^2 + (\hat{\mathbf{n}} \cdot \hat{\mathbf{y}}')^2}}{\hat{\mathbf{n}} \cdot \hat{\mathbf{z}}'}\right) \quad (\text{A.13})$$

$$\text{and } \phi' = \tan^{-1}\left(\frac{\hat{\mathbf{n}} \cdot \hat{\mathbf{y}}'}{\hat{\mathbf{n}} \cdot \hat{\mathbf{x}}'}\right). \quad (\text{A.14})$$

A.2 Grazing Angle

The local grazing angle θ_g is elevation angle of $\hat{\mathbf{k}}_g$ in the global coordinates, where $\hat{\mathbf{k}}_g$ is a unit vector in the direction of the projection of \mathbf{k} on the facet, is given by

$$\hat{\mathbf{k}}_g = \frac{\hat{\mathbf{n}} \times (\hat{\mathbf{k}} \times \hat{\mathbf{z}})}{|\hat{\mathbf{n}} \times (\hat{\mathbf{k}} \times \hat{\mathbf{z}})|} = \frac{(\hat{\mathbf{z}} \cdot \hat{\mathbf{n}})\hat{\mathbf{k}} - (\hat{\mathbf{n}} \cdot \hat{\mathbf{k}})\hat{\mathbf{z}}}{|\hat{\mathbf{n}} \times (\hat{\mathbf{k}} \times \hat{\mathbf{z}})|} \quad \text{and} \quad (\text{A.15})$$

$$\tan\theta_g = \frac{|\hat{\mathbf{k}}_g \times \hat{\mathbf{z}}|}{\hat{\mathbf{k}}_g \cdot \hat{\mathbf{z}}} = \frac{(\hat{\mathbf{n}} \cdot \hat{\mathbf{z}})\sqrt{1 - (\hat{\mathbf{k}} \cdot \hat{\mathbf{z}})^2}}{(\hat{\mathbf{n}} \cdot \hat{\mathbf{z}})(\hat{\mathbf{k}} \cdot \hat{\mathbf{z}}) - (\hat{\mathbf{n}} \cdot \hat{\mathbf{k}})} = -\frac{1}{\tan\theta_s \cos(\phi_s - \phi)}. \quad (\text{A.16})$$

A.3 Bragg Look Directions

A periodic surface causes the incident wave to be scattered in discrete directions called Floquet modes [75]. For Bragg backscattering to occur there must be a Floquet mode in the direction of the sensor. This condition can be written in vector form as

$$(\widehat{\mathbf{K}} \times \widehat{\mathbf{n}}) \cdot \widehat{\mathbf{k}} = 0 \quad (\text{i.e., vectors must be coplanar}) \quad (\text{A.17})$$

$$\text{and } \widehat{\mathbf{K}} \cdot \widehat{\mathbf{k}} = -\frac{mK}{2k}. \quad (\text{A.18})$$

For a rippled rough surface facet geometry specified by $\widehat{\mathbf{n}}$ and $\widehat{\mathbf{K}}$ all look directions $\widehat{\mathbf{k}}_m$ that result in Bragg backscattering can be found. Here m represents the Floquet mode that is backscattered. Multiplying Eqs. (A.17) and (A.18) by $\widehat{\mathbf{K}}$ and $(\widehat{\mathbf{K}} \times \widehat{\mathbf{n}})$, respectively, and then subtracting the two gives

$$\widehat{\mathbf{K}}\{(\widehat{\mathbf{K}} \times \widehat{\mathbf{n}}) \cdot \widehat{\mathbf{k}}_m\} - (\widehat{\mathbf{K}} \times \widehat{\mathbf{n}})(\widehat{\mathbf{K}} \cdot \widehat{\mathbf{k}}_m) = \frac{mK}{2k}(\widehat{\mathbf{K}} \times \widehat{\mathbf{n}}). \quad (\text{A.19})$$

Since

$$\widehat{\mathbf{K}} \cdot \widehat{\mathbf{n}} = 0 \quad (\text{A.20})$$

$$\text{and } -\widehat{\mathbf{k}}_m \times \widehat{\mathbf{n}} = \frac{mK}{2k}(\widehat{\mathbf{K}} \times \widehat{\mathbf{n}}), \quad (\text{A.21})$$

it becomes

$$(\widehat{\mathbf{k}}_m + \frac{mK}{2k}\widehat{\mathbf{K}}) \times \widehat{\mathbf{n}} = \mathbf{0}. \quad (\text{A.22})$$

The null cross product indicates that the two vectors are colinear and hence one can be written as a scalar multiple of the other as $\widehat{\mathbf{k}}_m + \frac{mK}{2k}\widehat{\mathbf{K}} = t\widehat{\mathbf{n}}$ and the Bragg backscattering direction as $\widehat{\mathbf{k}}_m = t\widehat{\mathbf{n}} - \frac{mK}{2k}\widehat{\mathbf{K}}$, where t is some scalar. t can be found from using the fact that $\widehat{\mathbf{k}}_m \cdot \widehat{\mathbf{k}}_m = 1$; hence,

$$\{t\widehat{\mathbf{n}} - \frac{mK}{2k}\widehat{\mathbf{K}}\} \cdot \{t\widehat{\mathbf{n}} - \frac{mK}{2k}\widehat{\mathbf{K}}\} = t^2 + \left(\frac{mK}{2k}\right)^2 = 1. \quad (\text{A.23})$$

Thus, the Bragg backscattering directions can be written as

$$\widehat{\mathbf{k}}_m = \pm \sqrt{1 - \left(\frac{mK}{2k}\right)^2} \widehat{\mathbf{n}} - \frac{mK}{2k}\widehat{\mathbf{K}}. \quad (\text{A.24})$$

A.4 Maxima of Second Order Harmonic

The second order harmonic equation is given by

$$\sigma^\circ(\theta, \phi) = A + M_1 \cos(\phi - \phi_1) + M_2 \cos(2\phi - \phi_2). \quad (\text{A.25})$$

Differentiating with respect to ϕ and setting it equal to zero gives

$$\frac{\partial \sigma^\circ(\theta, \phi)}{\partial \phi} = -M_1(\theta) \sin(\phi - \phi_1(\theta)) - 2M_2(\theta) \sin(2\phi - \phi_2(\theta)) = 0. \quad (\text{A.26})$$

The θ dependence of the parameters is dropped for convenience. The relationship

$$M_1 \sin(\phi - \phi_1) + 2M_2 \sin(2\phi - \phi_2) = 0 \quad (\text{A.27})$$

can be written as

$$M_1 \cos \phi_1 \sin \phi - M_1 \sin \phi_1 \cos \phi + 2M_2 \cos \phi_2 \sin 2\phi - 2M_2 \sin \phi_2 \cos 2\phi = 0. \quad (\text{A.28})$$

Let $x = \sin \phi$ and $y = \cos \phi = \sqrt{1 - x^2}$ then

$$\begin{aligned} \sin 2\phi &= 2xy = 2x\sqrt{1 - x^2} \\ \text{and } \cos 2\phi &= y^2 - x^2 = 1 - 2x^2. \end{aligned} \quad (\text{A.29})$$

Let $a_1 = M_1 \cos \phi_1$, $a_2 = M_2 \cos \phi_2$, $b_1 = M_1 \sin \phi_1$ and $b_2 = M_2 \sin \phi_2$ then

$$a_1x - b_1\sqrt{1 - x^2} + 4a_2x\sqrt{1 - x^2} - 2b_2(1 - 2x^2) = 0 \quad (\text{A.30})$$

or

$$(4a_2x - b_1)\sqrt{1 - x^2} = 2b_2(1 - x^2) - a_1x. \quad (\text{A.31})$$

Squaring both sides

$$(16a_2^2x^2 - 8a_2b_1x + b_1^2)\sqrt{1 - x^2} = 4b_2^4 + a_1^2x^2 + 16b_2^2x^4 - 4a_1b_2x - 16b_2^2x^2 + 8a_1b_2x^2 \quad (\text{A.32})$$

or

$$\begin{aligned} 16(a_2^2 + b_2^2)x^4 + 8(b_2a_1 - b_1a_2)x^3 \{a_1^2 + b_1^2 - 16(a_2^2 + b_2^2)\}x^2 \\ + 4(b_2a_1 - b_1a_2 - b_1a_2)x + (4b_2^2 - b_1^2) = 0 \end{aligned} \quad (\text{A.33})$$

or

$$\begin{aligned}
& 16M_2^2x^4 + 8M_1M_2 \sin(\phi_2 - \phi_1)x^3 + (M_1^2 - 16M_2^2)x^2 \\
& + 4M_1M_2(\sin(\phi_2 - \phi_1) - \sin \phi_1 \cos \phi_2)x \\
& + (2M_2 \sin \phi_2)^2 - (M_1 \sin \phi_1)^2 = 0, \quad (\text{A.34})
\end{aligned}$$

which is a quartic equation and can be used to find the extrema of the second order harmonic. The solution is two quadrant $\sin \phi$ which is used to find $\cos \phi = \pm \sqrt{1 - \sin^2 \phi}$ resulting in eight choices. The derivative equation is used to find the correct four solutions from the eight choices. Once the extrema are found, the second derivative can be used to differentiate between maxima and minima. If φ is a solution then

$$\frac{\partial^2 \sigma^\circ}{\partial \phi^2} \Big|_\varphi > 0 \text{ means } \varphi \text{ is a minimum,} \quad (\text{A.35})$$

$$\frac{\partial^2 \sigma^\circ}{\partial \phi^2} \Big|_\varphi < 0 \text{ means } \varphi \text{ is a maximum, and} \quad (\text{A.36})$$

$$\frac{\partial^2 \sigma^\circ}{\partial \phi^2} \Big|_\varphi = 0 \text{ means } \varphi \text{ is a saddle point.} \quad (\text{A.37})$$